Optimizing Blunt Nose Cone Designs and Canard Placements for Military Missiles to Mitigate Shockwave Interference

a project presented to
The Faculty of the Department of Aerospace Engineering
San José State University

in partial fulfillment of the requirements for the degree
Master of Science in Aerospace Engineering

by

Baraa W. Al-Sammarraie

May 2025

approved by

Dr. Ezunkpe
Faculty Advisor

© 2025
Baraa W. Al-Sammarraie
ALL RIGHTS RESERVED

ABSTRACT

Optimizing Blunt Nose Cone Designs and Canard Placements for Military Missiles to Mitigate Shockwave Interference

Baraa W. Al-Sammarraie

The purpose of this project is to take a further step in military equipment development by addressing and attempting to solve an existing problem in military and defense missile design. This project discusses why current military missile designs do not feature blunt nose cones for missiles that fly in the supersonic and hypersonic regimes. The project analyzes, optimizes, and designs various blunt nose cone configurations that focus on internal capacity while considering the flow characteristics over the canards. The results will be verified through CFD analysis and 3D printing of the selected efficient designs, followed by testing the nose cone and validating the CFD results through Level 3 Rocket certification testing.

ACKNOWLEDGEMENTS

With heartfelt gratitude, I extend my deepest thanks to Dr. Yawo Ezunkpe, whose unwavering guidance, patience, and wisdom have shaped every step of this journey. His mentorship has been a constant light through the most challenging moments.

To my beloved mother, Suad Khalid, your endless prayers, strength, and belief in me carried me through every obstacle. You are the quiet force behind every success.

To my sisters, Raghad and Nawar. thank you for your constant emotional support, for being my refuge, and for reminding me of who I am when I forget.

And finally, to the man who gave me the world without asking for anything in return, Watheq Al-Sammarraie. Your love is boundless, your generosity immeasurable. The world could never offer what you have given me.

Table Of Contents

List of Figures

List of Tables

Symbols

Symbol	Definition	Units (SI)
M	Mach Number	unitless
P	Pressure	Pa
T	Temperature	K
V	Velocity	m/s
u	The normal component	Unitless
w	The tangential component	Unitless
L	Length of Nose Cone	m
R	Radius on Nose Cone Base	m
x	X coordinate in space	unitless
y	Y coordinate in space	unitless
n	Power of Power-Law/Von Karman Nose Cone	unitless
Rs	Radius of Curvature	m
Greek Symbols		
β	Wave Angle	Degrees
θ	Deflection Angle // Semi-Vertex Angle	Degrees
ρ	Density	kg/m3
γ	Heat Capacity Ratio	Unitless
ξ	Bluntness Ratio	Unitless
Subscripts		
Acronyms		
NASA	National Aeronautics and Space Administration	-------
AAM	Air-to-Air Missile	-------
ASM	Air-to-Surface Missile	-------
SAM	Surface-to-Air Missile	-------
SSM	Surface-to-Surface Missile	-------
ICBMs	Intercontinental Ballistic Missiles	-------
L3	Level 3	-------
CAD	Computer-Aided Design	-------
IR	Infrared	-------
CP	Center of Pressure	m
CG	Center of Gravity	m
PETG	Polyethylene Terephthalate Glycol-modified	
FAR	Friends of Amateur Rocketry	-------
TPS	Thermal Protection System	-------

1. Introduction

1.1 Motivation

In the domain of military and defense technology, missile systems and military rockets are essential elements for national security. The development and optimization of more advanced missile technologies, particularly in the supersonic and hypersonic regimes, is a first priority for military forces around the world. The Department of Defense's 2022 Strategic Reviews emphasizes the importance of missile defense in defending the homeland, deterring aggression, and staying ahead of technological advancements from adversaries [1]. Moreover, the Atlantic Council assures that improving the U.S. homeland missile defense system not only enhances deterrence but also strengthens the overall credibility of retaliatory threats, especially against smaller-scale attacks from adversaries[2]. Given these escalating risks, advancements in missile design that prioritize better aerodynamic performance and shockwave mitigation, like the project on blunt nose cone optimization, can significantly contribute to U.S. defense capabilities. This project aligns with the need for more resilient defense systems capable of countering a broad range of threats.

1.2 Literature Review

Missiles are guided devices with precise aim that are designed to deliver destructive payloads to specific targets, varying from long or short distances. Missile technology, especially in the supersonic and hypersonic regimes, plays a crucial role in modern military strategy due to its high speeds, maneuverability, and ability to engage targets with minimal warning. Supersonic missiles, traveling at speeds between Mach 1 and Mach 5, and hypersonic missiles, exceeding Mach 5, provide rapid-response capabilities, allowing military forces to strike high-value targets before opponents can react or counter.

The design of a supersonic or a hypersonic guided missile is considered complex, as it requires a comprehensive understanding of several interconnected technical disciplines. These include aerodynamics, where high-speed flow interactions must be tuned to reduce drag and manage shockwaves, dynamic stability to ensure precision control and rapidity during maneuvers, and structural design to withstand the intense aerodynamic and thermal stresses caused by traveling at such high speeds. This complex interplay between these disciplines is critical to achieving the performance, accuracy, and durability required in such high-speed regimes as confirmed in NASA's comprehensive review on hypersonic vehicle structures and materials [3]. The precision of canard control systems, structural integrity under extreme conditions, and thermal management are all critical factors that further compound the design complexity at these speeds.

1.2.1 Missile Classification & Controls type

1.2.1.1 Missile Classification of Design

Missiles in the aerospace industry are classified into four classes [4]: air-to-air missiles (AAM), air-to-surface missiles (ASM), surface-to-air missiles (SAM), and surface-to-surface missiles (SSM).

Air-to-surface missiles (AAMs) are designed to be launched from aircraft to target or destroy other airborne threats, such as other missiles or enemy unmanned planes, this type of missile is comparatively smaller than other missiles due to the payload constraints of small fighter aircraft [5], the relatively short-range equipment needed to execute mission and shot flight time [6].

In contrast, air-to-surface missiles (ASMs) are primarily developed as offensive or tactical devices to take out stationary targets, including gun emplacements of the enemy, tanks, airfields, and ships. These missiles have lower maneuverability requirements compared to air-to-air missiles (AAMs) due to the relatively slow-moving or stationary nature of targets. ASMs are made to launch precise strikes, and they frequently have characteristics like distinct guidance systems and warhead designs that are optimized for particular kinds of ground-based threats. These features let ASMs perform as effectively as possible in various operating settings[4].

The surface-to-surface missile (SSM) serves dual purposes in warfare. It can function as a long-range retaliatory weapon, delivering strategic strikes against distant targets. Additionally, it can be employed to support ground troops, fulfilling a role similar to that of an artillery battery by providing close support and firepower on the battlefield [4]. This versatility allows SSMs to address both strategic and tactical needs in military operations.

Finally, surface-to-air missiles (SAMs) are mostly designed for the purpose of defense against attacking enemy aircraft, drones, or intercontinental ballistic missiles (ICBMs). Their aerodynamic design is fully influenced by their range, which can vary from a few miles to several hundred miles, and speed, which can vary from subsonic to hypersonic. For short and medium ranges, a liquid-propellant or a single-stage solid rocket motor is commonly used[4]. This classification is the primary focus of this project due to the frequent and urgent need for such missiles in contemporary defense systems, as well as the feasibility of testing them in an academic setting. The project will proceed under the assumption that the missile is a SAM/AAM, with the rocket designed and built for L3 certification expected to resemble similar characteristics to a SAM/AAM.

Figure 1.1 - Demonstration of missile classification [7].

1.2.1.2 Design Controls Type

Various external aerodynamic configurations are used in missile design for different purposes and classifications, with canard control being especially prevalent in surface-to-air missile classification. This system uses small forward canards and larger rear wings or tail surfaces. The minimal downwash from the canards ensures stable flight without directly affecting longitudinal stability, allowing flexibility in the placement of wings or tail sections to achieve the stability margins desired [8]. Lift is generated mainly through the missile's angle of attack (α), as the canard's lift is countered by the wing's downwash as displayed in Figure 1.2. The greatest advantage of the canard configuration is its compactness, particularly beneficial for missile packaging simplicity and internal capacity optimization [8].

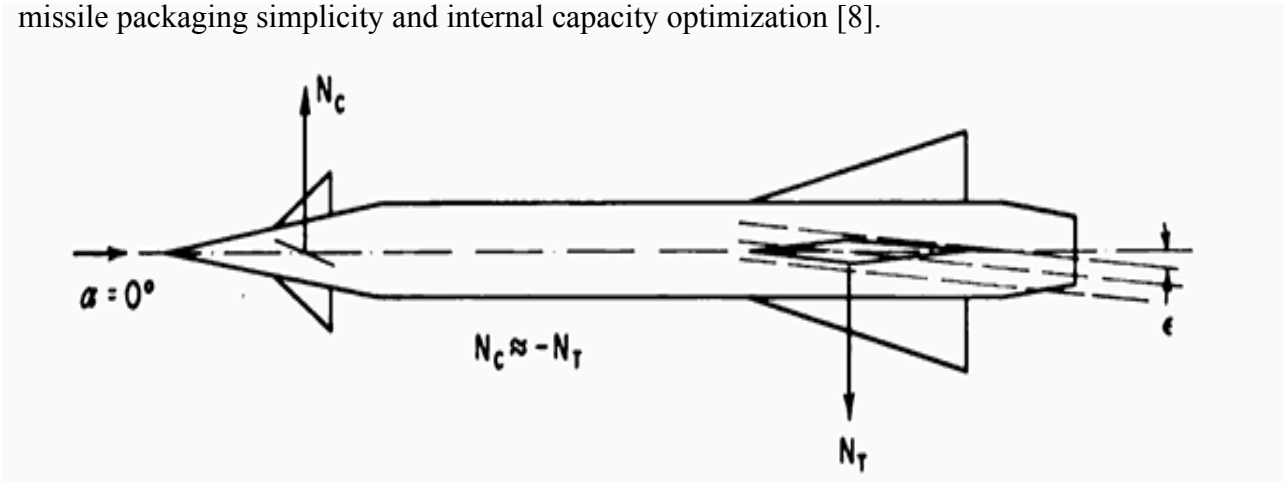

Figure 1.2 - Contrasting the loads on the canard and tail [4].

The relatively small size of canards reduces space constraints at the nose, making the design efficient for supersonic and hypersonic regimes when a round nose cone shape is utilized; at these high speeds, when the missile nose is round, the flow remains attached, allowing the

canards to respond effectively to stability inputs [9,10]. This provides missile designers the flexibility in canard placement, as airflow remains undisturbed. However, the challenge arises when a blunt nose cone design is used. Blunt noses generate bow shockwaves that interfere with the airflow that canards are exposed to [9,10]. These shockwaves can significantly disrupt the missile's stability and control, reducing the effectiveness of the canards [9]. The project aims to analyze this effect in detail, focusing on optimizing canard placement to maintain stability despite the shockwave interference caused by a blunt nose cone. Addressing this issue is critical to ensuring that canard-controlled missiles remain effective at the desired speeds of supersonic and hypersonic.

1.2.2 Supersonic/Hypersonic Flows over Nose Cones

In supersonic (Mach 1-5) and hypersonic (Mach 5 and above) regimes, shockwave formation dominates the flow characteristics around an object, directly impacting the aerodynamic performance and stability of the missiles. At supersonic speeds, shockwaves form when air is compressed beyond the speed of sound (Mach =1), creating abrupt changes in pressure, temperature, and density in the flow field. These shockwaves can either be oblique (tilted with an angle) or normal (perpendicular to the flow), depending on the shape of the object and the speed. In hypersonic flow, these effects intensify drastically, leading to the formation of strong detached bow shocks in front of the body. These bow shocks create a high-pressure, high-temperature stagnation region at the nose, resulting in significant heat transfer to the vehicle surface [11]. The high temperatures, combined with intense aerodynamic drag, present big challenges in designing vehicles for high-speed travel[11,12], the NASA "Materials and Structures for Hypersonic Vehicles*"* research paper outlined that the challenges caused by high temperature and extreme drag mainly are in material durability, structural integrity due to vibrations, thermal expansion, and material fatigue[3].

1.2.2.1 Supersonic/Hypersonic Flows over Different Nose Cones Designs

Nose cones are described to be the most forward section of the missile or a rocket, a blunt nose cone on the other hand, is rounded or flat-tipped; this nose cone design is effective in handling massive thermal loads and shockwaves in designated high-speed conditions, but it is typically not the most efficient design when it comes to minimizing aerodynamic drag at supersonic or hypersonic speeds, where a more sharp-tipped or streamlined nose cone is preferred [13]. The common blunted nose cone designs include hemispherical, blunted ogive, spherically blunted cones, power series, blunted tangent-ogives, some types of von Kármán, and parabolic blunt nose cones. These variations of blunt nose cone designs are often chosen based on specific aerodynamic requirements and carry distinctive geometric features.

In the "Analysis of Nose Cone of Missile" research paper by P. Kiran Kumar on the flow around a tangent-ogive nose cone, the results showed a distinctive pattern of aerodynamic behaviors. The blunted tangent-ogive design, characterized by its round, smooth curves that transition into a semi-sharp tip, generates a shockwave that is particularly strong at the nose cone's tip[14]. This design results in a defined oblique shock wave at the tip, which remains

comparatively stronger than other nose cone shapes. The pressure and velocity distributions around the tangent-ogive nose cone are uniform and well-defined at the tip, contributing to an effective drag reduction[15]. As the Mach number increases, the angle of the oblique shock wave decreases, causing a weak shockwave. Despite this, the tangent-ogive nose cone maintains relatively high pressure and aerodynamic efficiency, making it suitable for supersonic applications where minimal drag and efficient airflow management are critical [14].

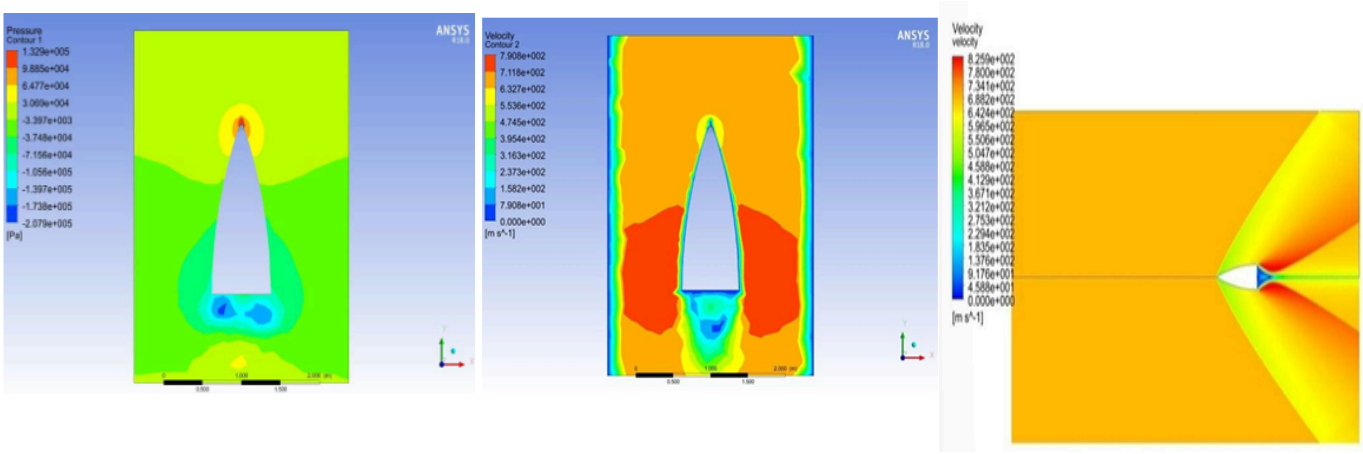

Figure 1.3 - Shockwave, pressure, and velocity contour of the tangent-ogive at mach 2. [14].

For the spherically blunted nose cone, the blunt tip of the nose cone generates a shock wave that is less intense and more undefined than that of sharper nose-cone designs such as the tangent-ogive. This spherically blunted configuration produces a more gradual transition of pressure and velocity around the nose cone. The shock wave formed at the blunt tip is weaker and more diffused, resulting in a smoother pressure distribution. This design provides more thermal protection and better shockwave controllability at high speeds due to the larger separation bubble created by the blunt tip[14]. Consequently, the spherically blunted nose cone is effective in applications where ultimate thermal protection and shockwave impact reduction are prioritized over minimizing drag, such as in hypersonic or re-entry vehicles.

In a study conducted by Girish Kumar and Pravin V. Honguntikar (CFD Analysis of Transonic Flow over the Nose Cone of an Aerial Vehicle, 2015), the three primary nose cone shapes, sharp (conic), ogive, and blunt, were tested. The results showed that the ogive shape presents the least drag, particularly at high speeds [16], making it the most ideal choice among the three tested. This proposes that for the purposes of this project, it is considered to modify or blunt the ogive nose cone while still achieving the desired aerodynamic characteristics to achieve the goal of this project. The ogive shape remains a key consideration in this analysis.

In an analysis conducted by A. Sanjay Varma, G. Sai Sathyanarayana, and J. Sandeep (CFD Analysis of Various Nose Profiles, Int. J. Aerospace Mech. Eng. 2016), different nose cone designs were tested such as the typical Conical, Von Karman, Parabolic, and spherically blunted Ogive. The Von Karman series nose cone demonstrated superior aerodynamic performance,

including a higher critical Mach number and lower pressure coefficient, especially under hypersonic conditions [17]. Similarly, in another study analyzing Bi-Conical, Ogive, typical Conical, and Spherically Blunted Cone nose cones at supersonic speeds, using numerical, analytical, and experimental methods, the ogive-shaped nose cone was found to have better aerodynamic characteristics, while the spherical blunt nose cone displayed poor characteristics [18]. In terms of drag analysis, a study conducted using Ansys Fluent under varying temperature and high-speed velocity conditions revealed that the Von Karman nose cone design creates the least drag in both subsonic and hypersonic regimes [19].

Understanding the study results of aerodynamic characteristics in supersonic/hypersonic flow around different nose cone designs is a critical step in the selection and elimination process for specific configurations, to create and design an ideal model for this project. Given that blunt nose cone designs a42re not typically optimal for high-speed regimes, a thorough analysis and evaluation of individual nose cone features, followed by combining these important features into a blunted or semi-blunted design, provides the most strategic approach for meeting the project's objectives.

1.2.2.2 Analytical and Mathematical Analysis of Shock Wave Formation

When a shockwave forms when a supersonic or a hypersonic encounters a surface or an object with an angle, it is called an oblique shockwave, as demonstrated in Figure 1.4.

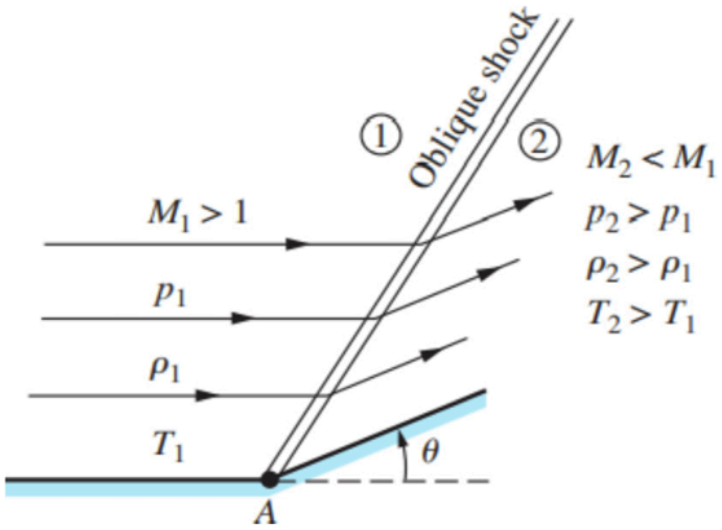

Figure 1.4 - Oblique shock demonstration [20].

The demonstration in Figure 1.4 represents a wall that is tilted with an angle called deflection angle θ at point A, where the flowing fluid, in this case, is air, must be tangent to the wall to ensure that the streamline is also reflected in the same direction of wall deflection caused by the angle θ, which results in an oblique shockwave. When an oblique shock forms, the pressure, flow density, and temperature increase discontinuously, while the Mach number reduces.

One important definition is the wave angle (β), which is the angle between the upstream flow direction and the shockwave, as demonstrated in Figure 1.5. The upstream with a velocity of V_1 and a Mach number of M_1 is directed horizontally while the downstream with a velocity of V_2 and a Mach number of M_2 is inclined upwards due to wall deflection caused by the deflection angle θ.

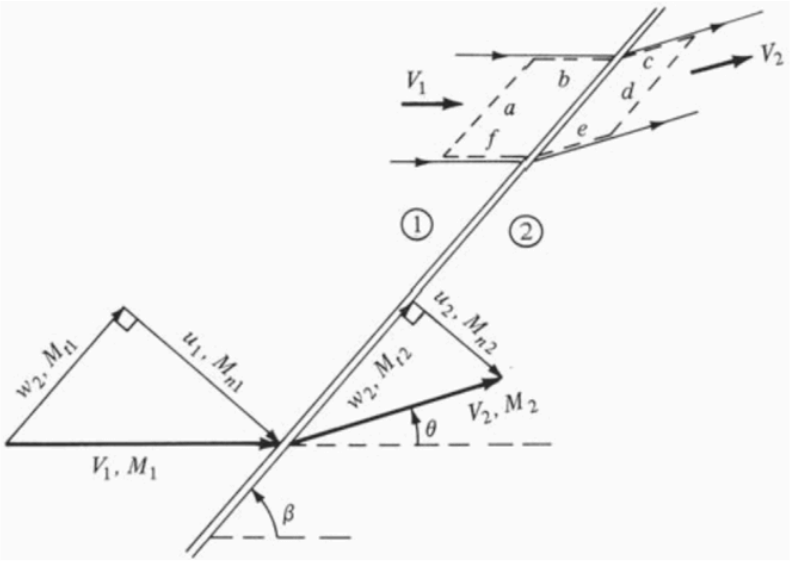

Figure 1.5 - Oblique shock components [20].

The upstream velocity V_1 and the downstream velocity V_2 are both divided into a couple components that are normal and tangential to the shockwave, donated as $w_{1,2}$ & $u_{1,2}$; these components have corresponding tangential and normal number donated as $M_{t,1\ \&\ 2}$ & $M_{n,1\ \&\ 2}$.
In the oblique shock, the tangential velocity component remains constant across the shock [20]. The characteristics are determined solely by the normal velocity component of the wave. The upstream Mach number's normal component is:

$$M_{n1} = M_1 sin(\beta) \tag{1}$$

The downstream Mach number's normal component in terms of M_{n1} is:

$$M_{n1}^{\ 2} = \frac{1+[(\gamma-1)/2]M_{n1}^{\ 2}}{\gamma M_{n1}^{\ 2}-(\gamma-1)/2} \tag{2}$$

The downstream Mach number:

$$M_2 = \frac{M_{n2}}{sin(\beta-\theta)} \tag{3}$$

The density ratio:

$$\frac{\rho_2}{\rho_1} = \frac{(\gamma+1)M_{n1}^{\ 2}}{2+(\gamma-1)M_{n1}^{\ 2}} \tag{4}$$

The pressure ratio:

$$\frac{p_2}{p_1} = 1 + \frac{2\gamma}{\gamma+1}\left(M_{n1}^{\ 2} - 1\right) \tag{5}$$

The Temperature ratio:

$$\frac{T_2}{T_1} = \frac{p_2}{p_1} \times \frac{\rho_1}{\rho_2} \tag{6}$$

Finally, the relationship between the deflection angle θ, wave angle β, and Mach number is:

$$tan(\theta) = 2cot\beta\frac{M_1 sin(\beta)^2 - 1}{M_1^{\ 2}(\gamma + cos(2\beta) + 2} \tag{7}$$

1.3 Project Objectives

This master's project aims to analyze and design an optimized blunt nose cone for surface-to-air guided missiles used in military and defense applications. The focus is on creating a nose cone that performs well aerodynamically at supersonic and hypersonic speeds, ensuring that the flow does not adversely affect critical missile components, such as the canards. By minimizing disturbed flow around the canards and customizing canard placement, the design seeks to prevent control system failures, thereby enhancing the missile's overall stability, response to guidance, and performance at high speeds.

1.4 Methodology

This project has several key objectives, including finalizing the most optimal blunt nose cone designs for guided military missiles. First, it seeks to develop multiple blunt nose cone designs specifically designed to maximize the internal capacity for housing military equipment then rate designs from best to worst. This design optimization will consider various geometric configurations to ensure the missile can accommodate essential payloads while maintaining structural integrity. Second, the study aims to determine the optimal placement of canards to mitigate shockwave-induced flow disturbance. Proper canard placement is crucial for maintaining aerodynamic stability and control, especially at high speeds. Third, the research will utilize CFD simulations to evaluate the aerodynamic performance of different nose cone designs and nose cone-canard configurations. These simulations will provide detailed insights into how different designs interact with airflow and shockwaves. Fourth, the study includes an experimental validation phase, where 3D-printed models of the proposed nose-cone designs will be fabricated and subjected to real-world testing. This phase aims to verify or compare the accuracy of the CFD simulations and refine the designs based on empirical data, the thesis integrates the experimental phase with my efforts to obtain L3 certification, ensuring that the designs meet theoretical and practical performance or compare empirical results with

computational results and sourcing the error factor. A conclusion will be reached regarding the best and most optimal blunt nose cone-canard design for military purposes.

2. The AIM-9 Sidewinder Missile

2.1 AIM-9 Sidewinder Missile Overview

The AIM-9 Sidewinder missile, first introduced in the 1950s, marked a significant advancement in AAM technology. However, its versatility and flexibility of design have led to adaptations for use as a surface-to-air missile (SAM) in certain modified configurations. For example, the MIM-72 Chaparral system was developed by the U.S. Army by modifying the AIM-9 for ground-based launches to defend against low-flying aircraft. Additionally, the RIM-116 Rolling Airframe Missile (RAM) uses modified technology from the AIM-9 for naval point-defense purposes. The ease of modifications highlights the Sidewinder's ability to effectively perform in both AAM and SAM configurations to fulfill the evolving over the decades to remain the weapon of choice in modern aerial combat [21].

The U.S. Navy led the first development of an operational heat-seeking missile to get around the limitations of radar-guided weaponry in close-range dogfights [22]. The Sidewinder was developed in response to the need for a lightweight, high-maneuverable missile that is capable of targeting high-speed aircraft using infrared homing. This marked a drastic shift from radar-guided weaponry, which was bulky and less effective in combat scenarios dynamically [21]. For instance, The AIM-9A adopted a simple seeker head with a constrained tracking range and a relatively small warhead. In its early trials, the missile outperformed its radar-guided contemporaries in maneuverability and simplicity of operation, despite its simple design [22].

During the Vietnam War, the AIM-9B variant showed its high levels of effectiveness by engaging MiG fighters at total ranges of up to 18,000 feet. However, operational reports revealed weaknesses and vulnerabilities in its seeker head to heat sources other than the intended targets, which could be confused by aircraft engine flares or sunheat[23]. This problem led to promising upgrades of the design to develop the AIM-9D, which adapted a cooler to its infrared seeker for better sensitivity, and the AIM-9E, which adapted a more advanced control system to improve overall performance. As air combat tactics develop, so do the missile's design principles, with enhanced propulsion systems and avionics [24]. When the AIM-9L was initially released in the late 1970s, it marked a major leap forward in the missile development sector, becoming the first all-aspect variant capable of locking onto targets from all angles, not just from the rear [25]. This development significantly increased its adaptability in contemporary air combat, as seen by its several kills against Argentine aircraft during the Falklands War [24].

Additional refinements were made in the early 2000s to solidify Sidewinder's reputation as one of the most successful and effective AAM/SAM in military history. The AIM-9X is equipped with an improved infrared seeker that tracks stealthier targets, thrust vectoring for enhanced maneuverability, and compatibility with modern helmet-mounted display systems. The AIM-9's extensive developmental history, from its initial, basic design to its advanced contemporary versions, highlights its flexibility in responding to the evolving aerial combat environment.

Military historians claim that the Sidewinder's remarkable success may be attributed to its ease of use, reliability, and versatility across a range of aircraft and surface platforms. As a result,

it has become an indispensable part of contemporary air forces throughout the globe. Its continuous development highlights the significance of small-step technology advancements supported by thorough testing and input from combat situations. [26].

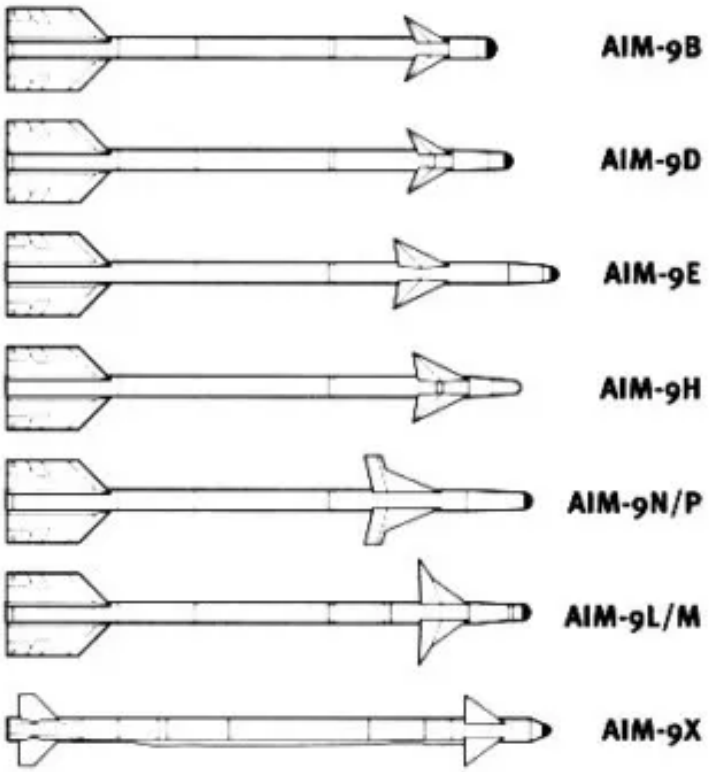

Figure 2.1 - Variations of the AIM-9 Sidewinder [27]

2.2 AIM-9 Sidewinder Components

2.2.1 Overall Components

The most important aspect of designing components for the AIM-9 Sidewinder missile is achieving a balance between maneuverability, guidance accuracy, effective controls, reliability, and simplicity. At the heart of the design, the missile's infrared seeker must be reliable enough to lock onto the heat signature of an enemy aircraft effectively while ignoring confusing inputs like flares, making the guidance system a deal-breaking component. The aerodynamic design has equal significance, since the missile's fins, wings, and Rolleron assembly provide stability while enhancing maneuverability, allowing it to adjust its flight path rapidly to intercept fast-moving targets.

The missile's ability to achieve supersonic speeds and burst controllably upon proximity to its target requires the propulsion system and warhead to perform reliably under extreme conditions. The missile's versatility is further enhanced by the modularity of components like

mounting systems and umbilical cables, which make it simple to integrate with a variety of platforms. Another significant aspect is that the Sidewinder's straightforward construction allowed for easy maintenance and cost-effective mass manufacture, making it one of the most durable and widely employed AAM in military history. The general components layout of the AIM-9 Sidewinder can be broken into the following:

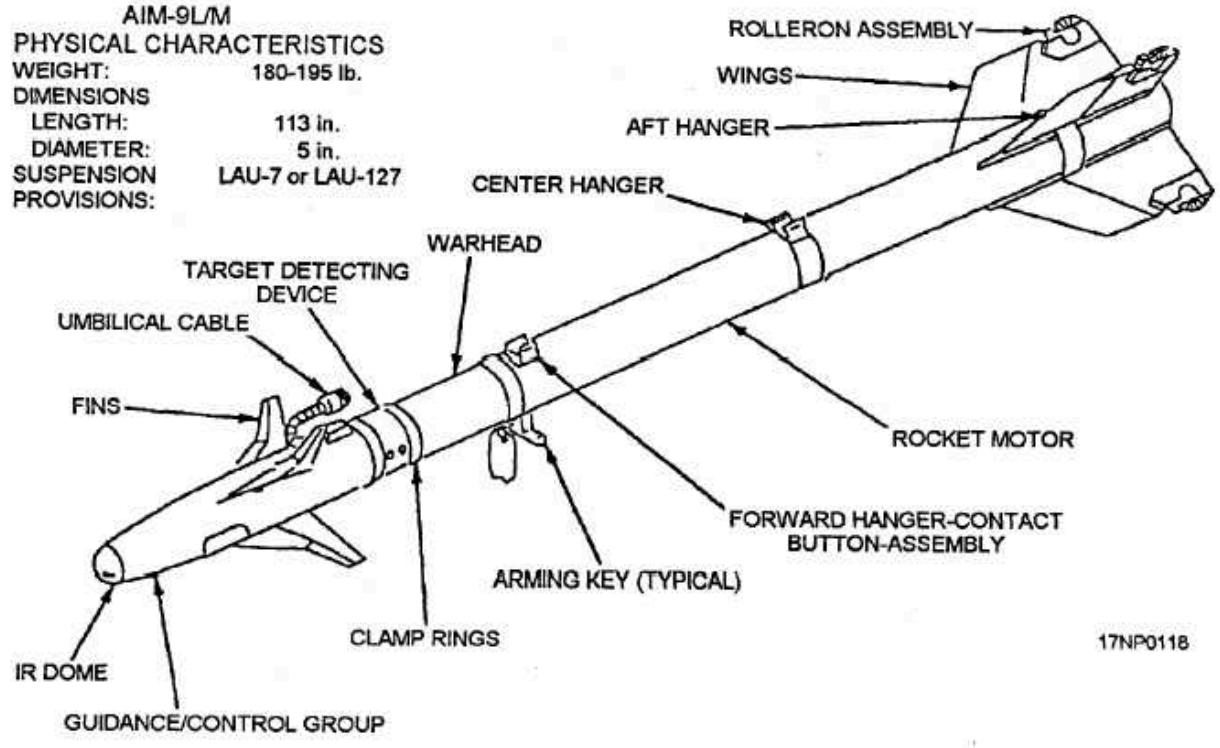

Figure 2.2 - AIM-9 Sidewinder general components [28]

IR Dome: The infrared (IR) seeker dome lays at the front of the missile, which houses the infrared sensor or the guidance system responsible for tracking the target. The sensor detects the heat signature from the target, typically an aircraft's engine exhaust, and guides the missile toward that heat signature. The sensitivity and accuracy of this tracking system is crucial for the missile's reliability, as it allows the Sidewinder to track and strike high-speed targets in dynamically combated scenarios.[29]

Figure 2.3 -Sidewinder infrared dome [30]

Guidance/Controls Unit: This component primarily focuses on receiving and processing data from the IR seeker and guiding the missile to its target. This system involves avionics and processors that interpret the heat inputs detected by the IR seeker and convert that data into instant real-time adjustments to the missile's flight path. These adjustments are made by the control surface response which is manipulated by the guidance component, like the fins and Rollerons, to ensure the effective missile engagement to pursue and strike the target. [31]

Canards/Fins: Canards are one of the most critical components of the missile, and the focus of this project. They are small aerodynamic surfaces located at the front of the missile that stabilizes and controls its flight path by responding to the guidance system instantaneously. Once the infrared seeker locks onto a target, the guidance unit uses the canards to quickly engage to target and adjust the missile’s direction towards it, ensuring the lock is maintained. The canards are also responsible for controlling the missile's pitch and yaw degrees of freedom, allowing it to make instant course corrections and stay on a direct path toward the target, even during high speeds. [32]

Figure 2.4 -Sidewinder canards [33]

Umbilical Cable: This cable is a connector of the missile to its launching aircraft/pad before launch. This cable serves as the main connection between the missile and the launching aircraft or a launch pad, allowing for the transfer of power and communication signals until the moment of launch. The umbilical cable disconnects when the missile is fired.

Target Detecting Device: This device is responsible for assuring that the warhead causes an explosive impact at the optimal moment to inflict maximum damage on the target. This device typically operates using proximity fuzes or contact sensors. A proximity fuze works by sensing when the missile is within a certain designated range close to the target, by analyzing IR signals from the Guidance/Controls unit to detect the distance between the missile and the target. This allows the warhead to explode when it is close enough to the target to cause significant damage, even without a direct hit.

Clamp Rings: This is a structural component of the missile that securely holds various sections of the missile together, this component must withstand significant forces during launch and flight without experiencing fatigue. The ring's purpose is to ensure that the missile's internal systems such as the warhead, guidance unit, and thruster, remain tightly connected throughout the stages of handling, storage, launch, and flight.

Arming Key: The arming key is a critical safety mechanism in the AIM-9 Sidewinder missile system, it ensures that the missile remains safe to handle during storage and transport. This is especially important during direct interactions between humans and the missile, such as when

mounting it on the aircraft or setting it up on the launch pad. When the missile is ready for deployment, the arming key is removed or disengaged, transitioning the missile into its operational state.

Figure 2.5 -Sidewinder's arming key and clamp rings [34]

Warhead: This is the explosive charge of the missile, which is responsible for delivering the destructive force or material necessary to paralyze or destroy the target when it is within close proximity. In the Sidewinder, the warhead is typically an annular blast fragmentation type, which is designated to maximize damage by projecting a ring or cloud of high-velocity fragments when it activates or detonates, which is effective against fast-moving targets.

Center Hanger: This is part of the mounting and security system that is used to attach the missile to the aircraft or a launching pad. It helps to hold the missile securely in place during positioning the missile and during flight until it is launched.

Aft Hanger: Very similar to the center hanger, the aft hanger's purpose is to attach the missile to the aircraft or the launching pad and provide rear support, to ensure the missile's stability on the aircraft during flight.

Rocket Motor: This key component is designated to provide the necessary propulsion to accelerate the missile toward its target after launch. The rocket motor typically used is a solid fuel, which is considered to be a good choice due to its stability during flight, safety to handling, and storage durability for long periods without significant degradation. Once the rocket motor is ignited, the solid fuel burns quickly to generate a powerful thrust that propels the missile to supersonic speeds, typically over Mach 2.5.

Figure 2.6 -Sidewinder's Rocket Motor [35]

Forward Hanger-Contact Button Assembly: This launch system component serves both structural and electrical roles. As it's located toward the front of the missile, the hangar assembly helps securely attach the missile to the launch rail of the aircraft or launch pad and maintains electrical connections between the missile and the aircraft's/launcher's systems. This ensures stability and activation during takeoff, flight, and pre-launch stages.

Rolleron Assembly: This unique stabilization system is made of small, aerodynamic wheels located at the trailing edges of the missile's wings. Their primary use is to control the missile's roll motion during a straight flight path, which refers to the rotation of the missile around its longitudinal axis, ensuring it maintains stability and executes the mission flawlessly.

Wings: These larger aerodynamic surfaces are located toward the rear of the missile, and they play an essential role in providing stability, lift, and control during flight. The wing's primary purpose in a missile is to maintain its overall trajectory and balance as it travels toward the target by controlling its rolling and lateral movements. The sufficient lift generated by the wings helps the missile maintain stability and altitude, even at supersonic speeds.

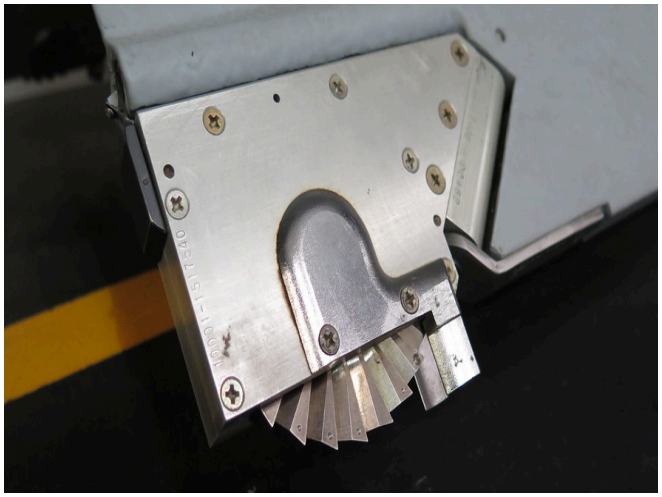

Figure 2.7 -Sidewinder's rolleron [36]

Figure 2.8 -Sidewinder's wings [37]

2.2.2 Project's Critical Components

Since the main objective of this project is to optimize a nose cone design that meets the essential requirements for supersonic flight without compromising the performance of the canards, the nose cone design is an extremely critical component for this project, as it directly influences the flow characteristics around the canards, which are the second critical component of this project. To ensure ideal performance, the nose cone will be carefully refined and optimized to achieve a blunt design that provides a steady flow around the canards. Subsequently, the placement of the canards will also be optimized to achieve the ideal combination of nose cone design and canard positioning, fulfilling the mission's goals for supersonic performance.

Nose cone optimization is the first priority of this project since its design defines the flow around the missile's active components and determines the overall aerodynamic characteristics. A blunt nose cone generates a bow shock which is an undesirable flow phenomenon defined as an abrupt change in pressure, density, and temperature when supersonic flow encounters a body. This occurs when the flow requires a deviation angle that exceeds the maximum reachable angle for an attached oblique shock, as illustrated in Figure 2.3.

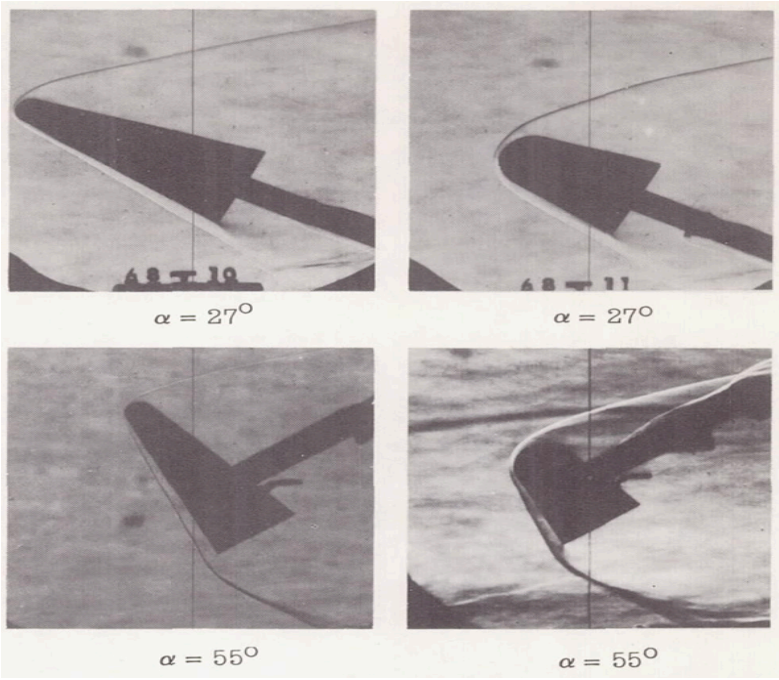

Figure 2.9 - Blunt nose cone bow shock wave formation at different AOA [38]

The canard is the second most critical component for this project because of its priority since any disturbance of the flow around it can significantly degrade the missile's aerodynamic overall performance, leading to instability, reduction of control effectiveness, and excessive drag, which compromises the overall efficiency of the missile during supersonic flight. Therefore, the second project's main objective is to find the optimal placement of the canards, ensuring they operate in minimal disturbance flow conditions to contribute to the success of the supersonic mission.

2.3 Sidewinder Missile Geometry

2.3.1 True-Size Geometry

Due to the classified nature of military hardware, detailed blueprints or diagrams of the exact geometry of all the Sidewinder missiles are not publicly published; releasing such classified technical information could compromise national security by revealing design specifics that adversaries might take advantage of. The military often restricts access to detailed schematics to prevent unauthorized development or replication of the technology. However, general geometric specifications are accessible through open sources such as official military publications and public aerospace databases. These sources provide an overall idea of the missile's basic dimensional specifications without disclosing any details. The information gathered in the following table compiles these publicly available geometric and performance specifications of the AIM-9 Sidewinder or Canard-controlled missiles generally:

Table 2.1 – AIM-9 Sidewinder general parameters [39,40,41]

Total Length	2.870 m (114 inches)
Diameter	0.127 m (5 inches)
Wingspan	0.630 m (24.8 inches)
Total weight	83.300 kg (188 lb)
Warhead Weight	9.4 kg (20.8 lb)
Control Surface Type	Cruciform canards with rollerons
Maximum speed	Mach 2.5+
Operational Range	1.6 to 35.4 km - (1 to 22 miles)
Canard Configuration	Delta fins near the nose, cruciform tail fins
Guidance System	Infrared homing
Propulsion System	Solid-propellant rocket motor

The Sidewinder missile's thoughtfully engineered geometry is a crucial factor in its exceptional performance since it's optimized to enhance both aerodynamics and maneuverability during supersonic flight. One main advantage of its design is its compactness and lightweight structure, which allows for versatile mounting on a wide variety of aircraft without impacting the overall performance [34]. Additionally, the missile's cruciform canard configuration, combined with rolleron-equipped tail fins, provides superior maneuverability, enabling rapid course adjustments that are crucial for dogfights and close-ranged engagements [42].

2.3.2 Scaled Geometry

The document titled *"Canard-Controlled Missile at Supersonic Mach Numbers"* by A. B. Blair, Jr., Jerry M. Allen, and Gloria Hernandez served the project by being a rich reference for the scaled geometry used in this section, which will be used further in this project. The document takes an interest in the aerodynamic characteristics of a canard-controlled missile at supersonic speeds, focusing on a variation of the Sidewinder missile that closely aligns with the missile type chosen for this project. For the project's final design, the geometry from the document has been further scaled to meet the minimum requirements for an L3 rocket, ensuring both structural integrity to withstand thrust and the forces generated during supersonic flight. The following geometry will be considered for further validation through both CFD simulations and real-life testing:

Table 2.2 – Project's scaled geometry

Component	Dimension
Total Length	1.841 m (72.49 inches)
Front section length (to hinge line)	0.398 m (15.69 inches)
Nose cone length	0.171 m (6.75 inches)
Midsection length	0.284 m (11.19 inches)
Distance from nose tip to moment center	0.829 m (32.63 inches)
Canard span (height)	0.130 m (5.13 inches)
Canard placement (distance from the tip)	0.485 m (19.08 inches)
Missile's Diameter	0.076 m (3.00 inches)
Rear fin section length (from tail)	0.328 m (12.90 inches)
Tail length (including rear fins)	0.388 m (15.29 inches)
Hinge line distance from the tip	0.398 m (15.69 inches)
Distance between rear fins and tail	0.061 m (2.39 inches)
Thickness of the Canard	0.0051 m (0.20 inches)
Canard Top Section's Length	0.060 m (2.36 inches)
Canard's Section Total Height	0.026 m (1.03 inches)
Overall Canard Height	0.130 m (5.13 inches)
Canard's bottom section's Length	0.20 m (7.88 inches)
Canard's Front Section's Length	0.114 m (4.50 inches)
Sweep Angle of Canard	47.10 degrees

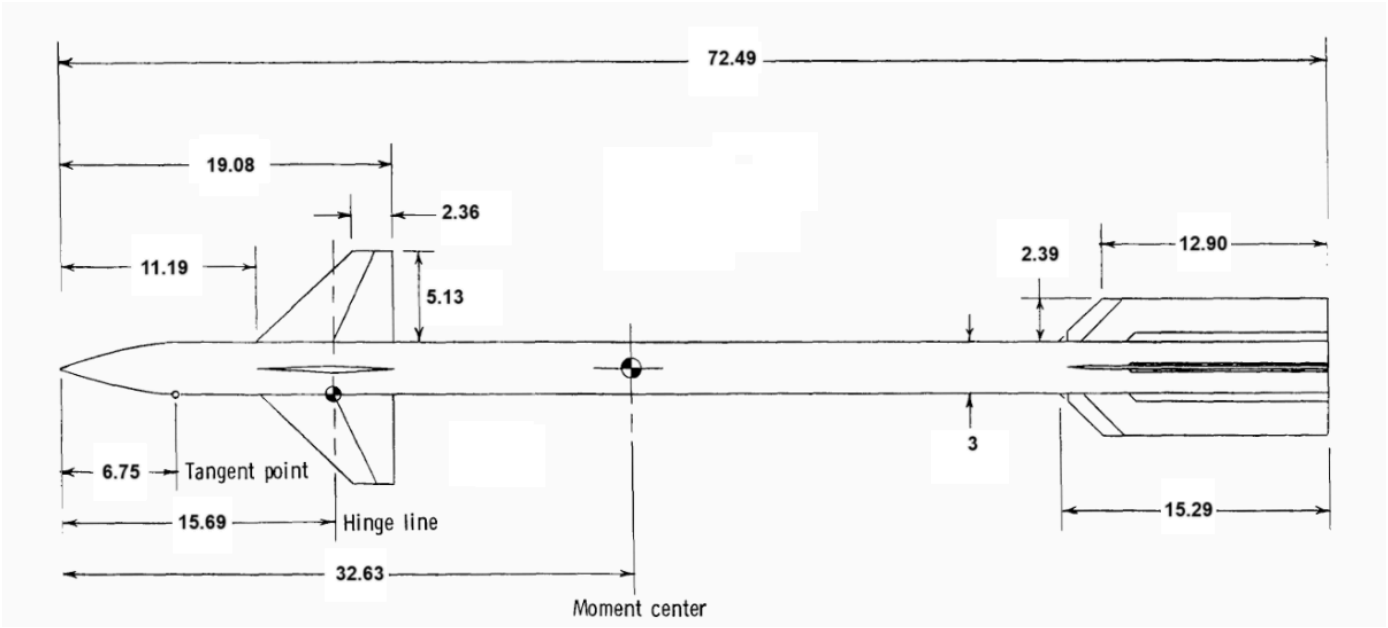

Figure 2.10 - Project's scaled design in inches. [36]

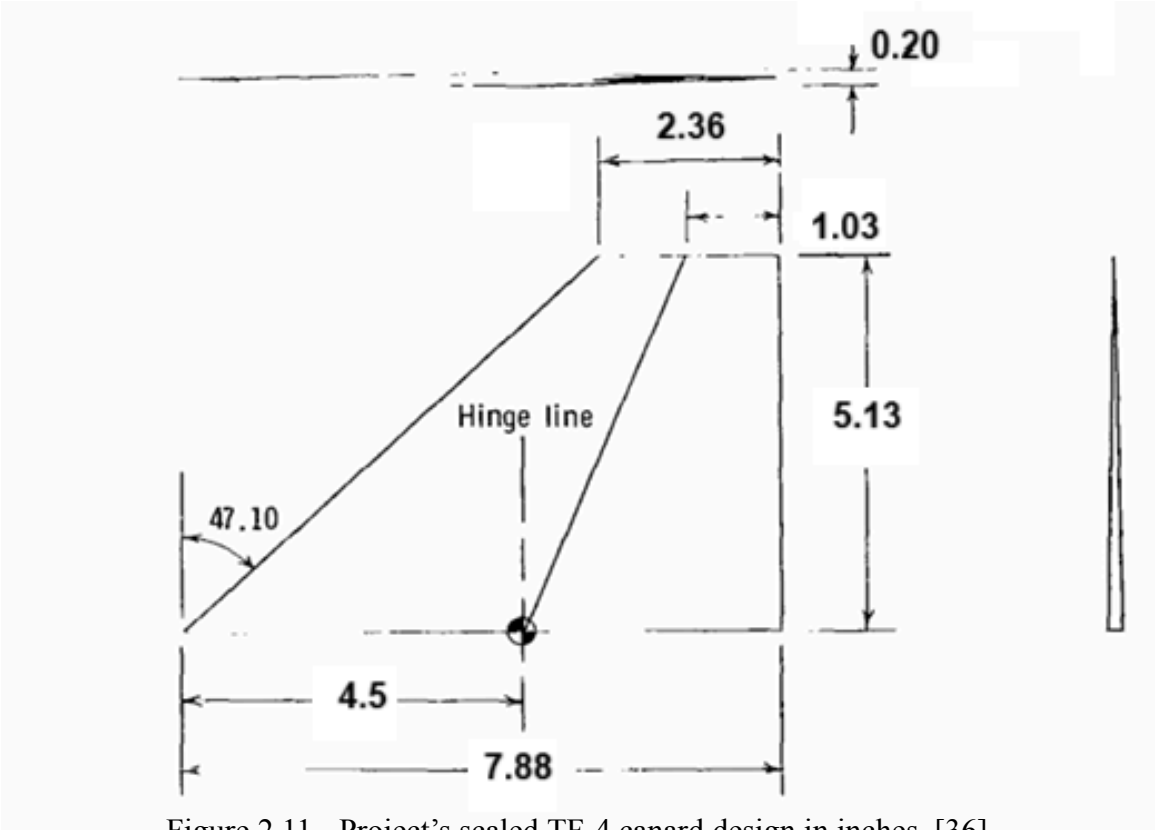

Figure 2.11 - Project's scaled TF-4 canard design in inches. [36]

Figure 2.12 - Project's scaled design side view.

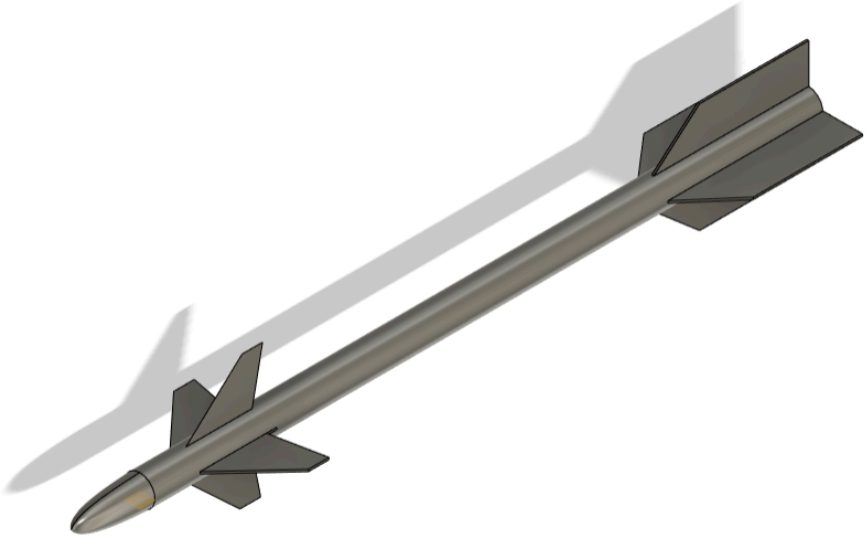

Figure 2.13 - Project's scaled design isometric view.

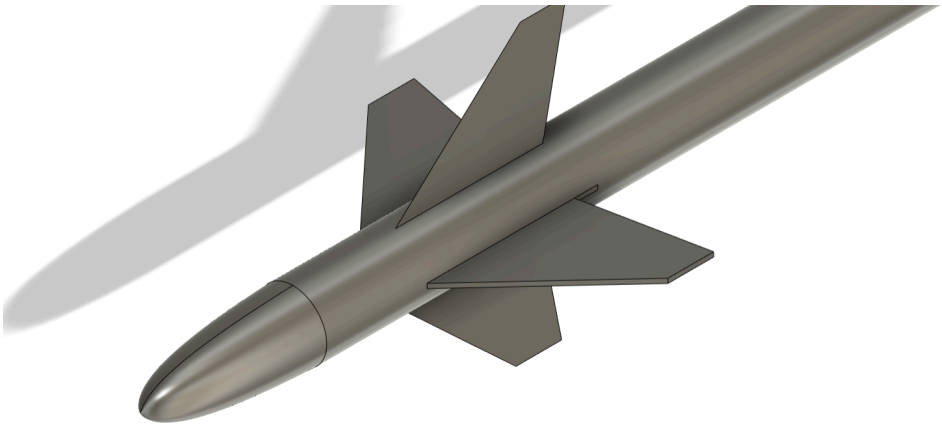

Figure 2.14 - Project's scaled design nose cone-canard system.

2.4 Design Implementation

For the flow analysis study that is required to achieve the project's primary objectives, developing a CAD model optimized for CFD simulations, along with the physical missile for the proof-of-concept phase, is essential. The project also aims to obtain a Level 3 rocketry certification which requires further optimizations and refinement to meet the basic requirements of the certification process, while validating the core design concept. The process of scaling the design to accommodate an L3 propulsion system was finalized in section 2.3, and the scaled-down model will serve as the foundation for further aerodynamic analysis moving forward in this project.

2.4.1 Overall Execution

For the purpose of testing and flow analysis using CFD, the CAD design will mainly characterize the external geometry of the Sidewinder missile. Detailed design considerations such as the internal components, weight distribution, and stability will be developed further on with the project using OpenRocket and RASAero II.

One of the basic requirements for stability and control is securing the distance between the center of gravity (CG) and the center of pressure (CP) to be at least 2 calibers, where one caliber is defined as the diameter of the rocket body. This 2-caliber separation ensures that the CG is ahead of the CP, providing a good stability margin for a basic missile design. Such a margin naturally stabilizes the missiles from minor disturbances during the vertical flight without losing stability. A 2-caliber CG-CP distance also displays a balance between stability and control; It prevents the missile from being too stable, which would make it difficult to steer, and prevents it from being too unstable, which would make it uncontrollable. This separation ensures that the missile remains stable while still being responsive to steering inputs and external factors.

Later in the design execution process, the missile's internal components and subsystems will be carefully designed and chosen under the supervision of the project advisor and a rocketry expert professor in the Department of Aerospace Engineering at San Jose State University.

The physical construction of the missile has been designed to meet all safety requirements for civil flight and launch testing while withstanding the forces generated by the L3-certified propulsion system, which involves motors of M-class or higher (with 5,120 Newton-seconds of total impulse or more). The nose cone will be 3D printed using carbon fiber-infused PETG, chosen for its high strength-to-weight ratio, and it will house pressure sensors for aerodynamic testing on its exterior. Canards will also be made of carbon fiber-infused PETG, due to its lightweight yet strong control surfaces capable of withstanding significant aerodynamic forces and will have pressure-sensors housing as well to fulfill the purpose of the study. The body tube will be made of fiberglass to ensure RF transparency, which is critical for maintaining communication and tracking signals. The wings will be fabricated from carbon fiber plates with fiberglass layering to provide rigidity to the design, while the couplers and centering rings will also be made from fiberglass to handle compression forces and ensure secure section alignment. The avionics bay will be 3D printed and reinforced with fiberglass for durability, ensuring the protection of the sensitive electronics and communication components during flight. The

recovery system will utilize a parachute purchased from Fruity Chutes, known for its reliability in high-power rocketry, and the motor retainer case will be sourced from Wildman Rocketry, offering a secure and robust retention system for high-power motors. To validate the design, the missile will be fitted with at least 10 custom pressure sensors on the nose cone and canards to analyze pressure distribution and shockwave interactions during flight. This data will help optimize aerodynamic performance, and the final nose cone design will be chosen based on the best results from CFD simulations, ensuring minimal drag and optimal pressure management.

2.4.2 Design Challenges

One of the main design challenges is the strategic placement of pressure sensors across the missile in the nose cone-canard configuration. Proper sensor distribution is critical to accurately capture pressure variations and have a comparative study based on it, and the choice of sensors must align with the mission objectives which is to measure speed and dynamic pressure at specific flight conditions. The sensors must be selected to handle the expected range of dynamic pressures during high-speed flight, ensuring reliable and accurate data collection.

Additionally, another significant challenge involves the design of the canards. To meet L3 certification requirements and ensure a safe test of the missile design, the canards must be minimized as much as possible. This is due to the fact that L3 rocket certifiers view inactive canards as a potential safety hazard, as they can affect the stability of the rocket during flight. Therefore, the design must balance aerodynamic performance while adhering to certification guidelines, ensuring that the canards do not compromise stability or safety.

3. Nose Cone Choices and Evaluation

3.1 AIM-9 Sidewinder Missile Nose Cone

3.1.1 AIM-9 Sidewinder Missile Nose Cone Overview

The Overall design of the AIM-9 Sidewinder missile nose cone is designed specifically to perform in supersonic regimes; Its conical geometry, with a rounded tip, is specifically optimized to reduce drag while maintaining the required margins of stability. At supersonic speed, a conical shape produces oblique shockwaves, which are less intense than bow shocks and result in lower wave drag. Additionally, the rounded tip smoothens the transition between shock layers, mitigating stagnation point heating. This overall design ensures a sufficient balance between aerodynamic efficiency and thermal durability at supersonic speeds. By using experimental wind tunnel data and Navier-Stokes solvers on the current AIM-9 Sidewinder missile nose cone, numerical simulations have shown that this design maximizes laminar flow across the missile body and reduces boundary layer separation [43] which further enhances localized heating challenges by distributing thermal loads, which is essential for supersonic flight durability [44].

Supersonic missiles like the AIM-9 Sidewinder are subjected to significant aerodynamic heating, with stagnation temperatures reaching 1000–1500 K during flight at Mach 2.5 -- 3.0, with that, the nose cone must withstand such extreme conditions without compromising structural or functional integrity. Titanium alloys, which are used for the structural shell, provide a high melting point of around ~1650°C, and it is known for its strong resistance to thermal stress, while sapphire, which is utilized in the seeker dome, keeps its transparency at high temperatures [44]. To further reduce heat loads in the nose cone, protective coatings are used such as high-temperature ceramics or ablative materials, which keep seeker electronics functioning, which either restrict heat conduction or disperse heat by controlled ablation.

The seeker dome at the tip of the AIM-9 nose cone houses the infrared (IR) seeker, which is a critical component for tracking heat signatures emitted by target aircraft engines. Sapphire is the preferred material for the dome due to its optical properties, including superior transmittance in the IR spectrum, specifically in the 3–5 μm and 8–12 μm wavelength ranges. Additionally, sapphire offers exceptional thermal stability that is capable of withstanding temperatures up to ~2000 K, and outstanding resistance to mechanical erosion, making it a preferred choice for high-speed, high-temperature flight envelopes. The seeker dome's curvature is optimized using ray-tracing algorithms to minimize optical aberrations and enhance the accuracy of target acquisition. The dome must also withstand aerodynamic pressures of up to ~100 kPa while maintaining optical clarity. The seamless integration of the dome with the surrounding aerodynamic shell reduces interference from shockwave-induced optical distortions, ensuring consistent IR signal fidelity [45].

The structural design of the AIM-9 Sidewinder missile nose cone combines lightweight materials with high strength and thermal resistance. The Titanium alloy used in the outer shell also provides the strength required to withstand all the aerodynamic forces that the missile is experiencing in a supersonic flight and protect the seeker system from external shocks. The structural elements are carefully chosen to ensure smooth transitions between components,

avoiding stress concentrations that could lead to failure [44]. To manage the combined aerodynamic and thermal loads, the sapphire dome is securely attached to the metal shell using a combination of adhesive and mechanical fasteners. This dual approach ensures an airtight seal while allowing for the differing thermal expansion rates of the two materials, preventing stress-induced failure during operation [49].

3.1.2 AIM-9 Sidewinder Missile Nose Cone Design Optimization Considerations

Optimizing the AIM-9 Sidewinder missile nose cone design to incorporate a blunted shape requires a careful optimization plan and extensive consideration of aerodynamic, thermal, and functional trade-offs. A blunted nose cone will reduce the intensity of stagnation point heating, dispersing thermal loads more effectively and lowering peak temperatures experienced during supersonic flight. However, this modification increases wave drag compared to the original conical design, potentially reducing overall aerodynamic efficiency in high-speed flights. Computational fluid dynamics simulations must be used and analyzed to evaluate the impact of the altered shockwave structure on missile stability and drag, which is a key objective of this project. Additionally, the modified geometry could influence the field of view and optical clarity of the infrared seeker housed in the dome. The seeker's performance would need to be reassessed to ensure it can operate effectively with the new optimized nose cone design, possibly requiring adjustments to the curvature or refractive properties of the sapphire dome. Structural considerations, such as material compatibility and stress redistribution due to thermal and aerodynamic loads, must also be addressed to maintain durability and functionality. Ultimately, the optimization process must balance these factors to achieve enhanced thermal management without compromising the missile's aerodynamic performance or targeting accuracy.

3.2 Optimized Nose Cone Designs

3.2.1 Blunted Elliptical Nose Cone

3.2.1.1 Blunted Elliptical Nose Cone Choice Discussion

Elliptical nose cones are commonly used in aerospace applications due to their efficient aerodynamic performance, balanced thermal distribution, and smooth flow characteristics. In mathematical terms, this shape is defined as a segment of an ellipse rotated around its central axis. It features a rounded tip and smooth transitions, making it highly effective at reducing drag and maintaining a laminar flow pattern around it, especially at supersonic speeds. The profile of the 2D shape on this nose cone represents one-half of an ellipse, where the major axis corresponds to the centerline and the minor axis is defined as the base of the nose cone. When the entire ellipse is rotated about its major axis, it forms a prolate spheroid, making the elliptical nose cone more accurately a prolate hemispheroid. This geometry is favored in model rocketry because of its blunt tip and tangent base, which are advantageous in subsonic conditions. Additionally, if the major axis equals to the nose cone length (L), the shape becomes a hemisphere.

$$y = R\sqrt{1 - \frac{x^2}{L^2}} \tag{8}$$

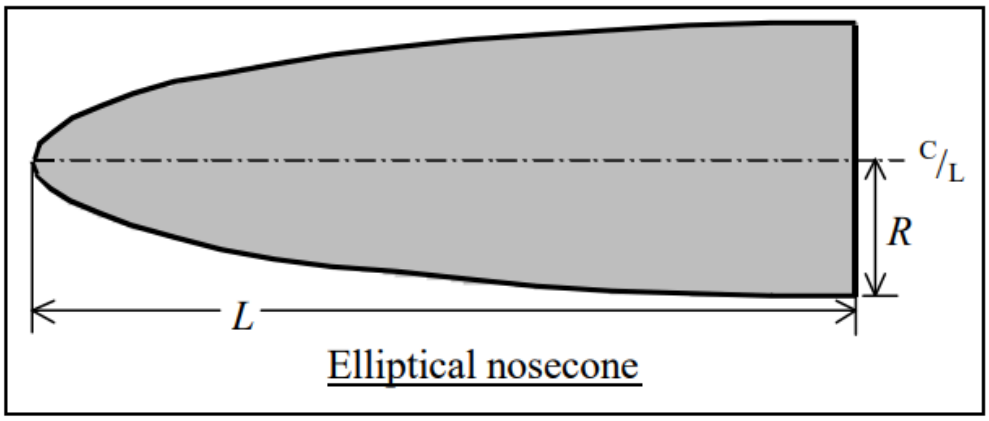

Figure 3.1 - Elliptical nose cone [46]

Advantages of Blunted Elliptical Nose Cones: Choosing a blunted elliptical nose cone for optimizing the AIM-9 Sidewinder missile could potentially provide a scientifically solid solution for supersonic flight challenges, by providing aerodynamic efficiency, thermal resilience, and effective seeker performance. The overall elliptical shape of the nose cone, defined by its gradual curvature, reduces wave drag by generating weaker oblique shockwaves rather than intense bow shocks typical of blunt or spherical designs. This results in a significantly lower drag coefficient on the overall nose cone, which directly improves the missile's speed and range, which is also the main objective of this project. At supersonic speeds, the blunted tip distributes stagnation point heating over a wider surface area which mitigates the peak thermal flux effectively. The heat transfer rate at the stagnation point is reduced as the larger radius of the nose cone's curvature lowers the aerodynamic heating, which plays a critical factor in structural integrity maintenance under extreme thermal loads.

The smooth elliptical geometry transitions effectively maintain laminar flow for a longer distance along the missile body, delaying flow separation and reducing pressure drag, which is a key objective in this project if the challenge is to have an effective flow around the canards. This delay in airflow separation enhances the missile's stability and maneuverability, critical in high-speed engagement scenarios like the typical missions for the Sidewinder AIM-9. The elliptical nose cone further accommodates the infrared seeker system and avionics by minimizing aero-optical distortions. The gradual curvature also stabilizes the shock layer, reducing density and temperature gradients that can interfere with infrared signal transmission. This ensures the seeker dome, which is made of sapphire, maintains a high transmittance in the IR spectrum while withstanding extensive aerodynamic pressures and thermal loads.

Structurally, the blunted elliptical design distributes aerodynamic forces evenly across the entire nose cone, avoiding stress concentrations that can lead to material and structural failure. The use of advanced materials, such as titanium alloys and adhesives for the outer shell and sapphire for the seeker dome would enhance durability while maintaining the missile's lightweight requirements.

Disadvantages of Blunted Elliptical Nose Cones: While blunted elliptical nose cones offer multiple advantages in terms of thermal management and flow stability compared to other designs, they also present challenges when applied to supersonic flight for missiles like the one that the project takes care of. One main disadvantage is the compromise of certain aerodynamic aspects when compared to sharper designs, such as conical or parabolic nose cones. Although it reduces wave drag relative to blunt or spherical geometries, the broader frontal area of the blunted elliptical profile generates more wave drag than sharper profiles in the nose tip. This trade-off can slightly reduce the missile's range, which is particularly critical for designs focused on maximum performance and mission execution.

Another disadvantage is the sensitivity to flow separation under certain flight conditions. Although the elliptical nose cone geometry produces smoother transitions and delays in boundary layer separation, extreme flight maneuvers or high angles of attack could still disrupt the airflow around the canards, affecting their stability. This may require additional compensatory measures in the missile's control surfaces or tail design, potentially a topic we could get to if necessary when it comes to optimizing canard placement.

For thermal distribution, while it is beneficial for reducing peak stagnation point heating, it redistributes heat over a larger surface area, which means there will be further requirements for expanded or reinforced thermal protection systems, which can add weight and complexity to the overall design. Additionally, achieving the precise elliptical curvature and smooth transitions required for missile performance requirements can introduce manufacturing challenges. Advanced manufacturing techniques, such as CNC machining or additive manufacturing, may increase production costs compared to simpler nose cone shapes.

Lastly, the mission-specific trade-offs must be considered. While a blunted elliptical nose cone is ideal for designs prioritizing thermal resilience and stability, it may not align with applications requiring peak speed or minimal drag, such as hypersonic missiles or those optimized for very long ranges. Thus, while the blunted elliptical design offers a balanced solution, it requires careful integration and optimization to mitigate these disadvantages effectively.

3.2.1.2 Blunted Elliptical Nose Cone Choice Design

The decision to select the Blunted Elliptical Nose Cone for this project, despite its disadvantages, comes from its balance of aerodynamic efficiency, thermal resilience, and design flexibility. While it is true that the design has inherent drawbacks, such as higher wave drag compared to sharper profiles like conical or parabolic nose cones, these challenges are offset by its numerous advantages and alignment with the project's objectives. The blunted elliptical shape offers a unique combination of reduced stagnation point heating and smooth flow transitions, both of which are critical for the performance and survivability of a supersonic missile like the AIM-9 Sidewinder. This shape is also well-suited for this project as it offers a sweet balance of reduced wave drag and effective thermal management, addressing two critical challenges in supersonic flight. Additionally, the elliptical design is versatile and can be easily customized, 3D printed, and experimentally tested, streamlining the iterative design and validation process.

The CAD design for CFD testing was created effortlessly using the equation for the Blunted Elliptical Nose Cone shape, which was seamlessly implemented in the CAD software. This shape, defined by an ellipse rotated about its major axis, forms a prolate spheroid, making the elliptical nose cone more accurately described as a prolate hemispheroid. Given that the base diameter is 3 inches and the nose cone length is 6.75 inches, as determined in the previous section, the equation used to trace the shape of the nose cone for this project is as follows:

$$y = 1.5\sqrt{1 - \frac{x^2}{6.75^2}} \tag{9}$$

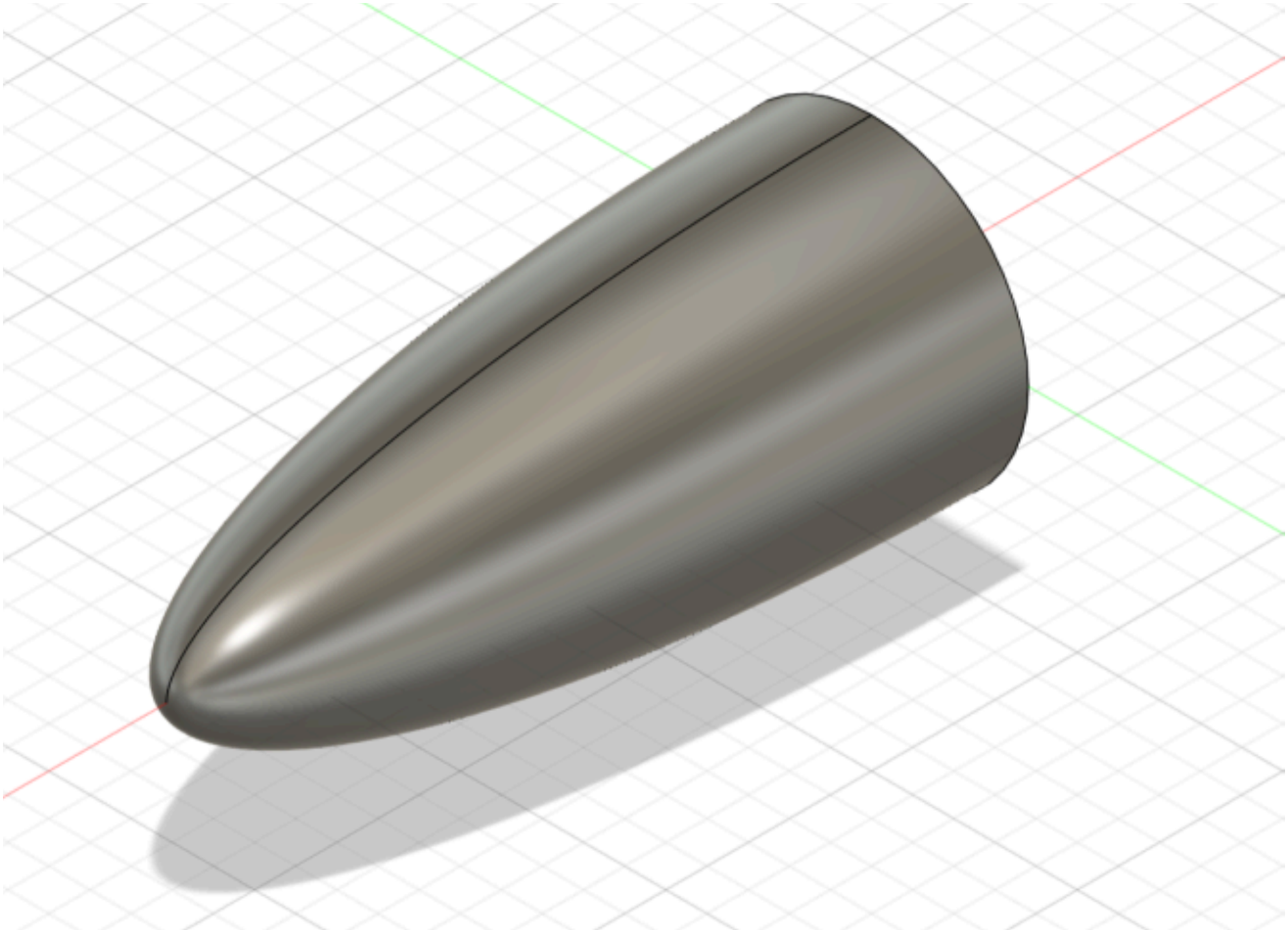

Figure 3.2 - Isometric view of the project's blunted elliptical nose cone

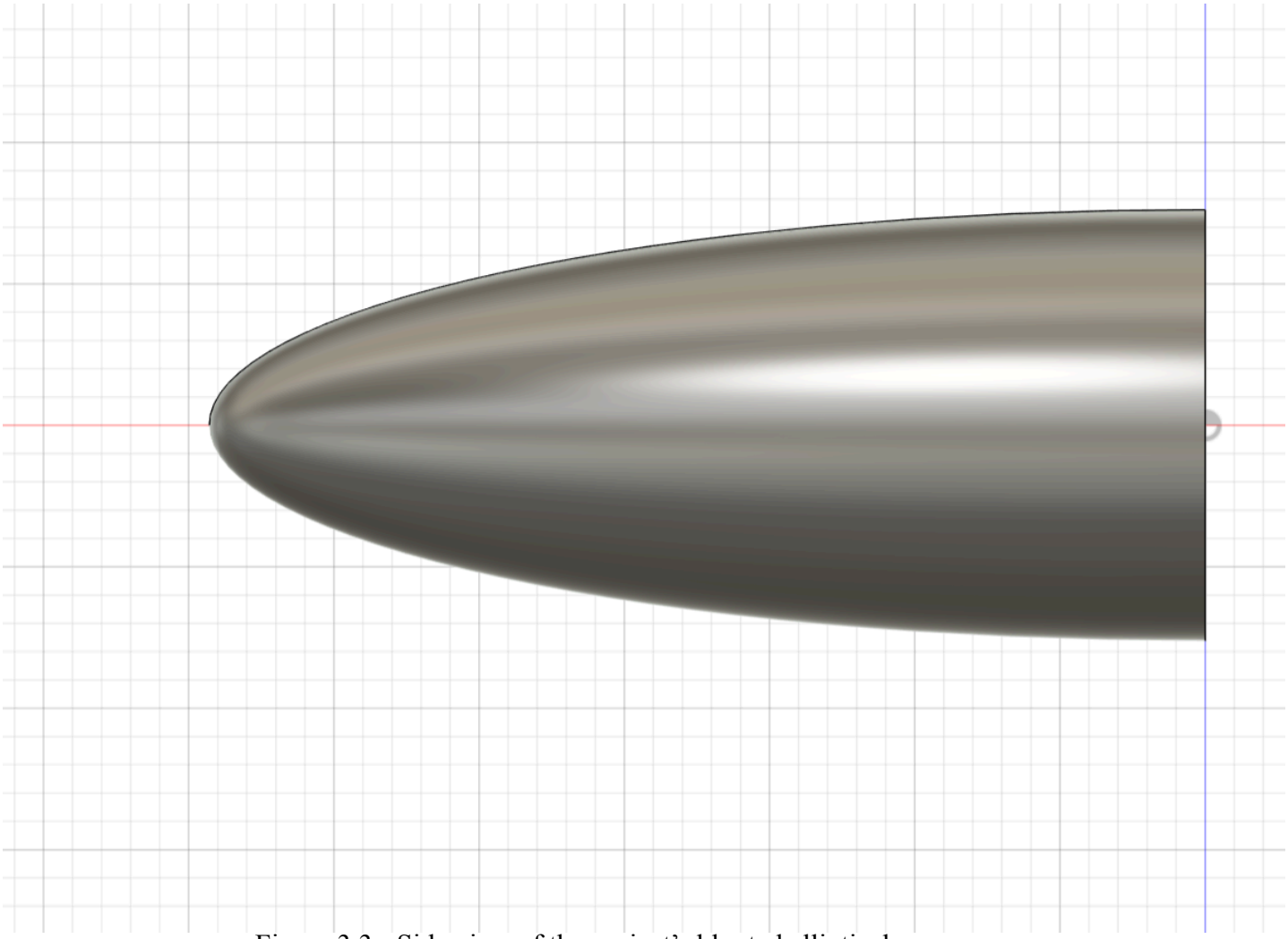

Figure 3.3 - Side view of the project's blunted elliptical nose cone

One of the most significant advantages of this design, from a manufacturing point of view, is its compatibility with 3D printing. The smooth and gradual transitions of the elliptical profile are ideal for additive manufacturing, where complex curves and contours can be reproduced with high precision. This allows for quick and cost-effective prototyping that matches the project's funding capabilities, enabling multiple variations of the design to be produced and tested in a short timeframe. Additionally, the reduced geometric complexity compared to other advanced nose cone designs makes it less prone to issues like uneven surface finishes or dimensional inaccuracies, which are critical for maintaining aerodynamic performance during testing.

Testing the blunted elliptical nose cone is also straightforward. Its symmetrical and balanced profile ensures consistent results in aerodynamic evaluations in the next step in this project, which is CFD simulations. The design's simplicity also supports modifications and adjustments

based on initial test outcomes, making it easier to optimize for the specific project requirements. The performance of the nose cone may be improved using this iterative method without causing major delays or expenses.

3.2.2 Power-Law/Von Karman Nose Cone

3.2.2.1 Power-Law/Von Karman Nose Cone Discussion

The Power-Law or Von Kármán nose cone is a highly engineered design and optimized to be used in supersonic and hypersonic rockets due to its exceptional aerodynamic and thermal performance. Derived from potential flow theory, the design's profile is mathematically engineered to produce minimal wave drag by creating minimal pressure gradients and weak oblique shockwaves. The Von Kármán nose cone is derived from the equation of a body of revolution that produces minimal drag in supersonic flow. Its profile is defined using the equation:

$$x = R\sqrt{\frac{\theta - sin\theta}{\pi}} \tag{10}$$

Where x is Axial distance from the base of the nose cone, R is radius of the nose cone at the base, and θ is half-angle of the nose cone, which varies along the length.This shape ensures a gradual taper from the base to the tip, reducing pressure gradients and minimizing shockwaves at supersonic speeds, which matches exactly the project's objectives.

The power-law nose cone is a generalization of the Von Kármán shape and can be expressed as:

$$r(x) = R(1 - \frac{x}{L})^n \tag{11}$$

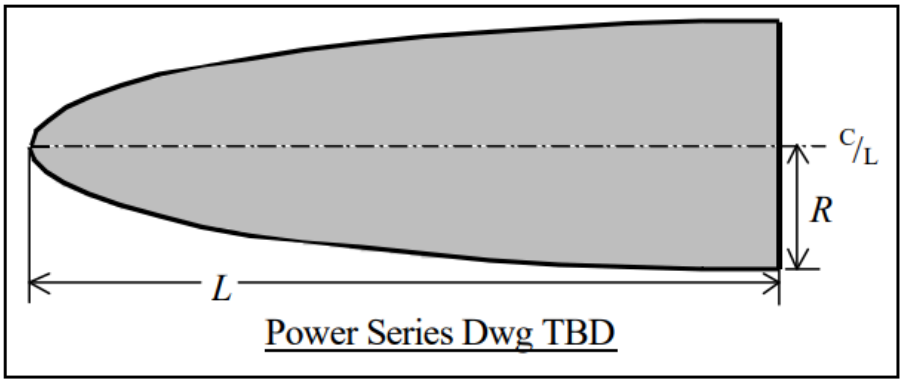

Figure 3.4 - Power series nose cone [46]

Where r(x) represents the radius at a specific point along the axial distance, defining the shape's curvature. The parameter R is the base radius of the nose cone, marking its widest point,

while L is the total length of the nose cone from the base to the tip. The power-law exponent n plays a massive role in determining the geometry, as it controls the degree of bluntness or sharpness of the profile. For missiles that fly supersonic, values of n typically range between 1.5 and 3, striking an optimal balance between minimizing drag and managing thermal resistance, making it suitable for high-speed aerodynamic performance. Since the project is seeking a blunt nose cone design, different values of n will be tested.

Advantages of Power-Law/Von Karman Nose Cones: The Power-Law/Von Kármán nose cone provides many significant advantages when considered for optimizing a blunt nose design for missiles with supersonic missions, making it a promising choice for this project. One of the primary advantages is its ability to drastically minimize wave drag, which is the dominant source of resistance at supersonic speeds and a main concern for this project. The smooth curvature of the Von Kármán profile generates weak oblique shockwaves instead of intense bow shocks, ensuring more efficient stored energy dissipation and streamlined flow around the missile body, and most importantly, an attached flow around control surfaces. This reduces overall drag while maintaining active controls and stability, crucial for precision in high-speed flight and mission execution.

The gradual taper of the nose cone delays boundary layer separation, ensuring a laminar flow around the body and enhancing the missile's range and maneuverability. The shape also excels in thermal management by redistributing stagnation heating over a broader surface area, lowering peak temperatures at the nose cone tip and reducing the risk of thermal damages. This feature is particularly advantageous for supersonic and possibly hypersonic applications, where aerodynamic heating can compromise structural integrity.

The design's mathematical precision enables fine-tuning of bluntness through the power-law exponent n, allowing engineers to optimize the balance between drag reduction and thermal resilience based on mission requirements. Overall, the Power-Law/Von Kármán nose cone is a highly efficient and versatile design for supersonic flight nose cone optimization, as it offers a reasonable balance between all variables of concern.

Disadvantages of Power-Law/Von Karman Nose Cones: While the Power-Law/Von Kármán nose cone offers many aerodynamic and thermal advantages for supersonic flight, it also presents several challenges and limitations when considered for optimizing blunt nose designs. One primary disadvantage is its reduced performance in thermal management compared to fully blunt designs. Although the Von Kármán shape redistributes stagnation heating more effectively than sharp or conical nose cones, it still concentrates heat more intensely at the tip than a blunted elliptical or spherical design due to a higher surface area. This concentration can lead to higher thermal stresses, requiring more advanced materials, additional thermal protection systems and thermal analysis, which will increase the missile's weight and complexity.

Another huge limitation is complex manufacturing. The precise and detailed mathematical profile of the Power-Law/Von Kármán nose cone requires advanced fabrication techniques, such as CNC machining or additive manufacturing, to achieve the required tolerances and design properties. This complexity can lead to higher production costs and increased fabrication time, which may be a concern for mass production in military applications.

In the context of seeker integration, the shape's gradual taper can introduce challenges for infrared systems. Although it reduces severe aero-optical distortions compared to fully blunt geometries, the remaining density gradients and flow disturbances around the seeker dome may still affect targeting precision, specifically at high angles of attack or during rapid maneuvers. This could require additional design optimization for the seeker system to compensate for residual distortions.

Finally, the Power-Law/Von Kármán nose cone may not align fully with different mission-segment requirements. Its performance is optimized for supersonic speeds, but for missions involving prolonged subsonic or transonic phases, alternative designs such as elliptical or ogive nose cones may offer better overall efficiency in all mission segments. Similarly, the Von Kármán shape's reliance on precise aerodynamic flow conditions means it may be less adaptable to unpredictable or rapidly changing operational environments. While this design choice is effective in many scenarios, the previously mentioned limitations highlight the need for careful evaluation and integration when considering the Power-Law/Von Kármán nose cone for optimizing blunt nose designs in supersonic missiles.

3.2.2.2 Power-Law/Von Karman Nose Cone Choice Design

The Power-Law/Von Kármán Nose Cone was considered for this project due to its exceptional aerodynamic properties and ability to minimize wave drag in supersonic flight despite its disadvantages, making it an ideal candidate for missile applications like the missile of interest for this project. This nose cone shape is mathematically derived to produce smooth pressure gradients along its surface, generating weaker oblique shockwaves and significantly reducing drag compared to other blunt or less streamlined designs. The Power-Law profile for this project with respect to the sized geometry is defined by the equation

$$r(x) = 1.5\left(1 - \frac{x}{6.75}\right)^{n} \quad (12)$$

The Power-Law profile allows for precise control of the nose cone's shape through the exponent n, which determines the degree of bluntness or sharpness of the profile. For this project, n-values ranging from 1.5 to 3 will be tested during CFD validation, as these values define the range where the tip is considered sufficiently blunt, note that the CAD Provided in the report is a nose cone with a costume power of n=0.75 that is subjected to change and this value will not be tested. This flexibility enables the design to be customized to meet specific project objectives, allowing for an exploration of how varying n-values impact key performance metrics such as drag reduction, thermal management, and seeker system compatibility. By testing this range, the project aims to identify the optimal nnn-value that balances these competing factors, ensuring the nose cone design is both aerodynamically efficient and thermally resilient while maintaining compatibility with the missile's seeker system.

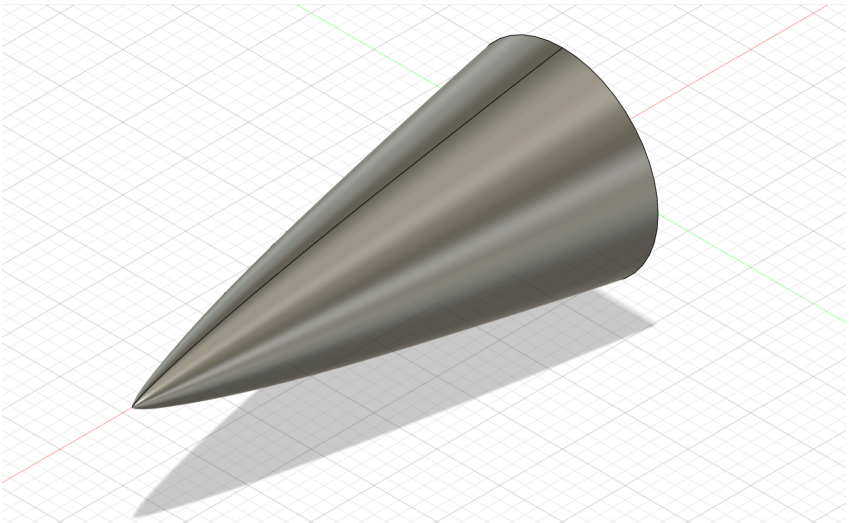

Figure 3.5 - Isometric view of the project's costume Power-Law Nose Cone (n=0.75)

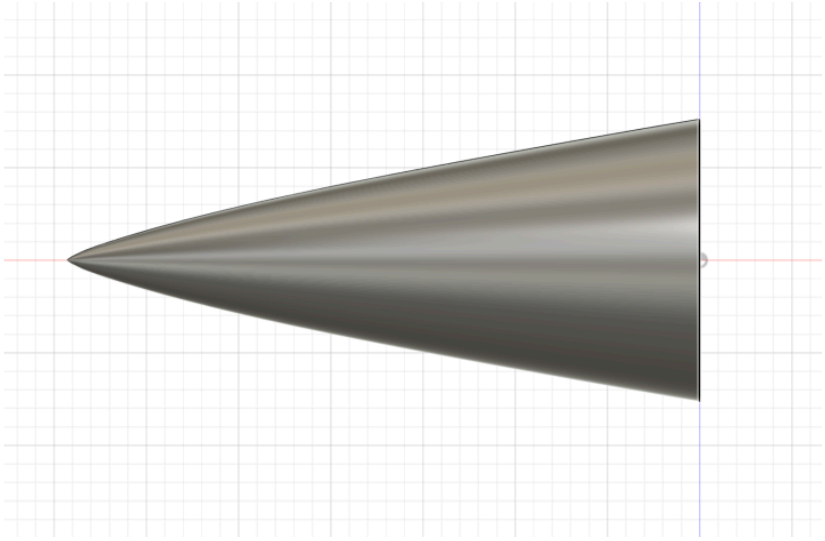

Figure 3.6 - Side view of the project's costume Power-Law nose cone (n=0.75)

One of the main reasons for fully considering the Power-Law/Von Kármán Nose Cone is its ability to enhance the missile's speed and range by minimizing aerodynamic resistance and its very flexible design dimensions. The shape promotes smooth airflow transitions, reducing boundary layer separation and pressure drag, which are critical for ensuring stable and efficient supersonic performance. Furthermore, its gradual curvature helps distribute aerodynamic forces evenly, reducing stress concentrations that could compromise the structural integrity of the nose cone. This feature is particularly advantageous for high-speed missiles, where maintaining structural durability under extreme conditions is a primary concern. The geometry also complements the integration of seeker systems by minimizing aero-optical distortions caused by density gradients and temperature variations in the shock layer, ensuring accurate infrared targeting and signal clarity.

3.2.3 Spherically Blunted Conic Nose Cone

3.2.3.1 Spherically Blunted Conic Nose Cone Discussion

The spherically blunted conic nose cone is a hybrid design that mixes the geometry of a spherical tip with a conical aft section, which offers a decent compromise between aerodynamic performance and thermal management. This design in particular is well-suited for high-speed applications, such as the missile of interest in this project, where drag reduction, stability, and thermal resilience are crucial.

The spherical tip shapes the frontal portion of the nose cone and is characterized by its radius of curvature noted as Rs, which defines the degree of bluntness. This rounded section of the nose cone purpose is diffusing stagnation point heating, reducing the intensity of thermal stresses concentrated at the tip during the supersonic flight. Following the spherical section, the aft portion transitions into a conical shape smoothly, tapering toward the missile's body for maximum aerodynamic efficiency. This conical section is defined by its semi-vertex angle noted θ, which determines the steepness of the taper. The choice of θ directly affects the aerodynamic performance, influencing both drag reduction and flow characteristics around the canards which affects the stability. The smooth transition and blending of these two regions can customize a balance between thermal resilience at the nose and aerodynamic efficiency along the aft body, making the spherically blunted conic nose cone a practical and effective design for supersonic missile applications.

As mentioned previously, the spherical tip is defined by its radius of curvature Rs, provides a rounded surface to diffuse stagnation point heating and reduce concentrated thermal stresses experienced at the nose during high-speed flight. Mathematically, this spherical region satisfies the equation

$$x^2 + y^2 = R_s^2 \tag{13}$$

where x and y represent the axial and radial distances, respectively, within the spherical section. The spherical portion transitions seamlessly into a conical section, described mathematically by

$$y(x) = tan(\theta)\,(x - xs) \tag{14}$$

where θ is the semi-vertex angle governing the steepness of the conical taper. The degree of bluntness for this hybrid design is quantified using the bluntness ratio

$$R_s/L \tag{15}$$

where L is the total length of the nose cone. Larger ratios enhance thermal resistance but increase drag, while smaller ratios prioritize aerodynamic efficiency. The seamless integration of the spherical and conical sections ensures smooth flow transitions, making the spherically

blunted conic nose cone an effective design for supersonic missiles, where thermal resilience and aerodynamic performance are critical.

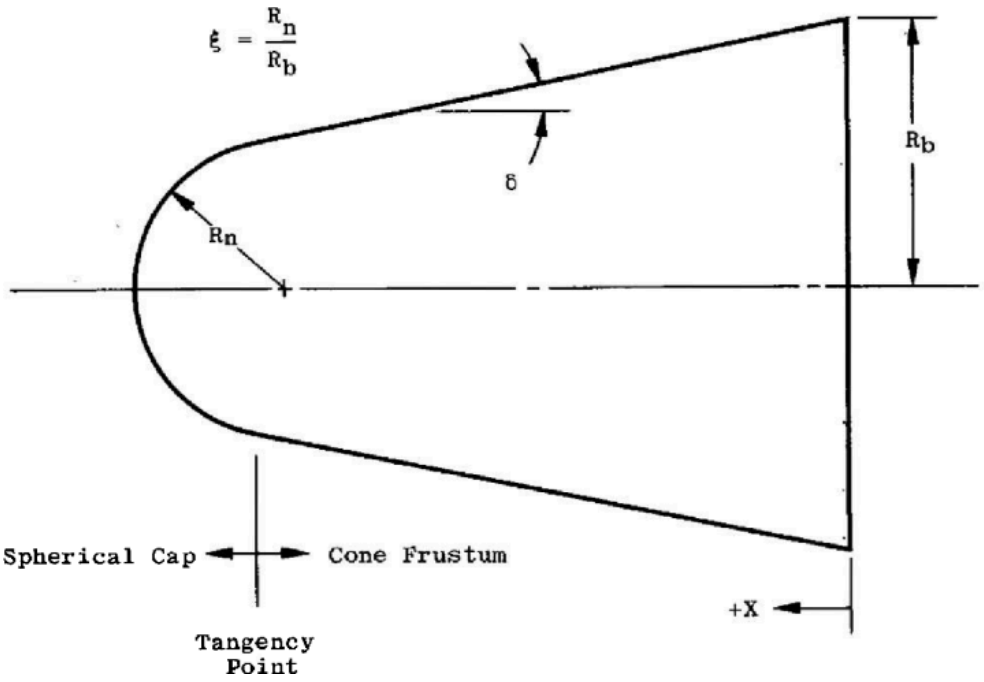

Figure 3.7 - Spherically blunted conic nose cone [47]

Advantages of Spherically Blunted Conic Nose Cones: Spherically blunted conic nose cones offer several advantages, making them a versatile choice for supersonic missile applications. The spherical tip effectively manages thermal loads by diffusing stagnation heating across a broader surface area, reducing the intensity of thermal stresses concentrated at the nose. This is particularly advantageous for high-speed missiles, where aerodynamic heating can compromise structural integrity. The conical aft section complements the design by reducing wave drag compared to fully blunt geometries, ensuring smoother airflow and enhancing overall aerodynamic efficiency. Additionally, the gradual transition between the spherical and conical sections promotes laminar flow, delaying boundary layer separation and improving stability during supersonic flight. This smooth integration also minimizes shockwave interference, which can disrupt flow and increase drag. Structurally, the hybrid geometry distributes aerodynamic forces evenly, avoiding stress concentrations that could lead to material fatigue or failure. These advantages make spherically blunted conic nose cones an effective solution for balancing thermal protection, drag reduction, and aerodynamic stability in modern missile systems.

Disadvantages of Spherically Blunted Conic Nose Cones: Weight considerations are a significant factor, as the spherical tip typically requires a larger volume of material to maintain structural integrity and withstand aerodynamic and thermal stresses. This additional material can increase the overall weight of the missile, potentially affecting its maneuverability and fuel efficiency. Complex flow interactions around the spherical tip can also lead to unsteady

aerodynamic phenomena, such as flow oscillations or transient separations at high angles of attack, which may compromise the missile's stability during maneuvers.

Furthermore, the drag penalties associated with the spherical tip's broader frontal area become more pronounced as Mach numbers increase, making this design less suitable for applications requiring extreme speeds or long ranges. Shockwave interference between the bow shock and downstream surfaces of the missile can exacerbate pressure drag and induce localized heating further aft on the missile body, creating additional design challenges. Additionally, the blunted nature of the tip can reduce the missile's overall aerodynamic efficiency during subsonic or transonic flight phases, making it less versatile across varying flight regimes.

Lastly, the visual and thermal signature of a spherically blunted conic nose cone is generally higher than that of sharper profiles, as the broader tip creates a larger heat plume due to stagnation heating. This increased signature can make the missile more detectable by advanced tracking and targeting systems, reducing its stealth capabilities in modern combat scenarios. These additional disadvantages underscore the need to carefully evaluate mission-specific requirements when selecting a nose cone design for supersonic missiles.

3.2.3.2 Spherically Blunted Conic Nose Cone Design

The primary reasons for considering the Spherically Blunted Conic Nose Cone for this project is its simplicity in design, flexibility, and its adaptability to project's mission requirements. Its geometry that is characterized by a spherical radius at the tip transitioning into a conical taper allows for predictable aerodynamic performance and straightforward integration with the missile body, while having the ability to test various refined dimensions to obtain the most optimal. This design in general ensures that aerodynamic forces are distributed evenly, reducing the likelihood of stress concentrations that can lead to material fatigue. Furthermore, the design complements infrared seeker systems by reducing density and temperature gradients in the shock layer, which can interfere with signal clarity.

Another main reason for this design to be considered is its practicality in manufacturing and testing. The relatively straightforward geometry makes it easier to model in CAD and manufactured using 3D printing, which is the chosen method to build the nose cone for the proof of concept part of this project. This adaptability allows rapid prototyping and testing, allowing efficient evaluation and optimization of the design through CFD simulations and cheaper/faster manufacturing. The ability to refine the nose cone based on test results will ensure that the final design meets the project's specific aerodynamic and thermal performance criteria.

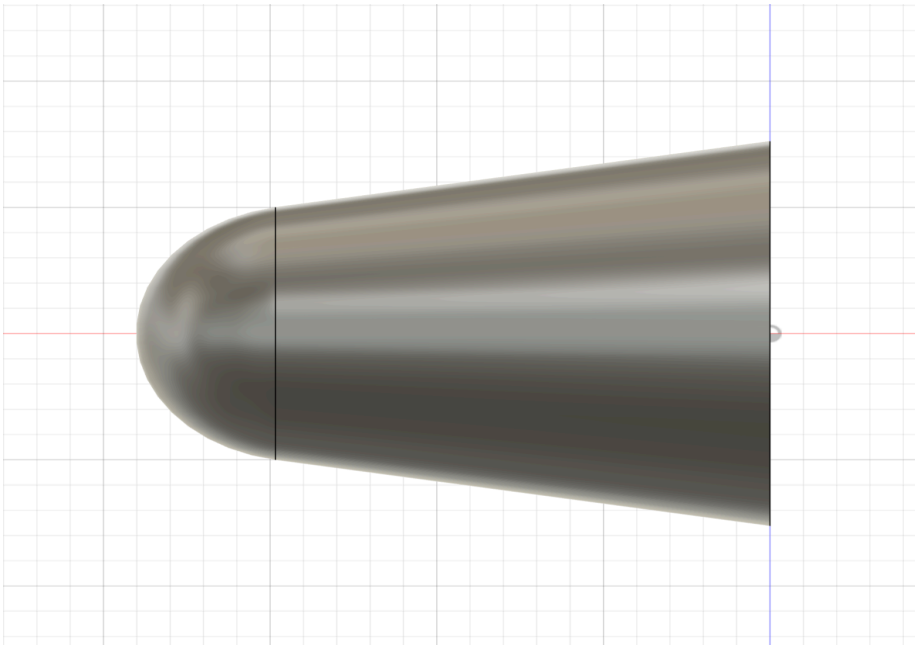

Figure 3.8 - Side view of a potential spherically blunted conic nose cone design

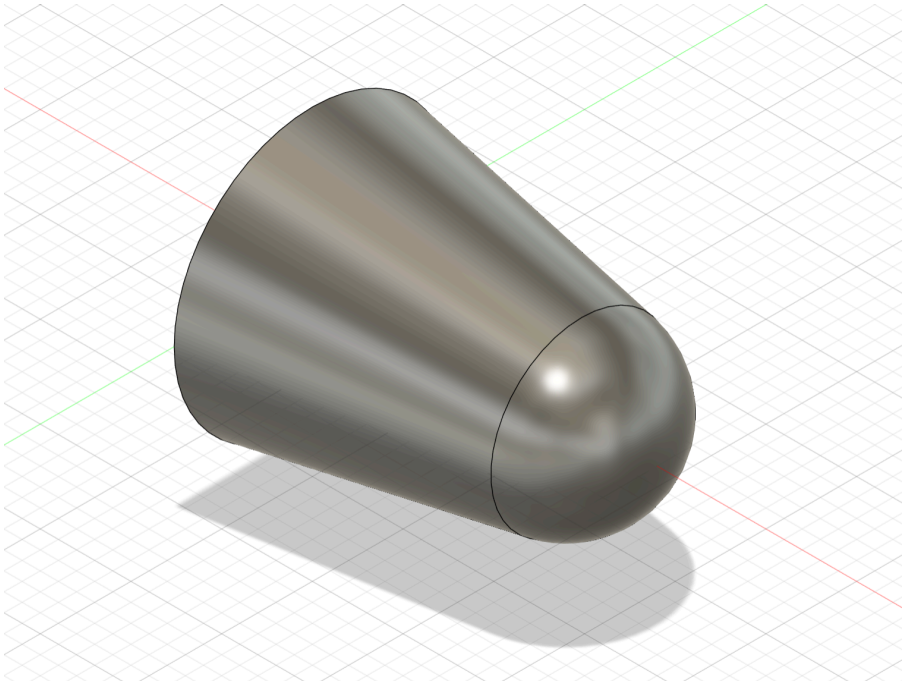

Figure 3.9 - Isometric View of a Potential Spherically Blunted Conic Nose Cone Design

3.3 Optimal Design Decision

From the previously identified nose cone options, three designs (Blunted Elliptical, Power-Law/Von Kármán, and Spherically Blunted Conic) were selected due to their suitability in meeting the project's objectives. These designs were chosen among many alternatives as they align with the specific requirements of this project, including compatibility with supersonic flight speeds and the need for a blunt shape to address aerodynamic and thermal challenges. To prioritize essential design considerations and project objectives, a decision matrix was developed, focusing on the critical needs and challenges of the project, primarily the minimization of flow turbulence and shockwave formation around the canards and control surfaces.

The decision matrix evaluates the selected nose cone designs across eight key criteria, with each design scored on a scale of 1 to 5:

1: Poor performance in that criterion.

5: Excellent performance in that criterion.

This scoring system provides an objective framework to assess how well each nose cone design aligns with the project's primary goals of reducing shockwave interference, maintaining laminar flow, and optimizing aerodynamic performance around the canards and control surfaces.

The Evaluation Criteria is the following:

1. **Minimizing Flow Turbulence Around the Body**: Assesses the nose cone's ability to promote smooth airflow along the missile's body and minimize turbulence near the canards.
2. **Minimize Shockwave Formation:** Evaluates the nose cone's effectiveness in generating weaker oblique shocks instead of strong bow shocks.
3. **Drag Reduction:** Measures the nose cone's capability to reduce aerodynamic resistance.
4. **Thermal Management:** Reflects the design's ability to manage and distribute stagnation heating effectively.
5. **Structural Robustness:** Considers the nose cone's resistance to stress and fatigue under aerodynamic and thermal loads.
6. **Seeker Compatibility:** Examines how well the nose cone integrates with the infrared seeker system, minimizing aero-optical distortions.
7. **Ease of Manufacturing:** Reflects the complexity of 3D printing and time of printing the nose cone design.
8. **Adaptability for Testing:** Assesses how feasible for the nose cone can be prototyped and tested for performance validation.

The resulting decision matrix summarizes the general characteristics and performance of each nose cone design relative to these criteria. While these scores provide an initial assessment, the report will further analyze the designs using thermal analysis and finite element analysis (FEA) once CFD simulations are completed. These simulations will provide critical data on specific

pressure forces and thermal loads that the nose cone designs will experience, enabling a more detailed evaluation in subsequent sections of this report.

Table 3.1 – Decision matrix for nose cone design choices

Criteria	Blunted Elliptical	Power-Law/Von Kármán	Spherically Blunted Conic
Minimizing Flow Turbulence Around Body	5	4	4
Minimize Shockwave Formation	5	4	4
Drag Reduction	4	5	3
Thermal Management	5	3	5
Structural Robustness	4	5	5
Seeker Compatibility	5	5	4
Ease of Manufacturing	4	3	4
Adaptability for Testing	5	4	4
Total Score	**37**	**33**	**33**

The decision matrix provides useful insights into the performance of each nose cone design relative to the project's objectives. The Blunted Elliptical Nose Cone emerges as a strong candidate for reducing turbulence and shockwave formation, matching well with the project's primary focus of minimizing aerodynamic interference around the canards. Its effectiveness in maintaining stability makes it particularly valuable for high-precision missions, although it is slightly less effective in drag reduction and structural robustness compared to other designs. The Power-Law/Von Kármán Nose Cone stands out for its exceptional drag reduction and structural performance, making it ideal for optimizing speed and range. However, its sharper profile raises concerns about thermal management and manufacturing complexity, which may require additional resources for implementation. Lastly, the Spherically Blunted Conic Nose Cone excels in thermal management and structural durability, making it highly suitable for scenarios where thermal resilience and robustness are priorities. However, it falls behind in aerodynamic efficiency and drag reduction, limiting its effectiveness for speed-focused missions. Overall, the matrix highlights how each design balances trade-offs, with the Blunted Elliptical Nose Cone being particularly well-suited for the project's goal of mitigating shockwave interference while ensuring stable aerodynamic performance.

4. Sidewinder Missile Stability and Controls

4.1 AIM-9 Sidewinder Missile Stability Analysis

Since the AIM-9 Sidewinder is a simply designed short-range air-to-air missile, it is widely used for its effectiveness and durability in military operations. Due to the classified nature of its detailed design parameters, the discussion of the Sidewinder's stability without active controls is general and limited in scope. Nonetheless, its aerodynamic and stabilization features can be examined to understand its inherent stability mechanisms.

As previously outlined in the components section in this project, the Sidewinder utilizes a cruciform wing and tail fin configuration to ensure general aerodynamic stability. This design activates passive self-correction during unguided flight phases, where deviations from the desired trajectory are naturally countered by restoring aerodynamic forces. Such passive stabilization is vital for maintaining a predictable and steady flight path before and during fast response and guided operation.

In addition to its aerodynamically stable geometry, the missile integrates rollerons, which is a system of small, freely spinning wheels located at the trailing edges of its tail fins. Discussed in detail in Section 2.2, these rollerons serve as gyroscopic stabilizers, counteracting roll disturbances encountered during flight. As the missile accelerates, aerodynamic forces induce rotation of the rollerons, which generate gyroscopic moments to resist unwanted roll motions. This passive roll stabilization mechanism not only enhances the missile's overall stability but also reduces full reliance on active control systems, thereby lightening the computational and operational burden on its onboard guidance systems.

The missile's compact dimensions of approximately 2.87 meters in length and 0.127 meters in diameter does contribute to its overall aerodynamic efficiency. Its stability margin, typically measured in calibers, is estimated to be between 1 and 1.5 calibers. This balance ensures the missile remains aerodynamically stable while retaining sufficient maneuverability to engage dynamic targets. For instance, a stability margin of 1.5 calibers for a missile diameter of 0.127 meters positions the center of pressure approximately 0.19 meters aft of the center of gravity, providing robust stability during both subsonic and supersonic flight regimes.

The AIM-9's enduring legacy lies in its adaptability, ease of use, and versatility in engaging highly maneuverable aerial targets with a high level of stability. Since its introduction in the 1950s, the missile has undergone continuous evolution to remain operationally relevant. Its interesting features, including rollerons and aerodynamic design, make it an exemplary case study in missile technology and a primary focus for this project. The Sidewinder provides valuable insights into key principles of aerodynamic optimization, computational modeling, passive stabilization mechanisms, and semi-basic systems and manufacturing processes, serving as a foundation for modern research and development in missile technology.

4.2 Scaled Missile Stability Analysis

As discussed in Section 2, the scaled geometry of the AIM-9 Sidewinder missile was designed to have a total length of 72.59 inches and an outer diameter of 3.5 inches. However, the final selection of the motor directly influences the diameter of the scaled geometry due to variations in motor availability. Since the inventory of Level 3 certified motors fluctuates based on stock levels and manufacturer supply, adjustments to the missile's diameter may be necessary to accommodate the available propulsion system. For an L3 certification-class launch, the project requires an M-class motor, which typically falls within an outer diameter range of 3 inches to 4 inches and a length between 24 inches to 40 inches. The objective of this project is to maintain a motor diameter as close to 3 inches as possible to preserve the initially scaled proportions of the missile, ensuring that only minimal modifications are required in the sizing and scaling of the missile's structural and aerodynamic features. However, after evaluating available motor options, a 3-inch diameter motor with a length of 24 inches was selected. This motor selection led to a slight increase in the overall missile diameter, adjusting from 3 inches to 3.5 inches, while still maintaining the integrity of the original scaled design.

To conduct a comprehensive stability assessment, the project utilized OpenRocket, an industry-standard rocketry simulation software. OpenRocket provided detailed insights into the rocket's static and dynamic stability by analyzing various design parameters, including center of pressure, center of gravity, and stability margin. The stacked rocket stability analysis, as shown in Figure 4.1, presents the stability characteristics based on multiple input parameters and design choices. These inputs were carefully selected to closely replicate the aerodynamic and structural properties of the AIM-9 Sidewinder missile, while also following safety regulations and L3 certification requirements for a civilian launch. The OpenRocket model was meticulously refined under the supervision of a rocketry advisor at San José State University, where several iterative modifications were made to enhance the aerodynamic performance and structural integrity of the design. These modifications included slight adjustments to the missile's outer diameter to accommodate the selected propulsion system, as well as minor reductions in fin size to comply with safety and liability constraints for L3 rocketry certification.

The selection of materials for the rocket was based on cost-effectiveness, availability, and manufacturability. Each material choice was carefully evaluated to ensure structural durability while maintaining feasibility for fabrication. The material selection process also considered factors such as weight optimization for CG placement, mechanical properties, and ease of manufacturing, ensuring that the final design remains aerodynamically efficient and structurally robust. The rationale behind each material selection, along with its mechanical properties and performance under launch conditions, will be discussed in Section 5.

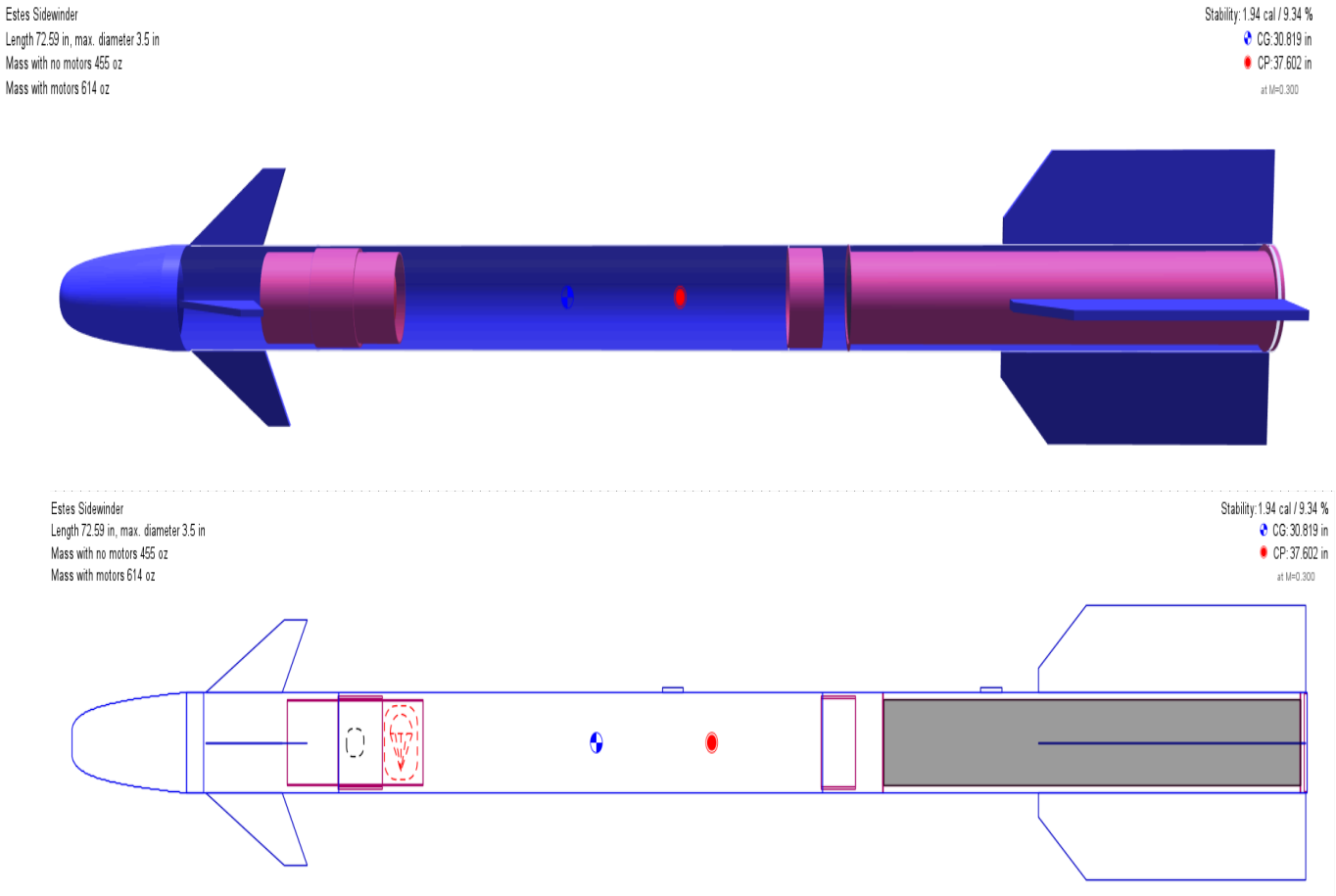

Figure 4.1 - 3D and Side View of Missile components in OpenRocket

The final design for the scaled geometry of the missile exhibits a stability margin of 1.94 calibers, corresponding to 9.34% of the total missile length. This value is very close to the recommended 2-caliber stability margin, which is widely advised in advanced rocketry and large-scale aerospace vehicle design. A stability margin approaching 2 calibers ensures that the rocket maintains natural aerodynamic stability, which is particularly critical for high-performance launch vehicles. This characteristic is essential, especially in configurations where a significant portion of the mass is concentrated toward the aft section, such as in this design where the aft-mounted wings extend 15.3 inches along the missile's total length.

One of the key design challenges in this project was optimizing the size of the canards (forward control fins) to comply with Level 3 high-power rocketry safety regulations while also ensuring that the pressure measurements collected from the canards remain valid. The canards are designed to house pressure sensors all across, which are critical for this project to validate the

aerodynamic performance and stability predictions of the system. However, modifications to canard sizing directly impact the center of pressure location, requiring extensive iterative testing and recalibration to maintain a desirable stability margin. Increasing the fin size results in a forward shift of the CP, which is generally undesirable as it reduces static stability. Conversely, reducing the fin size shifts the CP rearward, which is more desirable for passive stability but may compromise the intended functionality of the canards. Striking a balance between CP positioning and the stability margin was a crucial aspect of the design process.

Additionally, the center of gravity is subject to variation due to the dependence on motor selection and availability. The CG is expected to shift aft or forward within a tolerance of ±0.5 calibers, depending on the final propulsion system selection. For the current simulation and stability analysis, the motor selected was the Cesaroni Technology Inc. 5604M1830-P, which was used as a reference configuration. However, since the availability of certified M-class motors fluctuates, future design adjustments may be required to accommodate alternative propulsion options while ensuring that the stability remains within an acceptable range.

The design approach for stability tuning and aerodynamic optimization ensures that the missile-scaled rocket meets both aerodynamic efficiency and safety constraints, while also aligning with the core objectives of the project. The selection of materials for each component of the scaled missile will be thoroughly discussed in Section 5, where a comprehensive analysis will be provided on the manufacturing plan, material properties, and geometric specifications from the nose cone to the aft wings. Additionally, flight performance predictions and design alternatives will be examined, with a strong correlation to stability and control considerations discussed in Section 4. Since Section 4 focuses on achieving the desired stability margins and aerodynamic balance, Section 5 will detail the engineering decisions and material choices that enabled those stability goals to be realized, ensuring a seamless integration between theoretical design, practical implementation, and performance evaluation.

5. Material Selection and Flight Performance Parameters

5.1 Final Material Selection

Material selection plays a crucial role in determining the center of pressure and center of gravity relationship, which directly affects the stability, flight performance, and accuracy of aerodynamic data collection. Every component in this project serves a specific function and must be made from materials that balance strength, weight, heat resistance, and manufacturability. The material selection process for this final design was highly strategic and iterative, ensuring that each component contributes to the overall aerodynamic stability and structural integrity of the missile to serve and fulfill the purpose of the project.

The nose cone serves as a critical aerodynamic component in this project, as it directly influences shockwave behavior, aerodynamic stability, and sensor integration. Given its importance, the material selection process prioritized ease of manufacturing, adaptability, and structural performance to ensure both aerodynamic efficiency and functionality. Since the nose cone not only dictates the formation and propagation of the bow shockwave but also houses pressure sensors for data collection, it required a structurally robust yet lightweight material that could withstand high-speed aerodynamic loads while maintaining precise sensor placement. After evaluating multiple material options, 3D-printed carbon fiber-infused PETG was selected as the optimal choice due to its superior mechanical properties, ease of fabrication, and compatibility with high-power rocketry applications. Carbon fiber-infused PETG offers enhanced mechanical strength compared to standard PETG or PLA, making it ideal for structural components exposed to significant aerodynamic forces and free stream. Its high rigidity ensures that the nose cone maintains its shape and structural integrity during high-speed flight and shockwave interactions, reducing the likelihood of deformation under load. During launch and flight, the nose cone is subjected to intense vibrations, aerodynamic heating, and impact forces, especially during parachute deployment and landing. Unlike traditional 3D printing materials such as PLA or ABS, carbon fiber-infused PETG exhibits superior impact resistance, making it less prone to cracking or structural failure under stress.

In terms of thermal performance, carbon fiber-infused PETG provides higher heat resistance than standard PETG, making it better suited for supersonic and high-speed subsonic applications such as this project, where aerodynamic heating and temperature fluctuations are a concern. While it does not offer the extreme heat resistance of aerospace-grade materials such as PEEK or Ultem, it is sufficient for Level 3 high-power rocketry applications, particularly when combined with an external heat-resistant coating or protective surface finish. Another advantage of carbon fiber-infused PETG over conventional 3D printing materials is its smooth surface finish, which minimizes surface roughness and aerodynamic drag, improving overall flight efficiency. Additionally, PETE's low moisture absorption prevents warping or degradation over time, ensuring long-term dimensional stability, even in high-humidity environments.

A key design consideration for the nose cone in this project was its role as a housing unit for embedded pressure sensors, which will measure shockwave interactions and aerodynamic forces in real-time. Carbon fiber-infused PETG is easily machinable and modifiable, allowing for precise sensor placement and wiring integration without compromising structural strength. The

material also supports the addition of threaded inserts or reinforcement layers, further enhancing its adaptability and durability. By combining mechanical strength, thermal resistance, ease of fabrication, and sensor integration capabilities, the use of carbon fiber-infused PETG ensures that the nose cone meets the structural, aerodynamic, and data acquisition requirements of the project, making it an ideal choice for high-power rocketry applications.

The canards are one of the most critical components of this project, second only to the nose cone, as they play a fundamental role in shockwave interaction and stability behaviour. The project's primary objective is to minimize the effect of bow shock wave interference on the canards to improve active control efficiency. Therefore, the material selection process had to consider aerodynamic performance, structural integrity, sensor integration, and stability effects. Since the canards will house pressure sensors to collect aerodynamic data, the material had to allow for precise sensor installation while maintaining durability under flight conditions. Furthermore, to meet the stability requirements, it was essential to shift the center of gravity forward relative to the center of pressure to achieve the desired stability margin of at least 2 calibers.

Originally, the canards were designed using carbon fiber-infused PETG, but after further stability considerations, the final material selection was changed to titanium or aluminum. This transition presents multiple aerodynamic, structural, and fabrication advantages, particularly in terms of CG adjustment, strength, and sensor integration. One of the primary motivations for switching to a metallic material was to increase the forward mass of the missile, thereby shifting the CG forward without needing additional counterweights or mass redistribution. Given that the canards were slightly downsized to comply with safety regulations for Level 3 civilian rocketry flight testing, the added mass from a denser material such as titanium or aluminum helps counteract this change and maintain the intended stability margin.

Beyond stability adjustments, metallic canards offer significantly higher rigidity compared to 3D-printed alternatives, ensuring that the surfaces do not flex or deform under aerodynamic loading. This is particularly important for this design, as the canards are inactive control surfaces and are fully exposed to freestream flow and potential shockwave interactions. Unlike carbon fiber-infused PETG, which may experience fatigue and deflection over time, titanium and aluminum provide exceptional structural resilience, allowing the canards to withstand high dynamic pressure and maintain their aerodynamic effectiveness throughout the flight.

Another key advantage of switching to metallic canards is the ability to directly weld pressure sensors onto their surface, eliminating the need for separate 3D-printed sensor housings. In the original design, carbon fiber-infused PETG required additional enclosures and mounting mechanisms for the pressure sensors, which increased manufacturing complexity and introduced potential structural weak points. By utilizing titanium or aluminum, the sensors can be precision-machined or welded directly onto the canard surface, ensuring more secure integration, reduced failure risk, and possibly improved sensor accuracy by making them more exposed to stream. This simplifies the sensor installation process and enhances the reliability of aerodynamic pressure measurements, which are essential for validating the project's core hypothesis regarding shockwave interactions on control surfaces.

The avionics bay will be 3D printed and reinforced with carbon fiber for the sake of combining lightweight precision manufacturing with high structural strength. Carbon fiber reinforcement significantly improves impact resistance, thermal stability, and vibration damping, ensuring the protection of critical electronics such as the GPS module, power systems, and pressure sensors from mechanical stress during launch and flight. Unlike PLA, which is prone to warping and cracking, carbon fiber provides superior rigidity and RF transparency, ensuring uninterrupted GPS and telemetry signal transmission. The reinforced design prevents electronic displacement, maintains stable power delivery, and optimizes strength without excessive weight, making it an ideal choice for L3 high-power rocketry applications.

The main body tubes will be constructed from fiberglass, selected for its high strength-to-weight ratio, durability, and RF transparency, ensuring uninterrupted GPS signal transmission for accurate tracking and telemetry. The three-stage configuration, instead of a single continuous tube, allows for optimized material distribution, enabling varying thicknesses across different sections to enhance structural integrity and stability. The aft section, which houses the motor and motor retainer, will have reinforced fiberglass layers to withstand high thrust loads and aerodynamic forces, ensuring durability under extreme conditions. Meanwhile, the forward section will be reasonably thickened to shift the center of gravity forward, improving stability and flight control. The sections will be securely connected using fiberglass couplers, ensuring precise alignment, structural continuity, and even load distribution. This modular design enhances manufacturing flexibility, simplifies maintenance and part replacement, and allows for future design modifications, making it an efficient and adaptable solution for executing this project.

The motor retainer, responsible for securely holding the rocket motor in place, is centered by two fiberglass centering rings, ensuring precise alignment and stability within the airframe. The retainer itself is constructed from fiberglass and reinforced with epoxy, chosen for its high structural integrity, thermal resistance, and reusability. Fiberglass provides an excellent strength-to-weight ratio, maintaining rigidity and durability while keeping the rocket lightweight and aerodynamically efficient. Its high resistance to heat and combustion makes it ideal for enduring intense motor exhaust gases and extreme temperatures without compromising structural integrity. Given that the project involves multiple flight tests, the retainer's durability and long-term reusability are crucial to preventing material fatigue and degradation over repeated launches. Fiberglass's damage resistance and longevity make it a final choice for this project, by ensuring secure motor retention and design reliability throughout the propulsion system's operational lifespan.

Finally, The aft fins (wings) will be fabricated using carbon fiber plates with fiberglass layering, chosen for their high rigidity, structural strength, and lightweight properties to endure high-speed flight conditions. Carbon fiber was specifically selected due to its low density and high strength-to-weight ratio, ensuring the fins remain structurally stable without adding excessive mass to the aft section. Given that the motor is located at the rear of the rocket and is already a significant source of weight, it was essential to minimize additional mass in this region to keep the center of gravity forward and maintain the required stability margin. Since the aft fins are larger than the canards, a denser material like titanium or aluminum would have negatively

impacted the CG positioning, potentially making the rocket less stable. By utilizing carbon fiber with fiberglass reinforcement, the design ensures optimal aerodynamic performance, reduced aft weight, and improved overall stability, keeping the CG within the necessary caliber range for the scaled project while maintaining structural integrity during flight.

The table below presents the materials and their densities used in this scaled project model, selected to optimize structural integrity, aerodynamic performance, and stability. Each material was analyzed using OpenRocket software to ensure it meets project requirements while maintaining the desired center of gravity and center of pressure balance for optimal flight performance.

Table 5.1 – Final Material Selection for Scaled Sidewinder Missile

Component	**Material**	**Material Density (g/cm^3)**
Nose Cone	3D-Printed Carbon Fiber-Infused PETG	1.4
Canards	Titanium or Aluminum	4.5
Avionics Bay	3D-Printed Carbon Fiber-Reinforced Composite	1.6
Main Body Tubes	Fiberglass	1.8
Motor Retainer	Fiberglass Reinforced with Epoxy	1.8
Aft Fins (Wings)	Carbon Fiber Plates with Fiberglass Layering	1.6
Parachute	Polyethylene	0.000131

5.2 Component Specifications and Budgeting

5.2.1 Component Specifications

The pressure sensor selection for the nose cone is a crucial aspect of this project, as it directly impacts the accuracy of aerodynamic testing and shockwave interaction analysis. The final sensor model and specifications will be determined after conducting CFD simulations to identify the optimal pressure range required for accurate data collection. However, the Microsensor Small Size Pressure Sensors, manufactured by Dubai Sensors Company in Dubai, United Arab Emirates, have been identified as the primary candidate for this application. These sensors are designed for compact, high-precision pressure measurement and are particularly suitable for applications with limited installation space, such as nose cones and control surfaces in high-speed aerospace testing.

The selected pressure sensors have a diameter range of 12.6 mm to 19 mm and a height as small as 6.5 mm, making them ideal for integration within the 3D-printed nose cone without significantly altering its aerodynamic profile. These sensors are compatible with stainless steel and Viton, ensuring durability and resistance to environmental factors during flight and ground testing. The nose cone's 3D-printed design allows for precise sensor placement, enabling seamless CAD modifications to integrate the sensors at optimal positions.

For this project, a minimum of 10 pressure sensors will be installed along the length of the nose cone, spaced evenly to capture pressure variations across the surface. These five key measurement points will be analyzed in both CFD simulations and physical testing, ensuring consistency and accuracy between numerical and experimental results. The testing phase, scheduled for April, will validate the CFD predictions and provide real-world aerodynamic data critical for design verification and performance optimization.

Figure 5.1 - Air Pressure Sensors from Dubai Sensors [48]

With the material transition of the canards from 3D-printed carbon fiber-infused PETG to metallic alternatives (aluminum or titanium), the integration of pressure sensors will be optimized by direct welding onto the canard surfaces. This method enhances structural integrity and eliminates the need for separate mounting housings, which would have added complexity and potential weak points. Similar to the nose cone, each canard will be equipped with five pressure sensors, evenly distributed along its entire length to capture pressure variations and shockwave interactions at critical points. These sensor locations will also be simulated and analyzed using CFD for comparative validation against experimental data.

The pressure sensors will be wired to the avionics bay, which houses the battery and data collection system. However, one design challenge is that the wiring will be exposed to the freestream, potentially affecting aerodynamic performance and introducing disturbances in the local pressure readings. To mitigate this issue, the wires will be strategically routed and adhered to the canard surfaces using aerodynamically smooth adhesives or tapes, ensuring they remain as flush as possible to minimize flow disturbances. Special attention will be given to ensuring that sensor readings are not affected by turbulence generated by protruding wires, preserving the accuracy of pressure measurements in laminar flow conditions. This design modification aims to reduce aerodynamic interference while maintaining data accuracy for both CFD and real-world testing.

The body tube is designed as a modular three-part structure, connected by couplers and shear pins to accommodate assembly, maintenance, and recovery system integration. This segmented configuration allows for optimized material distribution, ensuring that each section is tailored to its specific function while maintaining structural integrity and aerodynamic efficiency. The first body tube, which serves as the primary structural section, integrates multiple critical components, including the nose cone, avionics bay, and canards. This tube measures 8.94 inches in length, with an outer diameter of 3.5 inches and an inner diameter of 3.25 inches. The avionics bay is securely housed in this section, providing a stable enclosure for GPS, power systems, and pressure sensors. Additionally, precisely cut slots in this tube allow for fins to be inserted. This section holds all the critical components for this project.

Connected via a coupler and shear pin mechanism, the second body tube is dedicated to housing the shock cord, parachute, and recovery equipment. This section measures 28.4 inches in length, with the same inner and outer diameter as the first tube, ensuring structural continuity. This tube accommodates recovery wadding and deployment mechanisms, which assures safe descent and reusability after launch.

The third and final body tube is designed exclusively for motor integration, providing a dedicated propulsion section. This tube features a motor mount with an outer diameter of 3.3 inches and an inner diameter of 2.7 inches, specifically designed to house a Cesaroni Technology Inc. 5604M1830-P motor with a secure fit. The motor is centered by two fiberglass centering rings, ensuring alignment and stability during high-thrust ignition and flight. The aft section also accommodates the fins, which are inserted into precisely machined slots for optimal aerodynamic performance. To reinforce this high-stress region, a fiberglass layering will be applied between the wings and body tube, providing structural reinforcement and smooth airflow. This reinforcement process is carefully executed to minimize aerodynamic disturbances

while maximizing durability, assuring that this section withstands the mechanical loads and stresses associated with propulsion and vibrations.

For this project, the Cesaroni Technology Inc. 5604M1830-P motor was selected due to its high thrust output that satisfies L3 requirements, optimal burn time, and high compatibility with the designed airframe for the project. This M-class motor, part of the Pro75-4G series, provides a total impulse of 5,586 Ns, which aligns well with the thrust requirements for achieving the desired velocity and Mach number to execute the purpose of the project while ensuring stability throughout the flight. The average thrust of 1,824 N and a maximum thrust of 2,301 N provide more than enough acceleration to overcome drag and gravitational forces, ensuring a controlled ascent. The burn time of 3.06 seconds balances high impulse with efficient energy release, minimizing excessive stress on the airframe while maintaining a smooth and stable thrust curve. The C-Star propellant was chosen for its consistent burn characteristics, allowing for predictable and constant flight performance, which is important for aerodynamic testing and pressure sensor validation. The Pro75-4G case is reloadable, making this motor a cost-effective option for multiple launch tests required for this research. The motor's diameter of 2.95 inches fits precisely within the motor mount, ensuring a secure installation with minimal modifications. Given that the project involves testing shockwave interactions and stability behavior, the thrust curve of this motor (As displayed in Figure 5.2) supports gradual acceleration until reaching the desirable Mch number for testing, and reducing the risk of abrupt aerodynamic instabilities.

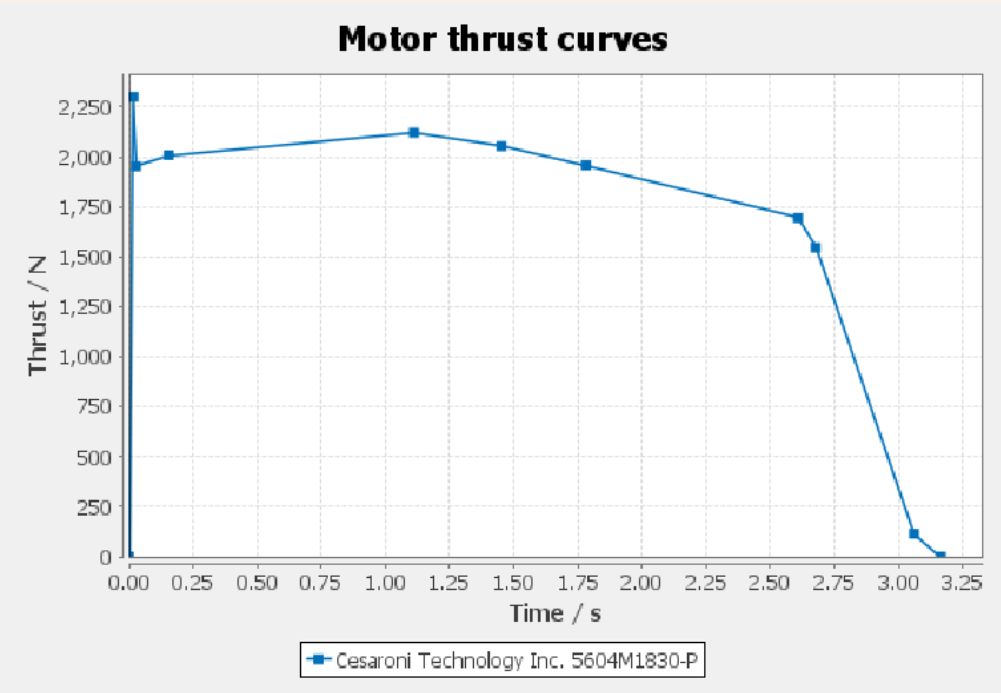

Figure 5.2 - Thrust Curve of the Cesaroni Technology Inc. 5604M1830-P

The full specifications of the motor are detailed in the table below, summarizing its key characteristics and performance parameters.

Table 5.2 – Cesaroni Technology Inc. 5604M1830-P Motor Specifications

Specification	Value
Manufacturer	Cesaroni Technology Inc.
Motor Name	5604M1830-P
Motor Class	M-Class
Total Impulse	5,586 Ns (96% M)
Average Thrust	1,824 N
Maximum Thrust	2,301 N
Burn Time	3.06 seconds
Launch Mass	160 oz
Empty Mass	65.5 oz
Motor Type	Reloadable
Case Info	Pro75-4G
Propellant Type	C-Star
Motor Diameter	2.95 inches
Motor Length	24.4 inches

5.2.2 Budgeting

The funding and budgeting for this project have been carefully calculated to ensure that all critical components are covered with balancing cost-effectiveness with high performance. The total estimated budget of $6,850 accounts for essential expenses, each justified by its functionality and necessity in a high-power rocketry project. 3D printing materials and machining ($550) are required for prototyping and fabricating custom components such as aerodynamic surfaces and structural reinforcements. Custom pressure and temperature sensors ($600) are crucial for collecting real-time aerodynamic data that are needed to validate computational simulations, and ensuring flight safety. Carbon fiber sheets ($400) provide structural reinforcement, offering a high strength-to-weight ratio essential for withstanding aerodynamic forces. The most significant expense, three M-class testing motors ($2,000), is

necessary for propulsion testing and Level 3 certification, with each motor costing several hundred dollars. Motor casing ($650) is a vital component designed to house the motor while enduring extreme temperatures and pressures, ensuring safety and reusability. Body tubes, couplers, centering rings, parachutes, and shock cords ($1,700) make up the rocket's airframe and recovery system, requiring durable materials like fiberglass and phenolic tubing to sustain high-speed flight and safe recovery. Test site access and certification costs ($100) are included to cover necessary launch site fees and regulatory compliance. Avionics supplies and GPS tracking ($400) are essential for real-time navigation, altitude tracking, and telemetry, ensuring the rocket's safe recovery and flight analysis. Additionally, adhesives, epoxies, and other consumables ($200) are required for assembly, reinforcement, and last-minute modifications. Each item in the budget is based on standard industry costs and reflects the demands of supersonic flight, high-power rocketry, and precision engineering. This well-planned budget ensures that the project is adequately funded for successful design, testing, and certification while maintaining cost efficiency and reliability.

Table 5.3 – Cost Breakdown of Project

3D Printing Materials and Machining	$ 550
20 Custom Pressure and Temperature Sensors	$ 600
Carbon Fiber Sheets	$ 400
3 Testing motors (M classification)	$ 2000
Motor Casing	$ 650
Body tubes, Couplers, Centering Rings, Parachutes, and Shock chords.	$ 1700
Test Site Access and Certification Costs	$ 100
Avionics Supplies/GPS	$ 400
Additional Supplies or Replacement Parts (Epoxy, Adhesives, etc..)	$ 200
Project's Total Estimated Budget	**$ 6,650**

5.3 Flight performance Parameters

The flight performance predictions indicate that the rocket is well-suited to achieve the objectives of the project. With an apogee of 3,765 feet and a maximum velocity of 958 ft/s (Mach 0.982), the rocket is capable of reaching high altitudes while maintaining stability, as indicated by the 1.95 caliber margin. The velocity off the launch rod (48.9 ft/s) ensures a safe

and controlled ascent, while the optimum delay of 20.6 seconds aligns well with the expected time to apogee. Additionally, the velocity at deployment (944 ft/s) and max acceleration (383 ft/s²) suggest that the rocket will undergo significant aerodynamic forces, which emphasize the importance of structural integrity, which requires further FEA considerations. The total flight time of 55 seconds allows for sufficient observation and data collection, making the test flight a strong candidate for validating the project's goals, including the evaluation of the nose cone and canard design under realistic flight conditions. Overall, these results indicate that the rocket's performance is within expected parameters, ensuring a successful execution of the planned experiments hopefully.

Table 5.4 – Flight Performance Parameters in SI Units

Flight Parameter	**Value**
Velocity off Rod	14.90 m/s
Apogee	1147.57 m
Velocity at Deployment	287.73 m/s
Optimum Delay	20.6 s
Max Velocity	~300 m/s (Mach 0.982)
Time To Apogee	11.6 s
Flight Time	34.4 s`
Ground hit Velocity	61.26 m/s
Stability	1.95 cal 9.452%
Center of Gravity (CG)	0.78 m
Center of Pressure (CP)	0.96 m at M = 0.3

6. Computational Analysis and Final Design Decision

This section outlines the core analytical phase of the project, which is critical in determining the optimal nose cone configuration to advance into the construction and experimental testing stages. The designs proposed in Section 6 will undergo two major forms of simulation: Computational Fluid Dynamics (CFD) and Finite Element Analysis (FEA). Among these, CFD serves as the primary tool for project evaluation, as it provides the essential insights into the pressure distribution and flow characteristics around the nose cone and canard assemblies. The central aerodynamic feature being investigated is the static pressure acting on the canards, which directly correlates to the level of flow activity and control authority in high-speed regimes. A design that generates higher pressure on the canards indicates more active and connected airflow, which is desirable for enhanced maneuverability and aerodynamic effectiveness. Furthermore, CFD analysis will be used to identify the stagnation pressure located at the tip of each nose cone configuration, as this point experiences the highest pressure due to the deceleration of the incoming airflow. This maximum pressure value is not only a key aerodynamic parameter but also serves as the critical loading condition that will be transferred into the FEA models.

The CFD simulations conducted in this study are entirely pressure-based, as pressure data alone provides a robust foundation for analyzing shockwave strength, flow attachment, and overall aerodynamic performance once all boundary conditions are properly defined. By focusing on pressure-based results, the analysis remains efficient and tightly aligned with the primary objective of the project, which is to evaluate how nose cone geometries influence flow behavior and pressure distribution across the canards. Following the CFD simulations, the stagnation pressure values will be applied as boundary conditions in the FEA models to assess the structural response of the nose cone under operational aerodynamic loads. This will help determine whether each design maintains its structural integrity without experiencing critical stress concentrations or material failure. Additionally, the FEA results will aid in material selection and optimization by revealing how different materials respond to the pressure-induced forces. Through this integrated simulation approach; first using CFD to capture aerodynamic behavior, then using FEA to validate structural feasibility, the project ensures that the selected nose cone design will not only perform effectively in flight conditions but also withstand the physical demands associated with high-speed operations. Ultimately, the most promising configuration identified through this analysis will proceed to the fabrication phase, where it will be tested to validate the simulation data and confirm the core concept of the entire project.

6.1 Computational Fluid Dynamics

6.1.1 CFD Setup and Boundary Conditions

For the purposes of this study, SolidWorks Flow Simulation was selected as the primary CFD tool due to its user-friendly interface, integrated wind tunnel setup, and built-in automation features that streamline the simulation process. The software provides automated meshing capabilities, intelligent error detection, and setup recommendations that make it ideal for iterative studies involving geometric variations, such as those present in the different blunt nose cone configurations analyzed here. One of the key advantages of using SolidWorks Flow Simulation is

the “Goals and Probes” feature, which allows users to place point probes, surface goals, and global goals across the flow domain. These tools make it possible to collect localized data such as static pressure, total pressure, velocity vectors, Mach number, temperature gradients, and flow trajectories. The collected numerical data can later be compared to experimental readings from pressure sensors during physical testing, ensuring a solid link between the CFD predictions and project real-world validation.

In this analysis, a total of ten pressure probes were deployed for each simulation run, with their positions carefully selected to represent common locations across all three nose cone geometries. These probe points include the tip of the nose cone to capture stagnation pressure, multiple positions along the surface of the canards to evaluate local pressure behavior and flow attachment, and additional points located at each significant geometric inflection or curvature shift across the nose cone surface. This uniform setup allows for direct comparative analysis between the different designs and helps isolate the effects of shape variation on shock wave interaction and aerodynamic loading.

The computational domain was shaped as a simplified wind tunnel focused exclusively on the critical areas of interest, which are the nose cone and canard assembly, extending slightly downstream of the canards to ensure flow development beyond these structures. The wind tunnel’s dimensions were set at 33 inches in length, 12 inches in width (depth), and 9 inches in height, with an extended inlet section to allow the incoming airflow to fully develop before reaching the test geometry. This spatial configuration helps reduce entrance effects and stabilizes the simulation by ensuring well-formed boundary layers and turbulence properties upon contact with the nose cone.

Boundary conditions were defined to replicate high-speed conditions corresponding to a Mach 1 (sonic) airflow, with a velocity inlet set at 345 m/s, assuming standard sea-level conditions (temperature = 288.15 K, pressure = 101325 Pa). The outlet boundary was set to ambient atmospheric pressure, completing a pressure-velocity coupling setup. Because the study involves compressible flow characteristics, SolidWorks' compressible flow option was activated to accurately model shock formations, pressure discontinuities, and local temperature changes.

Meshing was performed automatically, with a resolution set to 1% of the computational domain, which represents the finest element size that SolidWorks Flow Simulation can reliably generate for this type of study. This mesh density ensures that small-scale flow features, such as shockwave transitions and boundary layer separation around the canards and nose tip, are captured with sufficient fidelity. Additionally, adaptive mesh refinement (AMR) was allowed near high-gradient regions, particularly around the nose tip and canards, to further increase accuracy in those zones of interest.

The simulation also employed local mesh controls around the nose cone surface to ensure proper element density near walls, aiding in the accurate calculation of surface pressure and shear stress. Turbulence was modeled using the k-ε turbulence model, which provides a good balance between computational efficiency and the ability to predict turbulent wake behavior and shockwave/boundary layer interactions in high-speed external flows.

The combination of careful boundary condition setup, targeted probe placement, and refined meshing strategies ensures that the CFD results provide detailed insight into the aerodynamic performance and flow dynamics of each nose cone design. The output from these simulations, particularly the stagnation pressure at the nose tip and pressure distribution across the canards- will be carried over to the subsequent FEA phase, where they will serve as applied loads to test structural resilience and material suitability under expected operational conditions.

6.1.2 Nose Cone CFD Discussion and Results

6.1.2.1 Blunted Elliptical Nose Cone CFD

The CFD analysis of the blunted elliptical nose cone at Mach 1 in **Figure 6.1** provides a detailed understanding of the aerodynamic behavior and pressure distribution across the nose cone and its attached canard surfaces. This configuration was simulated under compressible, steady-state conditions within a wind tunnel with flow inlet was set to a velocity of 345 m/s, which represents sonic conditions at sea level, while the outlet was assigned a boundary condition of atmospheric pressure. A refined meshing strategy was employed, with a resolution of 1% of the domain size and automatic local refinement enabled near regions of high gradients, particularly around the nose cone tip and canard edges. The k-ε turbulence model was used to capture turbulent wake formation and shock-boundary layer interactions, which are critical for accurately predicting high-speed aerodynamic phenomenons.

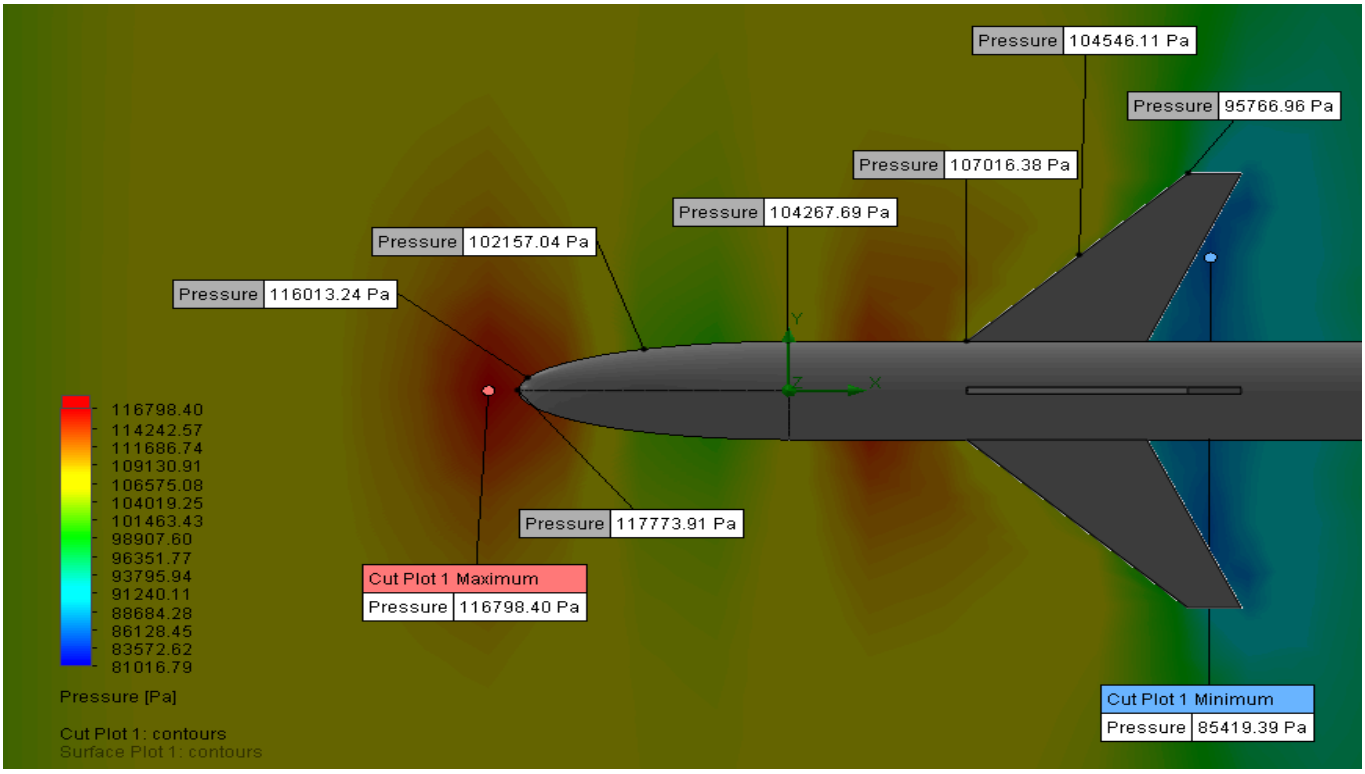

Figure 6.1 - Blunted elliptical nose cone pressure field

One of the defining features of the blunted elliptical nose cone is its smooth, continuous surface gradient that transitions from the rounded tip into the cylindrical body. Unlike sharper configurations, this geometry reduces flow separation and ensures a more gradual pressure change across the nose surface. The curvature effectively guides the airflow without causing abrupt compressions, which in turn influences both the stagnation zone and the strength of the generated shockwaves. Due to this smooth transition, pressure probes were specifically placed at key aerodynamic locations to gather meaningful data. The first probe was located at the tip of the nose cone, capturing the maximum stagnation pressure, which measured approximately 116798.40 Pa. This point represents the location where the incoming airflow is brought to rest, experiencing the highest pressure concentration due to the full conversion of kinetic energy into pressure energy.

The second probe was placed at the mid-section of the nose cone curvature, where the geometry is transitioning, and the airflow begins to accelerate along the body. This area reflects the change in pressure due to the slope of the elliptical surface, capturing the impact of curvature on local static pressure. The third probe was positioned at the junction between the nose cone and the main body coupler, an important location that marks the end of the nose's curved surface and the start of the cylindrical fuselage. The flow behavior here reflects how well the geometry maintains attached flow, and the pressure value helps validate the effectiveness of the gradient transition in preventing early separation.

Moving toward the control surfaces, a fourth probe was placed at the root of the canard, right where it attaches to the fuselage, to measure the local pressure environment at the canard's base. The fifth and sixth probes were located along the mean aerodynamic chord of the canard; one at the leading edge and one at the trailing edge. The leading-edge probe captures the high-pressure spike typical of supersonic flow hitting a sharp surface, and in this case, it shows a substantial increase in pressure due to localized shock interactions. The trailing-edge probe, on the other hand, recorded the minimum pressure in the simulation domain, measuring around 98419.39 Pa, indicating a significant acceleration and pressure drop, which is typical of flow exiting the control surface and potentially undergoing slight separation. This sharp pressure differential across the canard surface confirms the generation of lift and provides useful data for evaluating aerodynamic forces acting on the control surface.

A notable feature in the pressure contour is the intensity and structure of the shockwave formed around the nose cone. Despite being a blunt configuration, the elliptical shape reduces the abruptness of the shockwave, resulting in a relatively smoother bow shock. The color gradient shifts gradually from red near the stagnation region to green and blue further downstream, which indicates a moderate shockwave strength compared to sharper geometries. This smoother transition means that while a strong pressure buildup exists at the tip, the downstream flow is less disturbed, resulting in a cleaner boundary layer around the canards and body tube. However, the intensity of the bow shock is still sufficient to influence the pressure field around the canards, contributing to elevated pressure values near the leading edges.

The CFD analysis confirms that the blunted elliptical nose cone offers a favorable aerodynamic profile by generating a manageable stagnation pressure, reducing shockwave intensity, and ensuring stable flow attachment to downstream components. The pressure probe data validates the concept of using a smooth transition geometry to influence flow behavior positively, maintaining active flow around the canards and reducing excessive shock-induced drag. These detailed insights will be essential in guiding the structural FEA simulations and informing future design iterations which will be discussed in the following sections.

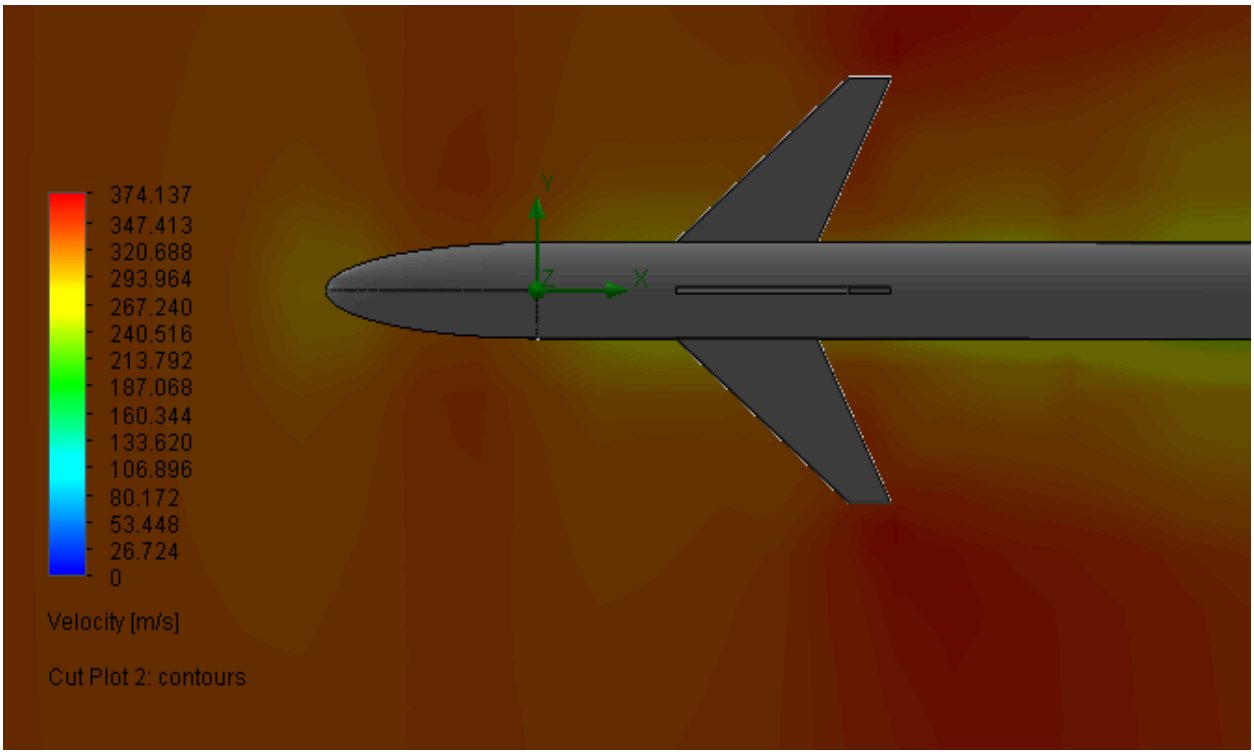

Figure 6.2 - Blunted elliptical nose cone velocity field

The velocity field demonstrated in **Figure 6.2** is critical for understanding how the airflow accelerates, decelerates, and interacts with the nose cone curvature, canards, and the overall Body Tubing geometry. The results are shown in meters per second, ranging from approximately 26.72 m/s (blue) in the wake and stagnation zones to a maximum of 374.14 m/s (red) where flow acceleration occurs, exceeding even the inlet speed due to localized compressibility effects.

The most significant feature in the velocity field is observed at the nose tip, where the incoming flow is abruptly decelerated, forming a stagnation region. In this zone, the velocity drops nearly to zero (indicated by the darkest blue contour) which matches the location of the previously identified maximum pressure point. This is expected in compressible flow at supersonic speeds, as the high-speed air is forced to halt at the frontal surface, converting kinetic energy into pressure energy. This stagnation region is bounded by a bow shock, which is not

sharply visible in the velocity plot alone but can be inferred by the rapid color gradient transition surrounding the nose.

Downstream of the stagnation point, along the curved elliptical surface of the nose, the flow gradually accelerates, which is evident from the transition from blue to green to yellow contours. This smooth acceleration is a direct result of the geometrical gradient of the blunted elliptical shape, which promotes controlled flow attachment and minimizes the abrupt shock interactions typically associated with sharp or conical noses. Unlike conical tips that generate strong detached shock waves with high drag penalties, the elliptical form reduces the strength and abruptness of the bow shock, maintaining better pressure and velocity control near the body.

Along the body tube, the airflow stabilizes and remains relatively attached, as shown by the uniform velocity bands parallel to the body surface. However, just ahead of the canards, there is a noticeable local acceleration zone, especially around the canard leading edges. This effect occurs due to the compression and redirection of the flow as it meets the thin leading edge, forming a localized high-speed zone (yellow-orange). It is in these regions that the velocity reaches peak values above 345 m/s, exceeding the inlet velocity, which is typical in compressible flows where shock-enhanced acceleration occurs at sharp features.

Just behind the canards and toward the trailing body section, the velocity field starts to show signs of flow separation and wake formation. The drop in velocity and the spread of cooler colors (green to blue) indicates turbulent mixing and pressure recovery zones, where the airflow becomes less organized and begins to detach from the body. This wake is also an important contributor to form drag, and its behavior is influenced heavily by the upstream geometry, flow alignment, and the presence of control surfaces.

It is also important to note the symmetry and uniformity of the velocity contours across the vertical mid-plane, suggesting a well-aligned and stable flowfield with minimal asymmetric interference or vortex shedding under these steady-state conditions. This supports the aerodynamic stability of the blunted elliptical nose and its integration with the body and canard layout.

In summary, the velocity field confirms the aerodynamic advantages of the blunted elliptical nose cone by demonstrating a controlled stagnation zone, gradual flow acceleration, and strong, attached flow along the canards. The presence of localized velocity peaks near the leading edges and reduced velocities in the wake region provide important information for estimating lift, drag, and thermal loads. These results not only validate the flow quality and behavior predicted in the pressure contour analysis but also serve as critical inputs for performance evaluations and future design optimizations.

6.1.2.2 Power-Law/Von Karman Nose Cone CFD

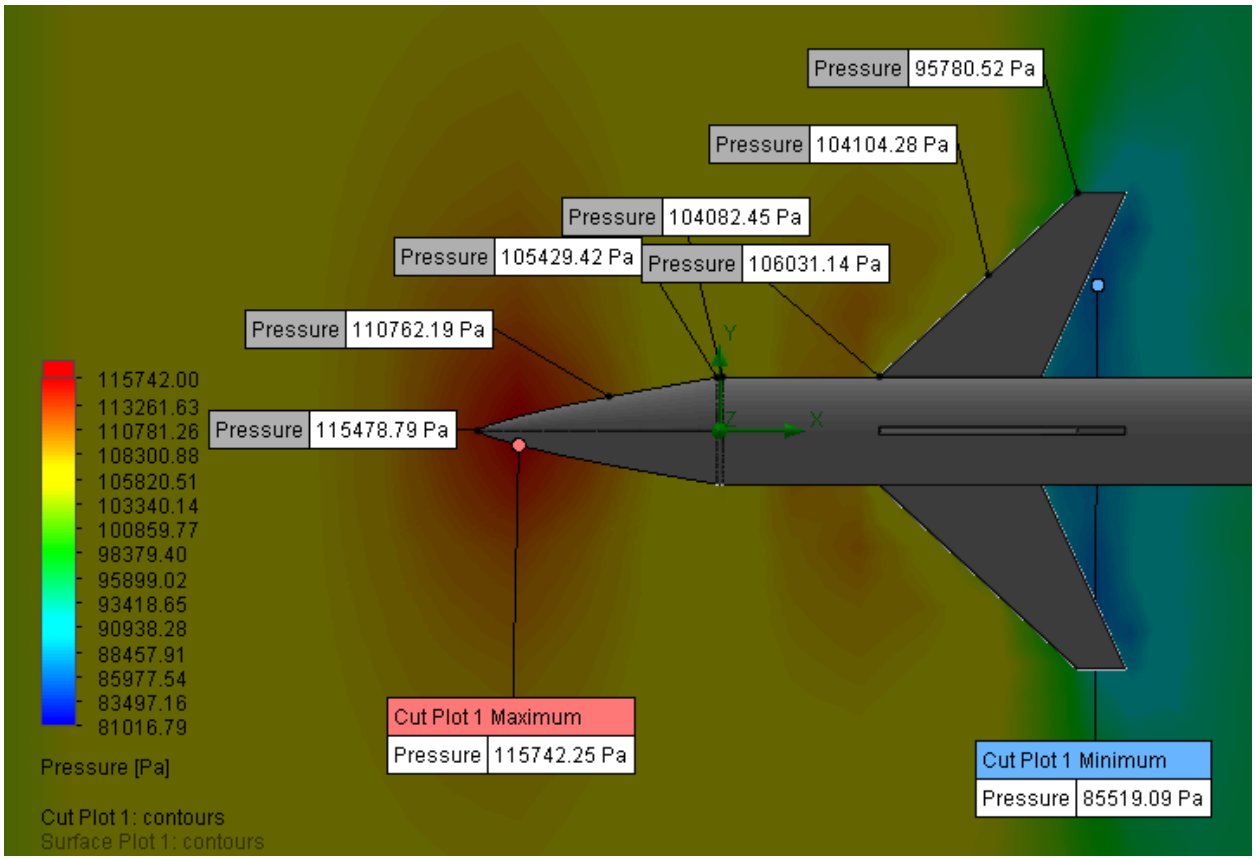

Figure 6.3 - Power-Law/Von Karman nose cone pressure field

The CFD pressure and flow field of the Power-Law/Von Kármán nose cone displayed in **Figure 6.3** provides enough understanding of the aerodynamic behavior under high-speed compressible flow conditions. This simulation offers the needed insights about both forebody performance and canard control effectiveness. The Von Kármán geometry, rooted in slender-body theory, is derived mathematically to minimize pressure gradients and wave drag, offering great aerodynamic efficiency compared to blunt or conical configurations. It features a continuously smooth curvature from the tip to the base, allowing for progressive airflow redirection and pressure recovery, thus significantly reducing the formation of strong detached shocks.

The pressure contour plots confirm these theoretical benefits. At the sharply pointed nose tip, a maximum stagnation pressure of approximately 115742.25 Pa is recorded near the front surface, which is a value slightly lower than that observed in blunter geometries, such as the elliptical nose cone (~116798.40 Pa). This reduced stagnation pressure is a direct result of the Von Kármán profile's ability to soften the intensity of the bow shock, allowing for a more oblique and surface-attached shock that leads to lower wave drag and enhanced boundary layer stability. The transition in pressure is smooth along the body, with no abrupt spikes, indicating that flow separation is minimal or absent in the forebody region.

Due to the sharpness of the nose tip, direct probe and real life pressure sensor placement at the exact stagnation point was not feasible. Instead, seven pressure probes were strategically placed to capture essential aerodynamic data along the most critical flow interaction zones and geometrical changes. The first probe was positioned slightly aft of the tip along the initial curvature, where the flow begins its deceleration. The second probe lies at the midsection of the nose cone's curved surface, capturing pressure values as the curvature gradient begins to soften and redirect the flow. The third probe is located at the junction between the nose cone and the cylindrical body tube, a structurally important transition where the pressure stabilizes and the flow fully transitions from a curved to a straight streamline. Two additional probes were placed slightly above and below the axial centerline around this geometric junction to detect any asymmetries or disturbances in the pressure field that could arise from real-world manufacturing imperfections.

Downstream, the sixth probe was located at the base of the canard, marking the first surface that directly interacts with the high-speed, compressible flow. At this location, mild flow stagnation and localized compression occur, producing an elevated pressure reading (~106031.14 Pa) that indicates a controlled shock interaction at the root. The seventh probe was placed at the leading edge of the canard, near the mean aerodynamic chord, capturing a significant pressure spike due to the formation of a localized leading-edge compression shock. Conversely, the trailing edge of the canard, also positioned along the mean aerodynamic chord, recorded the minimum pressure in the simulation domain (~85519.09 Pa), signifying flow acceleration and expansion as the flow exited the control surface. The differential between these two pressure points along the canard chord confirms that the surface is subjected to a strong normal force, ideal for lift production and control authority in a supersonic environment.

The flow behavior around the nose and canards further emphasizes the aerodynamic advantages of the Von Kármán design. The velocity field displayed in **Figure 6.4** shows smooth acceleration of the airflow around the curvature with no indications of early separation or recirculation zones upstream of the control surfaces. This ensures that the canards are immersed in high-energy, attached flow, a condition that is vital for their effectiveness. The pressure distribution pattern across the canard confirms this: with high pressure on the leading edge and significantly lower pressure at the trailing edge, the resulting pressure gradient is steep and uniform, indicating predictable and responsive control behavior. In compressible flow, particularly at Mach 1, such a configuration aligns with modified thin airfoil theory, which expects leading-edge shock compression followed by trailing-edge expansion, which is an ideal condition for stable lift generation with minimized drag penalties.

The nature of the shockwave observed in the simulation further supports these conclusions. Unlike blunter geometries that produce intense, detached bow shocks, the Von Kármán profile generates a weaker, oblique, and surface-attached shockwave that remains close to the geometry. The pressure contours transition smoothly from red near the tip to yellow, green, and blue downstream, indicating gradual deceleration and energy dissipation. This controlled pressure gradient reduces the risk of turbulent separation, enhances pressure recovery, and improves the aerodynamic quality of the flow encountered by downstream components like the canards. The symmetrical nature of the pressure distribution on both sides of the body also suggests a stable

and balanced aerodynamic configuration, free from lateral asymmetries or instabilities under steady-state conditions.

From a control standpoint, the results predict that the canards on this configuration will exhibit decent aerodynamic responsiveness and linear control authority, particularly for small to moderate deflection angles. The presence of a clean, attached boundary layer around the root and consistent pressure gradients across the chord ensures that the hinge moment required for actuation will remain within manageable limits, and that control inputs will yield stable and proportional aerodynamic responses. The large pressure differential from root to tip also implies that the aerodynamic center of pressure on the canards remains well-defined and predictable, which is vital for flight control system modeling and real-time feedback systems in test flight.

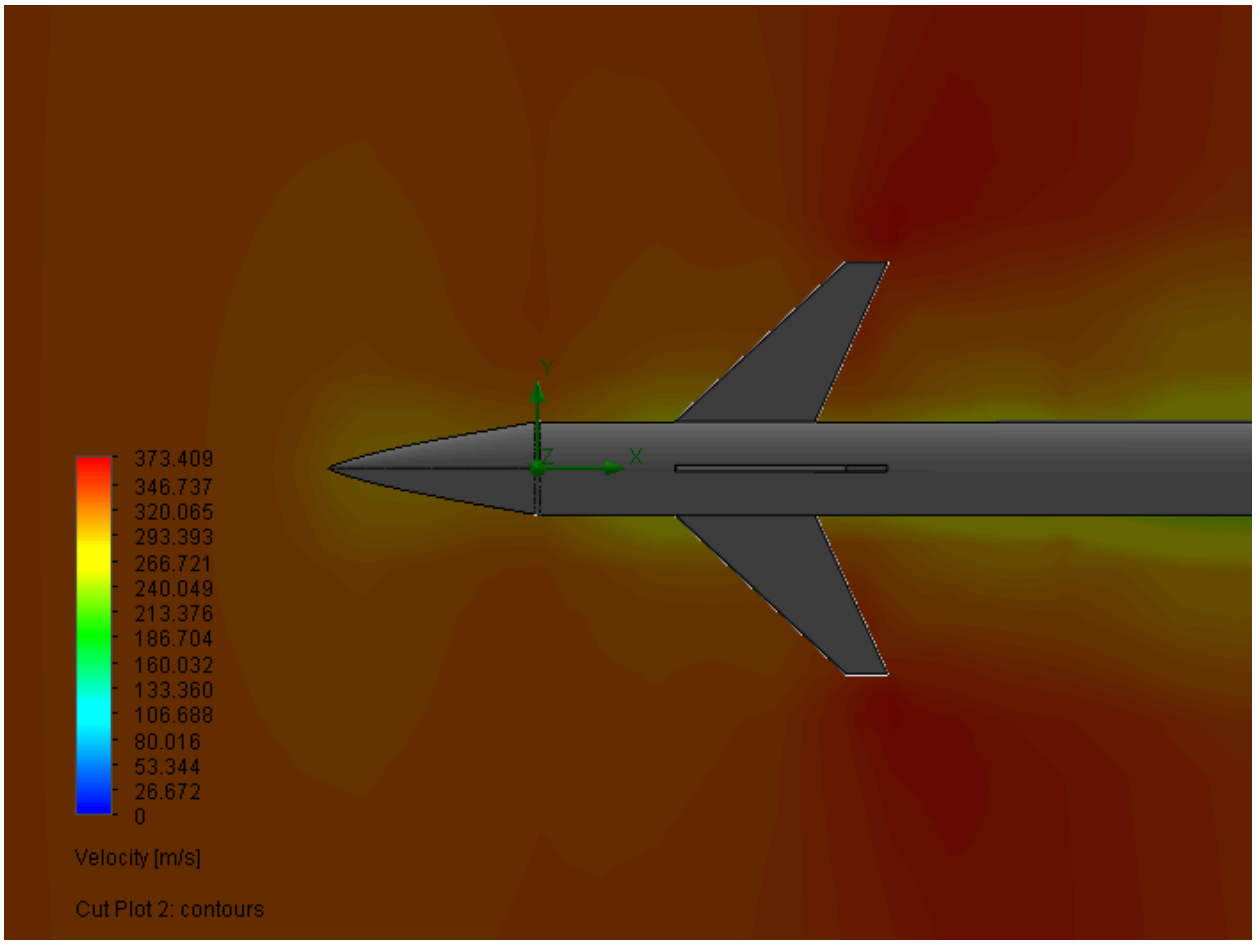

Figure 6.4 - Power-Law/Von Karman nose cone velocity field

The velocity contour plot clearly displayed in the velocity field in **Figure 6.4** illustrates the flow dynamics as air interacts with the sharp nose, smooth forebody, and the attached canards. Color gradients in the plot range from approximately 26.67 m/s in the stagnation and wake zones to 373.41 m/s in regions of accelerated flow, providing a high-resolution understanding of airflow acceleration, deceleration, and directional behavior.

At the tip of the nose cone, the simulation captures a well-defined stagnation zone, where the airflow slows down to near-zero velocity due to direct frontal impact. This stagnation region is a classic behavior in compressible flows, where kinetic energy is fully converted into pressure. What distinguishes the Von Kármán geometry, however, is how it manages the flow from this stagnation point forward. Thanks to its mathematically derived and continuously smooth curvature, the air accelerates gradually along the nose cone surface without detachment. The velocity field transitions smoothly from blue to green to red, confirming that the boundary layer remains attached and stable throughout the forebody. This behavior stands in contrast to sharper or blunter geometries, which tend to induce strong detached bow shocks and flow separation at similar speeds.

One of the most notable aerodynamic advantages observed is the presence of a surface-attached, oblique shock wave along the nose cone. While not explicitly visualized as a shock in the velocity plot, its effects are inferred from the sudden changes in velocity magnitudes and flow compression near the tip. The Von Kármán nose generates a weaker and more surface-aligned shockwave, minimizing energy loss and reducing wave drag. This controlled deceleration and redirection of flow around the nose ensures that air arriving at downstream components (especially the canards) remains energetic and coherent. In several regions, local velocities even exceed the freestream Mach 1 input, with values reaching up to 373.41 m/s. This suggests localized expansion and compressibility-induced acceleration around curved surfaces, validating the theoretical efficiency of the Power-Law slope in supersonic flow environments.

Moving aft, the flow maintains a high level of organization as it encounters the canards. Here, the velocity field is especially important because it determines the quality of the air interacting with the control surfaces. The velocity contours show that the flow approaching the canards is smooth, symmetric, and energetic, suggesting that the surfaces are fully immersed in high-speed, attached flow. This is crucial, as control surfaces function most effectively when they are operating in clean, undisturbed airflow. The leading edge of each canard experiences a localized deceleration due to normal shock interaction, followed by a recovery and expansion along the trailing edge. These characteristics match what is expected in supersonic thin airfoil behavior, where the difference in pressure, driven by changes in velocity, is a key contributor to lift and control force generation.

Furthermore, the overall symmetry of the velocity field along the longitudinal axis reflects the aerodynamic balance of the vehicle. There are no signs of asymmetrical flow separation, vortex shedding, or lateral instability, all of which are potential risks at transonic speeds. Instead, the field maintains a clear and symmetric wake pattern, with flow velocities gently tapering off behind the body and canards. The velocity reductions in the downstream region, visualized by the shift to green and blue shades, represent the formation of a controlled wake. This wake remains narrow and organized, indicating that wave drag and turbulent separation are being effectively minimized by the geometry of the nose cone and body.

Altogether, the velocity field analysis confirms the exceptional aerodynamic performance of the Power-Law/Von Kármán nose cone under Mach 1 flight. The nose geometry successfully manages stagnation pressure, promotes efficient flow acceleration, and limits shock strength, while the attached canards benefit from a high-quality flow environment, ensuring reliable and

responsive control behavior. The pressure and velocity differentials across the canard surfaces reinforce the aerodynamic force generation predicted in earlier analyses, and the clean flow behavior seen in the velocity field supports assumptions made about canard effectiveness in pitch or yaw maneuvering. These aerodynamic observations, when taken together, validate the Von Kármán profile not just as a low-drag nose shape, but as a carefully optimized forebody design capable of supporting high-speed flight with precision control, minimal shock-induced disturbances, and superior flow management across the entire vehicle envelope.

6.1.2.3 Spherically Blunted Conic Nose Cone CFD

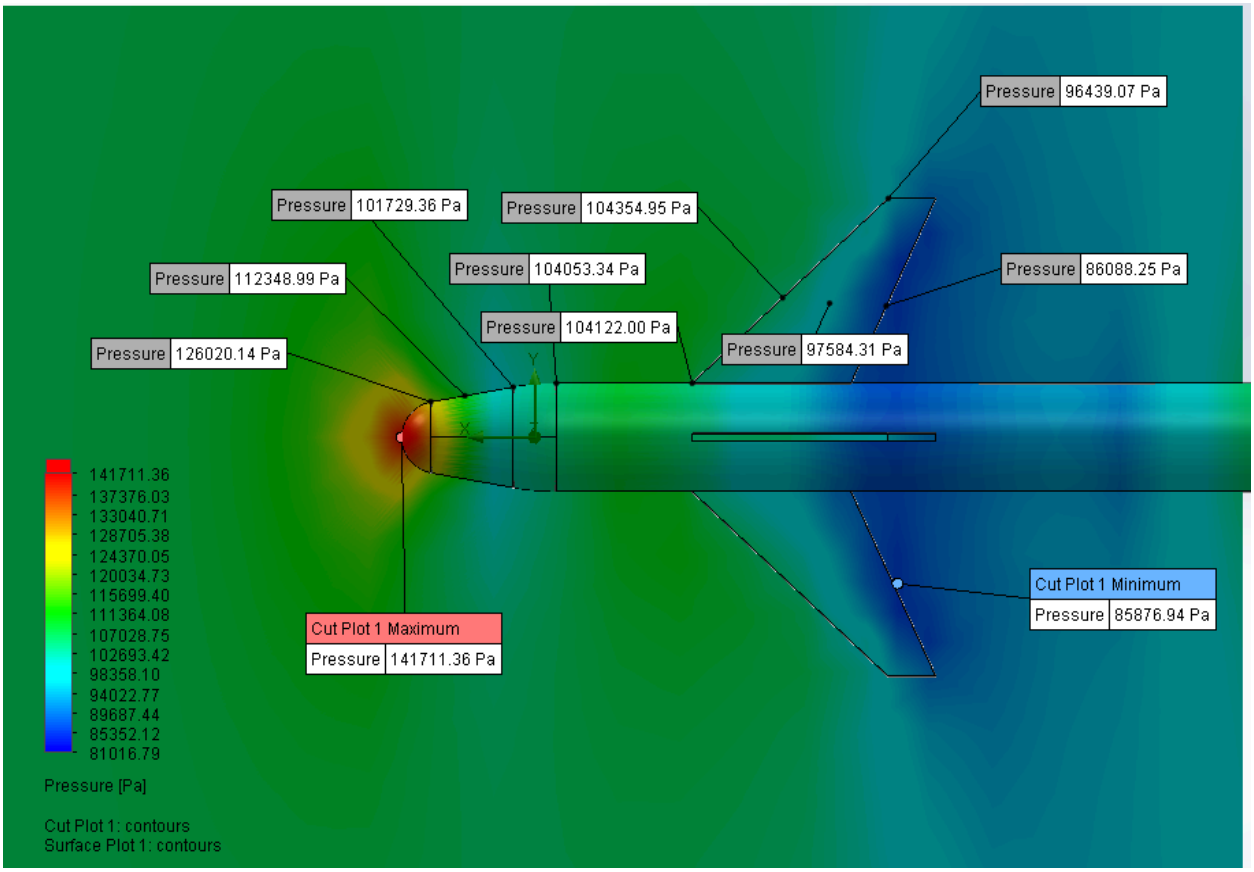

Figure 6.5 - Spherically Blunted conic nose cone pressure field

The Spherically Blunted Conic profile combines the geometric sharpness of a conical body with a hemispherical front cap, which significantly influences the shockwave intensity, pressure distribution, and flow stability along the vehicle. The data extracted from the simulation of the pressure field of this nose cone as displayed in **Figure 6.5** offers the needed insights into the shock structure, forebody pressure behavior, and control surface interaction with the flow.

The Spherically Blunted Conic Nose Cone consists of two distinct geometric sections, a spherical cap followed by a straight conical taper, each governed by different equations. This

varying geometry leads to complex flow behavior, particularly at supersonic speeds. To understand these effects, ten pressure probes were strategically placed at locations of geometric transitions where flow behavior is most affected.

Probes were placed at the nose tip (to capture stagnation pressure), at the end of the spherical cap, and at two points along the conical taper, the midpoint of its steepest slope and its base. One probe was positioned at the junction between the nose cone and the body tube, with two more located just above and below this transition to detect pressure asymmetries. Additional probes were placed at the canard root, the leading edge along the mean aerodynamic chord, and the trailing edge, which recorded the minimum pressure due to local flow expansion. This probe layout provides a detailed map of pressure behavior across critical aerodynamic regions. The nose generates a strong, detached bow shock, resulting in steep pressure gradients and elevated wave drag. The conical section further accelerates the flow, while the canards operate in a compressed, shock-influenced flowfield. These data are essential for evaluating control effectiveness and guiding structural and aerodynamic optimization.

At the forefront of the nose cone, the simulation captures a strong, localized stagnation point at the center of the hemispherical cap. This location reaches the maximum recorded pressure of 141711.36 Pa, indicated as "Cut Plot 1 Maximum" in the CFD output. This is the highest pressure encountered among the nose cone geometries analyzed thus far, which is consistent with expectations for a blunt body at supersonic speeds. The abrupt deceleration of the flow at this point leads to the formation of a strong detached bow shock, located slightly ahead of the nose tip. This shock compresses the air significantly before it flows around the body, resulting in high-pressure gradients and increased wave drag relative to more gradually sloped geometries like the Von Kármán or elliptical profiles.

As the flow travels around the spherical blunt tip and transitions to the conical section, the pressure begins to drop off but remains elevated compared to smoother geometries. Pressure probes placed along the nose and conical body capture this transition. The first reading beyond the stagnation zone, 126020.14 Pa, reflects the immediate post-shock compression. Further downstream, at the beginning of the conical surface, the pressure drops to 112348.99 Pa, followed by 101729.36 Pa at mid-cone. This pressure gradient confirms a relatively steep decay, typical of conical surfaces following strong bow shock formation. The rapid drop in pressure around this area also increases the risk of boundary layer separation, particularly under off-design conditions or angle-of-attack variations.

At the junction between the nose cone and the cylindrical body, pressure stabilizes to approximately 104122.00 Pa, indicating that the flow begins to reattach or become more uniform after passing the conical slope. The pressure on the canard root, captured at 104053.34 Pa, is relatively high, suggesting that shock-induced compression effects are still present in this region. This elevated pressure persists slightly farther upstream of the canards, where the flow remains influenced by the earlier shock structures.

On the canard leading edge, the pressure increases again to 104354.95 Pa, confirming the interaction between the high-speed flow and the control surface. This region experiences local flow impingement and compression, likely forming small-scale shocks or stagnation zones

depending on the angle of attack. However, downstream along the canard trailing edge, the pressure drops significantly to 86088.25 Pa, and even further down the body, the wake zone registers a minimum pressure of 85876.94 Pa, marked as "Cut Plot 1 Minimum." This steep pressure differential across the canard chord indicates a strong aerodynamic force generation, validating that the canard is actively contributing to control authority. The trailing-edge expansion suggests that lift is being generated in this region and that subsonic expansion zones are forming in the wake due to reduced flow energy and pressure.

Further downstream along the fuselage, the flow fully reattaches, but the pressure remains somewhat lower compared to the forebody, with readings of 97584.31 Pa just aft of the canards and 96439.07 Pa closer to the rear fin. This continued low-pressure region reflects the turbulent wake zone, which results from the strong upstream shock, boundary layer thickening, and shear layer development typical of blunt body flowfields.

The pressure contour as a whole reveals the influence of the spherical bluntness: the color transition from red to green and finally blue shows a rapid and intense deceleration at the nose tip, followed by steep gradients along the conical sides and a wide, low-pressure wake downstream. The shockwave generated by this geometry is intense and fully detached, with energy losses that are higher than in smoother, elongated designs. While this design offers good internal volume capacity and ease of manufacturing, it comes with increased wave drag and greater stagnation heating, which are important factors in both structural design and thermal protection system (TPS) considerations.

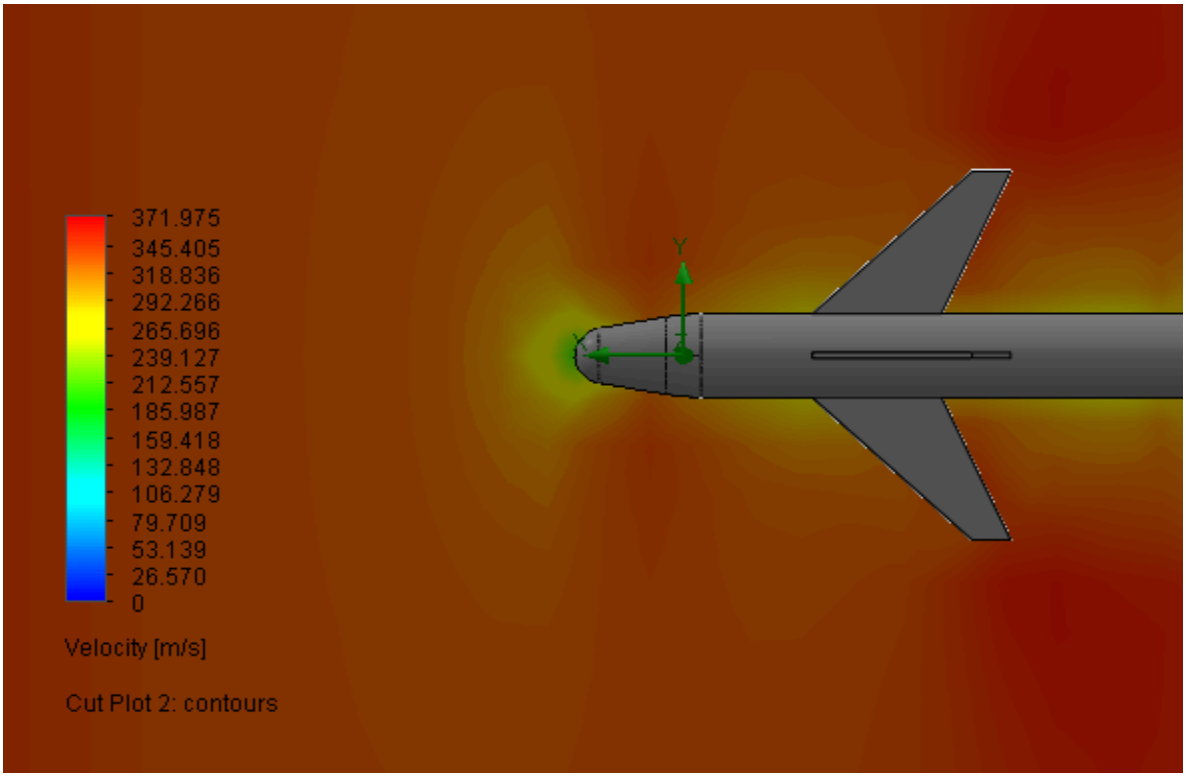

Figure 6.6 - Spherically Blunted conic nose cone velocity field

The velocity field analysis of the Spherically Blunted Conic Nose Cone under Mach 1 conditions that is displayed in **Figure 6.6** reveals the distinct aerodynamic behavior resulting from its geometry. This configuration is characterized by a hemispherical front cap followed by a straight conical taper which produces a flow response that reflects both the advantages and aerodynamic penalties of combining bluntness with angular transitions. The CFD results, presented through a velocity contour plot ranging from 0 m/s to approximately 372 m/s that visualizes the airflow interacts with this geometry of interest.

At the very front of the nose cone, a pronounced stagnation region is observed, which was noted as the max pressure in the pressure field analysis. This area, marked by deep green to blue coloring, indicates where the incoming supersonic flow is abruptly brought to rest, forming a large zone of near-zero velocity. This behavior is a direct result of the detached bow shock that forms ahead of the spherical cap, typical of blunt nose geometries. The presence of this strong normal shock leads to significant compression of the flow, increasing pressure but simultaneously causing an energy loss that manifests as reduced velocity and elevated drag.

As the flow moves past the stagnation region and wraps around the hemispherical surface, it begins to accelerate along the conical taper. This transition is marked by a gradual change in contour color (from green and yellow to orange and red) as the air is directed around the nose and re-energized. The conical section plays a critical role here by gradually redirecting the flow downstream, helping to reattach and stabilize the boundary layer. However, due to the blunt nature of the forebody, some flow disruption persists, and complete reattachment is delayed further along the body.

The downstream region, including the canard and mid-body tube sections, shows mostly attached and energetic flow, represented by red and orange shades close to the freestream velocity of 345 m/s. The flow reaching the canards remains relatively stable, though it passes through a mildly compressed environment shaped by upstream shock structures. While this provides enough energy for the canards to function effectively, the presence of upstream compression and boundary layer development can influence control surface performance, especially under dynamic conditions or at varying angles of attack.

Farther downstream, in the wake region behind the nose-body junction and aft of the canards, the velocity field shows a slight return to green and darker orange hues. This indicates flow deceleration and minor separation, a result of the body's abrupt geometry transitions and the energy loss across the bow shock. While the wake is not as large or turbulent as in purely blunt bodies, it still reflects momentum loss that contributes to overall form drag.

Importantly, the entire flow field appears symmetrical along the longitudinal axis, which suggests a balanced aerodynamic response under these conditions. There is no evidence of lateral instability, asymmetric vortex shedding, or off-axis flow detachment, which supports stable flight behavior at Mach 1.

In summary, the velocity field of this nose cone displays a flow pattern dominated by a strong stagnation zone, intense shock-induced compression, and rapid but controlled acceleration along the conical taper. While the geometry supports structural strength and internal volume, it

imposes aerodynamic costs in the form of strong bow shocks, flow separation tendencies, and a modest wake region. These characteristics confirm that while functional and robust, this nose cone configuration trades aerodynamic efficiency for structural simplicity and thermal survivability, making it more suitable for missions where blunt-body performance outweighs drag reduction priorities at lower speeds.

6.2 Finite Element Analysis

6.2.1 FEA Setup and Boundary Conditions

In this section, the focus shifts from the aerodynamic assessment provided by the CFD analysis to the structural evaluation of the three nose cone designs through Finite Element Analysis (FEA) to test the material choice and design geometry characteristics. With the CFD process completed, one of the most critical outputs, which is the stagnation pressure. This output serves as the foundation for this next phase. The stagnation pressure represents the maximum total pressure experienced by the surface when a high-speed flow is brought to rest at a point, typically at the tip of the nose cone. This parameter is vital not only for defining aerodynamic performance but also for guiding the selection of pressure sensors for the real-world experimental validation stage, as well as determining the critical loading conditions for structural simulations.

For the purpose of this FEA, the stagnation pressure is interpreted as the peak normal force per unit area that the nose cone experiences during flight. In compressible flow (particularly at supersonic speeds) this pressure arises due to a combination of airflow deceleration, density increase, and shockwave-induced compression at the leading edge. As predicted by both theoretical models and confirmed by CFD results, this maximum loading consistently occurs at the nose tip for all three designs under consideration. The confluence of high velocity, high density, and normal impact flow results in the tip becoming the focal point for pressure accumulation and stress concentration.

To simulate this effect in the FEA environment, the stagnation pressure value for each nose cone was extracted from the CFD data and applied as a concentrated pressure load over a small, uniform surface area at the tip. For this study, a 5 mm diameter circular region (0.005 m) was defined on the nose tip of each design. This simplification ensures consistency across geometries and mimics the localized impact zone seen in high-speed compressible flows. The total force applied in the FEA is calculated by multiplying the stagnation pressure of each nose cone by this surface area, resulting in a precise load condition reflective of in-flight aerodynamic stresses. These calculated forces are then visualized and applied in the FEA models, as shown in **Figure 6.7**.

For this simulation, the applied force derived from the stagnation pressure is modeled as a concentrated load with magnitudes that will be calculated later in the section, acting normal to the surface of the nose cone tip. This loading condition creates a simplification to an aerodynamic force resulting from high-speed airflow impinging directly on the nose tip during flight. To properly constrain the model for structural simulation, a fixed boundary condition was applied at the base of each nose cone. This boundary condition is justified by the physical

configuration of the nose cone in the assembled vehicle, where the base is rigidly connected to the body tube and structural coupler. These components mechanically secure the nose cone during operation and are designed to resist axial, lateral, and torsional displacements. As such, treating the base as fixed accurately simulates the structural support the nose cone would experience when mounted on the vehicle. This simple boundary condition is sufficient for this simulation because the primary deformation and stress concentration are expected to occur near the tip, where the load is applied. The fixed base ensures that any resulting stress or displacement is due solely to the applied aerodynamic loading, resulting in a clear understanding of the structural response and failure potential of each nose cone geometry under maximum operating pressure.

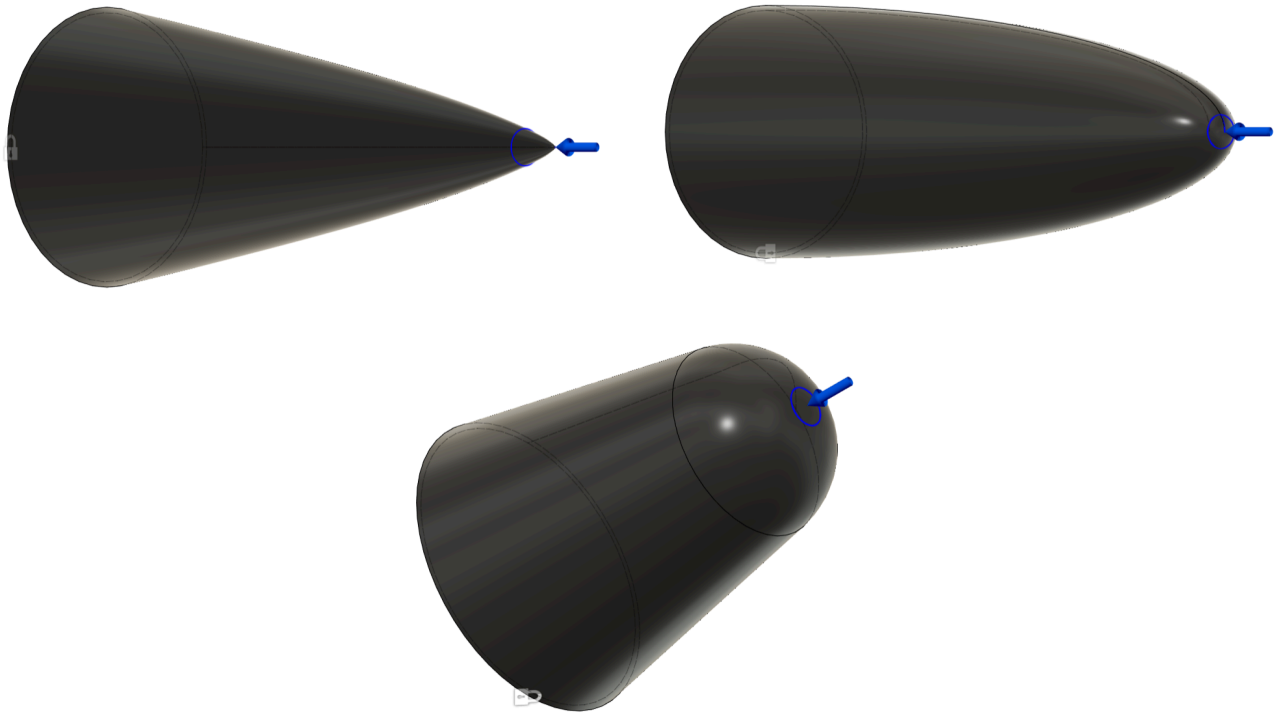

Figure 6.7 - Force applied over a 5 mm diameter area at nose cone tip

The FEA analysis was performed using Autodesk Fusion 360's Static Stress module, selected for its ease of use, quick setup, efficient editing, and automatic meshing capabilities. For meshing, the simulation utilized Fusion 360's 1% element size setting, which is the smallest mesh resolution the software allows. This fine mesh provided higher accuracy by increasing the number of elements and capturing localized stresses more effectively, particularly around the nose cone tip where the load was applied.

In conclusion, this section has established the methodology for translating aerodynamic loads into structural inputs using stagnation pressure from CFD results. With the loading and

boundary conditions defined, the following sections will present the FEA results for each of the three nose cone designs, evaluating how their geometry and material selection respond to high-speed aerodynamic forces to come up with the final decision of the manufactured nose cone for testing.

6.2.2 Nose Cone FEA Discussion and Results

6.2.2.1 Blunted Elliptical Nose Cone FEA

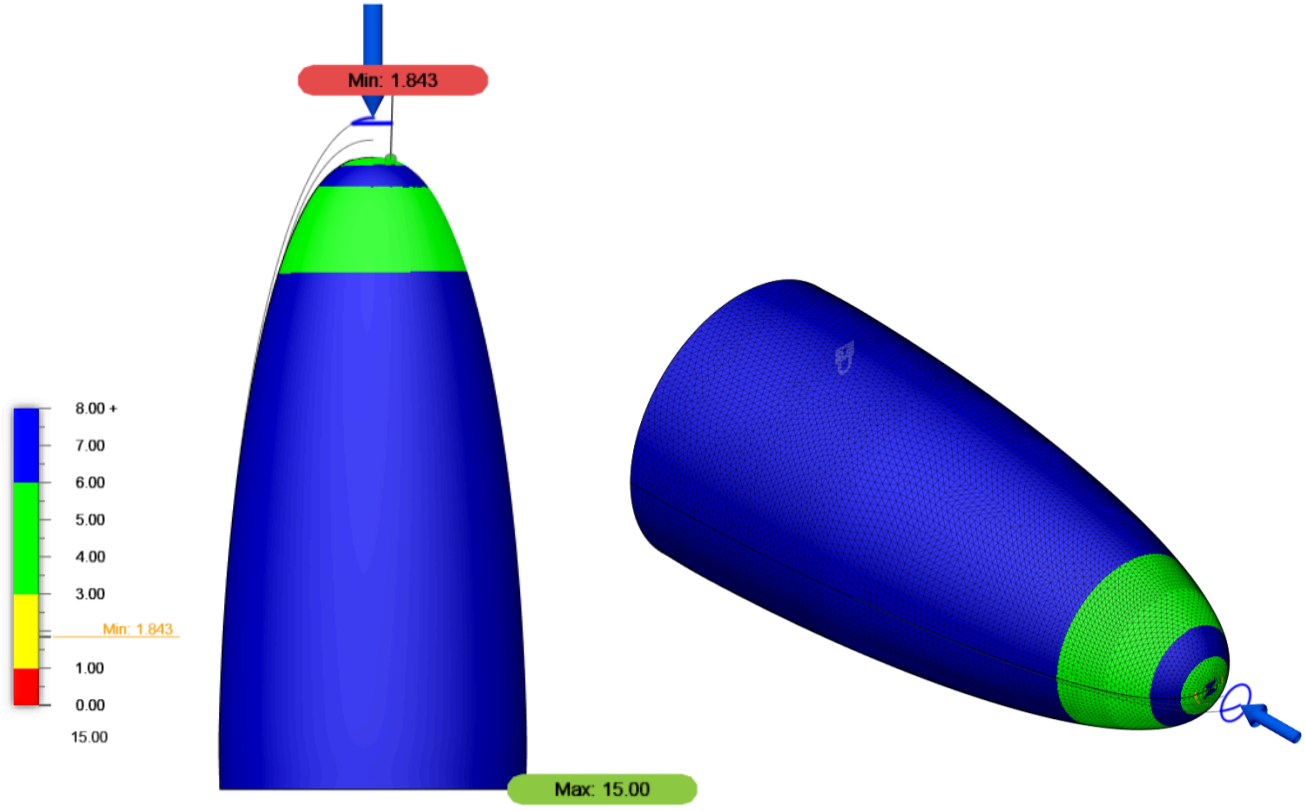

Figure 6.8 - Static stress FEA results for the blunted elliptical nose cone

The Finite Element Analysis of the Blunted Elliptical Nose Cone that is displayed in **Figure 6.8** was performed using Autodesk Fusion 360's Static Stress module to evaluate the structural integrity of the design under aerodynamic loading conditions derived from the CFD results that was run on the first nose cone of interest. This analysis serves as a critical step in validating the nose cone's ability to withstand the extreme forces encountered at Mach 1 flight and make a final selection between the 3 nose cones of interest. The primary objective for this specific analysis was to understand how the chosen material (PETG) and the geometry of this blunted elliptical profile respond to high-pressure, compressible airflow, particularly at the tip, where stagnation pressure is most significant and reveal if this shape shows any outstand among other shapes.

From the CFD results, the maximum stagnation pressure was determined to be 117,773.91 Pa, occurring at the nose tip due to the abrupt deceleration of high-speed airflow. To simulate this in the structural analysis, the corresponding force was calculated using the fundamental relation $F = P \times A$, where P is the stagnation pressure and A is the surface area subjected to this pressure. For consistency across all analyzed nose cone geometries, a 5 mm diameter circular region (approximating 0.005 m^2 for calculation purposes) was defined at the tip of the nose cone as the application zone, which will equal to a force of 588.87 Newtons. This small and localized region replicates the real-world aerodynamic loading experienced by the nose tip under supersonic conditions. The calculated force was then applied normally to the tip surface, accurately representing the direction of airflow impact.

The material used in this simulation was PETG, selected for its favorable balance of mechanical performance and convenient manufacturability for this project. PETG offers a tensile strength of approximately 50 MPa, a Young's modulus of around 2 GPa, and a yield strength in the range of 45–50 MPa. It is widely used in aerospace prototyping due to its impact resistance, ease of 3D printing, and moderate structural performance, though it lacks the high-temperature resistance and stiffness of advanced composites.

The simulation results, as visualized in the safety factor plot, revealed a minimum safety factor of 1.843, located at the apex of the nose cone where the aerodynamic force was applied. This indicates that under the specified conditions, the material is nearing its yield limit in this localized region. The rest of the structure, particularly the mid-body and base, showed safety factors well above 8, with values reaching the capped display maximum of 15, suggesting that these regions experience very low stress and offer a substantial structural margin.

The color-coded safety factor map highlights a red-to-yellow gradient near the tip, transitioning to green and blue across the body. This gradient confirms that the tip is the most critical structural zone, consistent with theoretical predictions and aerodynamic load patterns in high-speed flows. The concentrated stress at the tip suggests that while the PETG nose cone is structurally stable for early-stage testing and prototyping, it approaches critical stress thresholds under full supersonic load. Any additional load like thermal, vibrational, or dynamic, could potentially compromise the structural integrity in this region.

In conclusion, the Blunted Elliptical Nose Cone made of PETG demonstrates a structurally sound but stress-concentrated behavior under Mach 1 loading. The analysis confirms the design's suitability for prototyping, wind tunnel testing, and conceptual validation, while also identifying the tip region as a potential point of failure under extreme conditions. With a minimum safety factor of 1.843, the design passes this simulation phase but warrants further material or geometric refinement for high-speed operational readiness, or maximizing printed material thickness on the tip of the nose cone. The following sections will compare this performance with that of the other two nose cone geometries to evaluate the role of shape in stress distribution and overall structural resilience.

6.2.2.2 Power-Law/Von Karman Nose Cone FEA

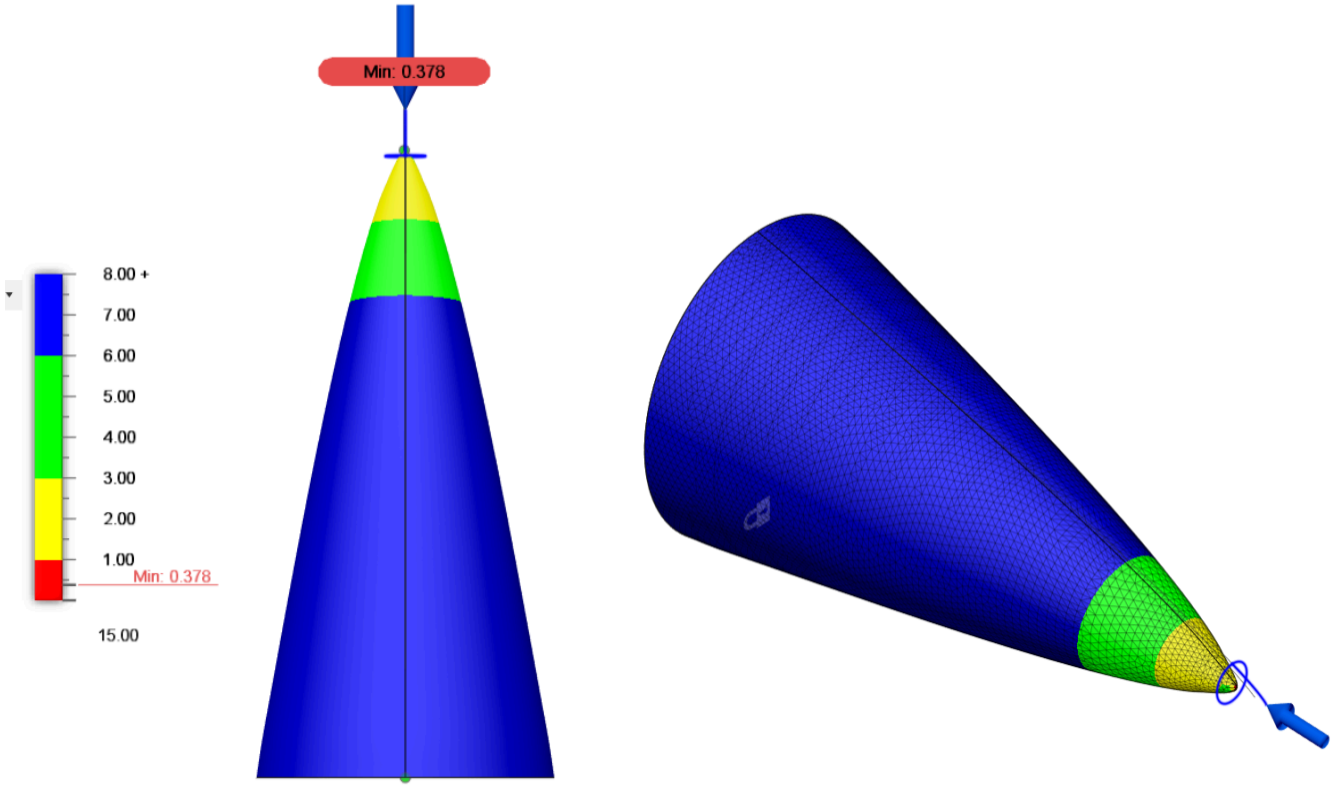

Figure 6.9 - Static stress FEA results forPower-Law/Von Karman nose cone

The Finite Element Analysis of the Power-Law/Von Karman Nose Cone that is displayed in **Figure 6.9** was performed using Autodesk Fusion 360's Static Stress module to evaluate the structural integrity of the design under aerodynamic loading conditions derived from the CFD results that was run on the second nose cone of interest. The FEA conducted using Autodesk Fusion 360's Static Stress module to assess its structural response under peak aerodynamic loads. The aerodynamic loading condition was derived from CFD simulation results, specifically from the maximum stagnation pressure, which occurs at the nose tip due to the compressible, high-speed airflow experienced at Mach 1. This structural study aimed to evaluate whether the geometry of the Von Kármán nose, known for its aerodynamic efficiency, could also maintain more structural resilience among other nose cones under supersonic conditions when manufactured from PETG.

The stagnation pressure used for this simulation was directly obtained from the CFD analysis and had a value of 115,478.79 Pa, recorded at the tip of the Power-Law/Von Kármán nose cone. To apply this as a structural load in the FEA, the pressure was converted into a force using the equation $F = P \times A$, where P is the stagnation pressure and A is the area over which the force acts. In this study, the area was defined as a 5 mm diameter circular region, equivalent to 0.005 m^2, representing the small, localized zone of aerodynamic impact at the tip. This calculation yielded a total applied force of approximately 577.39 N, which was applied normally to the nose

tip surface. This setup accurately replicates the concentrated aerodynamic loading condition experienced during supersonic flight, where the flow stagnates and transfers peak pressure directly to the frontmost point of the nose cone.

The FEA results for the Power-Law/Von Kármán nose cone reveal a significant structural vulnerability concentrated at the tip of the geometry. While this nose cone shape is known for its aerodynamic advantages which were discussed earlier like minimizing wave drag and promoting laminar flow, the simulation highlights the severe stress concentration it introduces when subjected to high-speed stagnation pressure, particularly when manufactured using PETG. The analysis shows a minimum safety factor of just 0.378 at the tip, well below the acceptable threshold for structural safety, indicating a clear risk of failure in this region under operational conditions. This low safety factor confirms that the sharp taper of the tip, although beneficial for aerodynamic performance, becomes the most critical structural point where stress drastically exceeds PETG's yield strength. The rest of the nose cone body performs well, maintaining high safety margins, but the tip's geometry and load application area create a bottleneck for structural integrity.

Given that material substitution is not an option for this project, it becomes evident that selecting the Power-Law/Von Kármán shape for a supersonic application using PETG is structurally unsound unless careful adjustments are made. However, since the component will be 3D printed in real life, a practical solution would be to increase the wall thickness locally at the tip to help distribute stress over a broader volume and reduce peak concentration. This approach would take advantage of the flexibility offered by additive manufacturing without significantly compromising aerodynamic performance. Alternatively, this result may suggest that choosing this geometry for this material is inherently a poor match for high-speed, high-load environments. The simulation ultimately underscores that despite its aerodynamic strengths, the Power-Law/Von Kármán nose cone lacks structural robustness at the tip when constructed from PETG, and critical regions such as the apex must be addressed through geometry reinforcement during the design-to-fabrication process.

6.2.2.3 Spherically Blunted Conic Nose Cone FEA

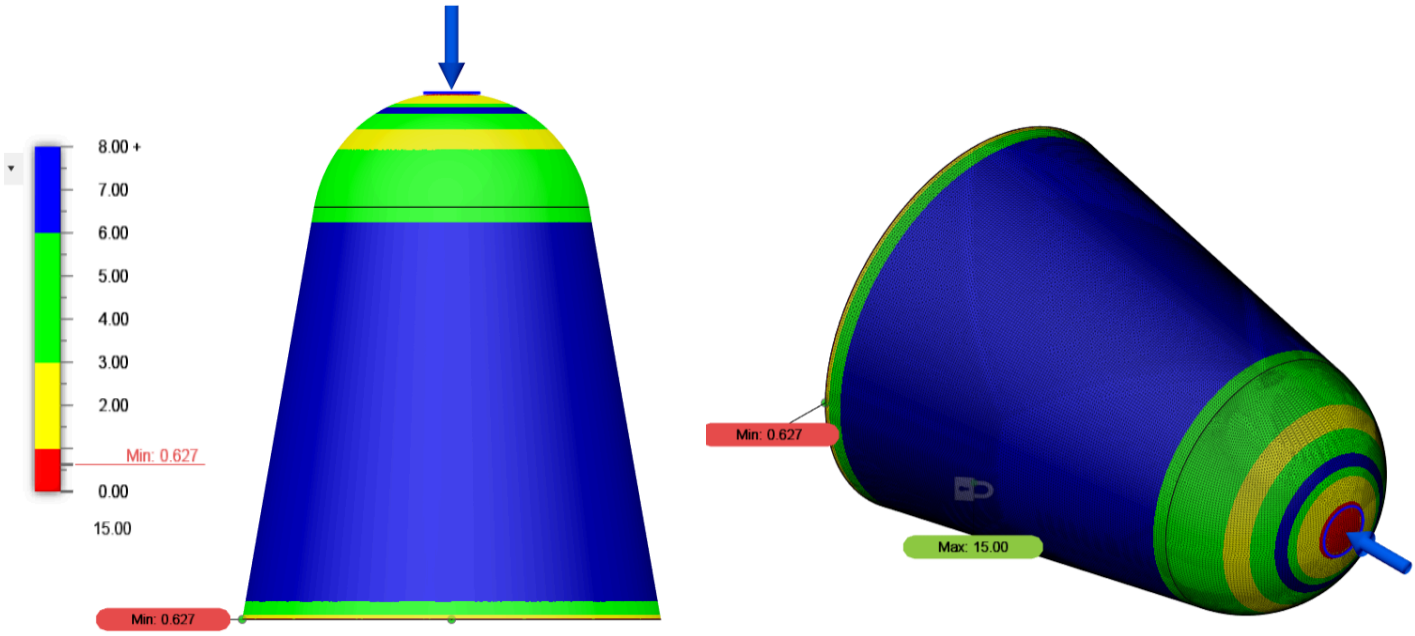

Figure 6.10 - Static stress FEA results for spherically blunted conic nose cone

The Finite Element Analysis of the Spherically Blunted Conic Nose Cone that is displayed in **Figure 6.10** was performed using Autodesk Fusion 360's Static Stress module to evaluate the structural integrity of the design under aerodynamic loading conditions derived from the CFD results that was run on the third nose cone of interest. The FEA conducted using Autodesk Fusion 360's Static Stress module to assess its structural response under max aerodynamic loads. The aerodynamic loading condition was derived from CFD simulation results, specifically from the maximum stagnation pressure, which occurs at the nose tip due to the compressible, high-speed airflow experienced at Mach 1. This structural study aimed to evaluate whether the geometry of the Spherically Blunted Conic nose, could also maintain more structural strength among other nose cones in this project under supersonic conditions when manufactured from PETG.

The stagnation pressure used for this analysis was taken from CFD results and recorded at 141,711.36 Pa, the highest among the three nose cone geometries studied. To convert this pressure into an applicable structural load, the force was calculated using the equation $F = P \times A$, where P is the pressure and A is the surface area exposed to it. For consistency, the application area was defined as a 5 mm diameter circular region, equivalent to 0.005 m^2. This yields a total force of approximately 708.56 N, which was applied perpendicularly to the tip surface, which is simulating the real aerodynamic impact zone at the nose during flight. The fixed boundary condition was applied to the base of the nose cone, representing its attachment to the fuselage via couplers and body tubes. This constraint assumes that the base is fully supported and restricted in

all directions, allowing the simulation to isolate the structural response of the nose cone body to the applied load.

The FEA simulation revealed a minimum safety factor of 0.627, located near the outer rim of the spherical nose tip, where the curvature transitions into the conical region. This value is well below the standard safety threshold of 1.0, indicating that the structure, as modeled in PETG, would likely fail in that region under the given aerodynamic load. The rest of the structure, particularly the mid-cone and base, demonstrated excellent structural stability, with a maximum safety factor capped at 15, showing little to no stress accumulation in those zones. The color distribution on the safety factor map transitions from red and orange near the high-pressure region to green and blue across the rest of the body, confirming that the tip and transition curvature are the most critical stress zones in this design.

This result confirms that the geometry of the Spherically Blunted Conic Nose Cone, while beneficial for shock absorption and thermal shielding in aerothermal environments, introduces significant structural concentration of stress at the nose when constructed from PETG. Unlike the Von Kármán design, where failure is focused sharply at a single point, the blunted conic design spreads the stress slightly over the curvature, but the stress levels remain too high for the selected material to sustain safely.

Because material substitution is not an option, and the component is intended to be 3D printed, a feasible mitigation approach would be to increase wall thickness locally around the nose tip and transition area to better distribute the force and reduce peak stress concentrations. Adjusting the internal print infill density or adding reinforcement rings within the print design could also improve performance while preserving the overall aerodynamic profile. If such reinforcement is not possible, the analysis suggests that this geometry is a poor structural match for PETG under supersonic loads, despite its favorable thermal and aerodynamic behavior.

In conclusion, the FEA of the Spherically Blunted Conic Nose Cone demonstrates that, when fabricated from PETG and exposed to peak stagnation pressure at Mach 1, the design falls below structural safety limits, particularly near the front curvature. The minimum safety factor of 0.627 confirms that this geometry is not structurally viable in its current form without reinforcement. Future implementation of this design must take into account 3D print-based strengthening strategies or alternate applications where aerodynamic forces are reduced.

6.3 Results, Discussion, and Final Decision

6.3.1 Comparison and Discussion

6.3.1.1 CFD Comparison

The comparative analysis of the CFD results for the three nose cone geometries, the Blunted Elliptical, Power-Law/Von Kármán, and Spherically Blunted Conic, reveals significant aerodynamic performance differences in the supersonic regime, particularly at the speed of interest which is Mach 1. Each design presents distinct flow behaviors, stagnation pressures, shock structures, and impacts on downstream control surfaces such as canards. When analyzed through both pressure and velocity fields, the Von Kármán configuration emerges as the most aerodynamically optimized, while the Spherically Blunted Conic proves structurally robust but aerodynamically penalized. The Blunted Elliptical geometry sits between the two, offering a moderate balance between aerodynamic softness and manufacturing practicality.

Starting with the Power-Law/Von Kármán nose cone, this profile was specifically designed to minimize wave drag by maintaining a smooth curvature from tip to base, a characteristic derived from slender-body theory. The simulation results confirm the aerodynamic efficiency of this configuration: the stagnation pressure at the tip (115742.25 Pa) is marginally lower than that of the other two geometries, implying a weaker bow shock and reduced kinetic energy loss. More importantly, the flow remains attached across the surface, with no evidence of upstream separation, and forms an oblique, surface-attached shock instead of a strong detached shock. These flow characteristics create a coherent, energetic boundary layer, ensuring that the attached canards operate in a highly active flowfield, which is essential for responsive and predictable control authority. The pressure differential across the canards is pronounced (from approximately 106031.14 Pa at the root to 85519.09 Pa at the trailing edge) indicating excellent lift generation with minimized shock-induced distortion. The velocity contours also show clean acceleration along the forebody and symmetric wake formation downstream, suggesting low wave drag, reduced flow turbulence, and minimal separation zones. In totality, the Von Kármán geometry offers the most outstanding aerodynamic behavior of the three, providing a favorable blend of low drag, clean shock interaction, and enhanced control effectiveness in a supersonic environment.

The Blunted Elliptical nose cone also shows strong aerodynamic merits but lacks the refined efficiency of the Von Kármán profile. This geometry is characterized by a continuously smooth curvature transitioning into the fuselage, which moderates the shock formation and encourages steady flow attachment. The stagnation pressure here reaches 116798.40 Pa, higher than the Von Kármán but lower than the Spherically Blunted Conic, indicating a stronger shock yet not excessively penalizing. The shock structure is relatively smooth and not sharply detached, and the pressure field shows a gentle transition from the stagnation zone to the downstream regions. This design manages to mitigate abrupt compressions, thereby reducing flow disturbances near the canards. However, the pressure differentials across the control surfaces are less significant compared to the Von Kármán geometry. For example, the trailing edge of the canard records a pressure of around 98419.39 Pa, which is higher than that of the Von Kármán case, suggesting a more conservative flow expansion and possibly weaker lift forces. Velocity plots show a well-behaved flow with minimal wake disruption, but not as clean or rapid an acceleration as

seen in the Von Kármán profile. In terms of practical application, this configuration offers a good compromise between aerodynamic softness and manufacturability. It avoids the complexities of a mathematically ideal shape and still performs adequately in a supersonic flow regime. Nonetheless, in a pure performance ranking based on flow control, shock handling, and canard activation, it ranks second behind the Von Kármán.

In contrast, the Spherically Blunted Conic nose cone displays the most intense aerodynamic penalties, despite offering potential benefits in structural durability and internal volume capacity. The spherical tip introduces a sudden and complete deceleration of the flow, leading to a strong detached bow shock that forms ahead of the body. This geometry generates the highest stagnation pressure among all cases (141711.36 Pa), indicating a substantial energy conversion from kinetic to pressure energy, but at the cost of heightened wave drag and potential thermal loading. The pressure decay along the conical surface is steep, with values falling from 126020.14 Pa post-stagnation to 101729.36 Pa at mid-cone. This gradient implies a rapid boundary layer thickening, increasing the risk of separation under dynamic flight conditions. The pressure on the canards is heavily influenced by the upstream shock structure, with leading-edge values reaching up to 104354.95 Pa and trailing edge pressures plunging to 86088.25 Pa. While this gradient does indicate lift generation, it is achieved in a disturbed and highly compressed flowfield, potentially reducing control predictability and responsiveness. Moreover, the velocity field is characterized by a large stagnation zone, slower reattachment of the boundary layer, and a wider turbulent wake, all contributing to an increase in form drag. From an aerodynamic standpoint, this design is least favorable for supersonic maneuvering, although its bluntness may be desirable for specific mission requirements like thermal protection or housing large payloads.

In conclusion, when ranking the three nose cone geometries based on their ability to handle supersonic speeds, the Power-Law/Von Kármán nose cone stands out as the most aerodynamically efficient and responsive design. It exhibits the lowest stagnation pressure, cleanest flow attachment, most effective canard immersion in active flow, and lowest induced drag. The Blunted Elliptical design follows with a good performance profile marked by moderate stagnation pressure, smooth shock transitions, and respectable control surface engagement. Finally, the Spherically Blunted Conic design, although structurally advantageous, is penalized by high stagnation pressure, detached shock formation, and increased wave drag, making it the least desirable from an aerodynamic standpoint in supersonic regimes. Therefore, in the context of optimizing nose cone shapes for maneuverability, shockwave management, and flow control at Mach 1, the Von Kármán configuration is the superior choice, promising optimal performance across a wide operational envelope.

6.3.1.2 FEA Comparison

The Finite Element Analysis conducted on the three studied nose cone geometries of interest (Blunted Elliptical, Power-Law/Von Kármán, and Spherically Blunted Conic) reveals crucial insight into their structural viability when subjected to supersonic stagnation pressures that could alter the final decision for this project, specifically under Mach 1 flow conditions. The analysis aimed to rank the configurations in terms of mechanical integrity, considering that all geometries were fabricated from polyethylene terephthalate glycol (PETG). While CFD

simulations identify aerodynamic efficiency through pressure gradients and flow smoothness, FEA complements this by identifying whether the material and geometry can resist the localized and distributed loads generated by stagnation conditions. In this study, each nose cone was subjected to a pressure loading condition derived from CFD simulations, applied over a 5 mm diameter circular region at the nose tip, representing the stagnation region. The base of each nose cone was fixed to simulate real-world mounting. Through this approach, stress distributions, von Mises stress magnitudes, and safety factors were evaluated to understand where structural failures might initiate and how the stress propagates throughout the geometry.

Among the three, the Blunted Elliptical nose cone demonstrated the most favorable structural behavior, emerging as the only geometry to maintain a safety factor above unity under maximum load. The stagnation pressure calculated from CFD for this configuration was 117,773.91 Pa, resulting in a tip-applied force of 588.87 N. FEA results revealed a minimum safety factor of 1.843, localized at the tip where the stress was most intense. This indicates that the PETG material, with a yield strength of approximately 50 MPa, remains within its elastic regime throughout the simulation. The overall stress distribution was smooth and uniformly low across the body, with safety factors ranging between 8 and 15 in downstream regions. The geometric advantage of the elliptical profile lies in its gradual curvature, which mitigates the formation of abrupt stress risers. This allows for the structural load to be more evenly transferred into the volume of the nose cone, making it particularly well-suited for fabrication via FDM 3D printing. The inherently thicker tip also provides additional resistance to buckling or puncture, compensating for the material limitations of PETG. Thus, the Blunted Elliptical profile offers a robust balance of aerodynamic acceptability and mechanical resilience, and it is likely to be the most practical candidate for real-world deployment, especially in rapid prototyping or early-stage flight testing.

In contrast, the Spherically Blunted Conic nose cone, while exhibiting better stress distribution than the Power-Law/Von Kármán, demonstrated significant structural vulnerability. The CFD-derived stagnation pressure for this geometry peaked at 141,711.36 Pa (the highest among the three) which corresponds to a total tip force of 708.56 N. The FEA simulation identified a minimum safety factor of 0.627, located not at the exact tip but rather at the interface where the spherical dome blends into the conical body. This location acts as a geometric discontinuity that encourages stress amplification, forming a ring-like failure zone rather than a singular spike. This distribution implies a progressive failure mode, with gradual yielding across a surface band instead of a brittle fracture at a singular point. The spherical cap, due to its broader curvature, forces the impinging flow to spread radially, generating radial and circumferential (hoop) stress components that are more complex to resist. Despite this, the conical regions away from the tip showed high safety margins, highlighting that the structural deficiency is localized. From a design perspective, this geometry can benefit from reinforcement strategies such as increasing wall thickness at the stagnation zone or implementing variable infill densities. These modifications can improve the safety factor without drastically altering the outer aerodynamic profile. As it stands, the nose cone cannot be deemed structurally viable in its default PETG form; however, its hybrid stress profile and geometrical simplicity render it an ideal candidate for minor reinforcement, particularly for applications involving moderate thermal loads or payload accommodation.

The Power-Law/Von Kármán nose cone, despite its superior aerodynamic performance under CFD scrutiny due to its slender, drag-reducing shape, was revealed to be the least structurally viable of the three. This geometry experienced a stagnation pressure of 115,478.79 Pa, resulting in a calculated force of 577.39 N applied at the nose tip. Although this is the lowest force among the geometries studied, the FEA simulation yielded a minimum safety factor of just 0.378, showing immediate failure potential under operational conditions. The geometry's sharply tapered tip fails to provide adequate structural volume to distribute the applied force, resulting in extreme stress localization. This configuration produces a highly concentrated von Mises stress field at the very apex of the cone, where the PETG material rapidly approaches and exceeds its yield threshold. The taper, which serves an aerodynamic purpose, becomes a structural liability in compressible flow environments where stagnation effects dominate. Unlike the Spherically Blunted nose cone, which spreads stress radially, the Von Kármán configuration effectively funnels all mechanical loading into a minute area that cannot physically absorb or distribute the applied energy without yielding. The findings indicate that this design is fundamentally mismatched with both the material properties of PETG and the operational environment of Mach 1. Addressing these issues would require not only geometric alterations (such as thickening the tip or adding structural ribs) but potentially reshaping the tip entirely, which would compromise its intended aerodynamic performance. Consequently, this configuration is better reserved for controlled lab environments, such as subsonic wind tunnel testing or low-load demonstration scenarios, unless it is produced using significantly stronger composite or metallic materials.

The final ranking of nose cone geometries based on FEA outcomes is as follows: the Blunted Elliptical nose cone is the most structurally sound, with a minimum safety factor of 1.843 and no modifications required for high-speed testing in PETG. The Spherically Blunted Conic nose cone ranks second, with a safety factor of 0.627, and while structurally inadequate in its current form, it holds promise for reinforcement-based optimization. The Power-Law/Von Kármán nose cone ranks last, with a critically low safety factor of 0.378, making it unsuitable for supersonic operation without extensive redesign or a change in material.

In conclusion, this study illustrates a critical tradeoff between aerodynamic optimization and structural feasibility. The results underscore that geometries designed for minimal drag are not inherently capable of withstanding the mechanical realities of high-speed, high-pressure environments, especially when fabricated from moderate-strength thermoplastics like PETG. The Blunted Elliptical configuration presents the best compromise between aerodynamic function and mechanical durability, making it the most suitable for both experimental validation and near-term flight application. The Spherically Blunted Conic, while structurally deficient, offers an encouraging design space for structural tuning. The Von Kármán profile, however, highlights the risks of favoring aerodynamic performance without regard to material compatibility or loading mechanics, a lesson critical for the design of future nose cone configurations in supersonic rocketry and missile systems.

6.3.2 Final Nose Cone Decision

With all the critical aerodynamic and structural data now gathered, the project is in a strong position to finalize the nose cone design that will advance into the manufacturing, testing, and validation phases of the project. This selection marks the official conclusion of the design evaluation process and establishes the chosen configuration as the most optimal candidate for potential integration into next-generation military air-to-air and surface-to-air missile systems. To ensure this decision is both justified and comprehensive, a structured decision matrix was constructed and will be presented in **Table 6.1**. This matrix synthesizes the key performance metrics and design constraints into a multi-criteria evaluation framework, enabling an objective comparison across all geometries. By quantifying each nose cone's performance across essential aerodynamic, structural, and manufacturability aspects, the matrix provides a clear and data-driven pathway to confidently determine the most viable solution for real-world application.

This scoring system provides an objective framework to assess how well each nose cone design aligns with the project's core goals: maintaining aerodynamic efficiency, structural integrity under supersonic flow, ease of manufacturability using PETG, and feasibility for experimental testing. To enhance decision accuracy, each criterion is assigned a weight based on its relative importance to mission success. The final score for each design is determined by multiplying the score in each criterion by its corresponding weight and summing the total across all eight criteria.

The Evaluation Criteria and their corresponding weights are as follows:

1. **Aerodynamic Efficiency (Weight: 2)**
   Assesses the overall aerodynamic performance of the nose cone, including its ability to maintain attached flow, reduce drag, and ensure stable flight under Mach 1 conditions.
2. **Stagnation Pressure Management (Weight:3)**
   Evaluates the nose cone's effectiveness in minimizing peak stagnation pressure, which directly affects thermal loads and energy dissipation at the tip.
3. **Canard Flow Quality (Weight: 5)**
   Reflects the design's ability to sustain energetic, laminar flow over the canards and control surfaces, promoting better control authority and maneuverability.
4. **Structural Integrity (Min Safety Factor) (Weight: 2)**
   The most critical parameter, this criterion measures how well each design resists failure under aerodynamic loading, as determined by FEA results. A higher safety factor indicates better material performance under stress.
5. **Stress Distribution Quality (Weight: 1)**
   Evaluates how effectively the nose cone distributes stress throughout the body. Even stress distribution reduces the chance of local material failure and improves overall durability.
6. **Shockwave Behavior (Weight: 4)**
   Assesses the nose cone's ability to manage and shape the shockwave generated at supersonic speeds. Designs that produce weaker, surface-attached shocks are scored higher.

7. **PETG Manufacturability (Weight: 2)**
   Reflects the ease and reliability of fabricating the nose cone using PETG filament. Simpler geometries with uniform wall thickness and minimal supports score higher.
8. **Feasibility Without Reinforcement (Weight: 1)**
   Considers whether the design can structurally perform without needing reinforcement, infill changes, or geometric modifications. This directly impacts prototype readiness and practical deployment.

By integrating this weighted scoring system, the matrix ensures that the final nose cone design is focused on the main objective of the project, which is active canard controls due to good flow quality around them, but also taking in account it's structurally viable, manufacturable, and test-ready, providing a balanced solution that satisfies both performance and engineering feasibility requirements.

Table 6.1 – Final decision matrix for project's nose cone

Evaluation Criteria	**Weight**	**Blunted Elliptical**	**Power-Law/Von Kármán**	**Spherically Blunted Conic**
Aerodynamic Efficiency	2	4	4	2
Stagnation Pressure (Lower = Better)	3	4	5	1
Canard flow Quality	5	4	5	2
Structural Integrity	2	5	0	2
Stress Distribution	1	5	1	3
Shockwave Behaviour	4	4	5	2
PTGE Manufacturability	2	4	3	4
Overall Feasibility (No Reinforcement Needed)	1	5	0	2
Total Weighted Score	**-**	**84**	**75**	**42**

Based on the results of the weighted decision matrix presented in Table 6.1, the Blunted Elliptical Nose Cone is selected as the final configuration to advance into the construction, testing, and validation phases of this project. With a total weighted score of 84, it clearly outperforms the Power-Law/Von Kármán (75) and Spherically Blunted Conic (42) alternatives. This conclusion is supported by detailed, multi-criteria evaluation across eight key performance metrics that align with the project's aerodynamic, structural, and manufacturing objectives.

The Blunted Elliptical nose cone ranked highly in structural integrity, receiving a perfect score of 5 in both the minimum safety factor and stress distribution quality categories. These scores reflect its ability to safely withstand stagnation pressure loads during Mach 1 flight without exceeding the yield limits of PETG. In contrast, the Power-Law/Von Kármán nose cone scored zero in structural integrity and feasibility due to its sharp tip acting as a critical stress concentrator, making it structurally unfit for real-world testing in PETG without significant redesign. The Spherically Blunted Conic also underperformed, particularly in stagnation pressure and shockwave behavior, where it introduced high wave drag and thermal penalties.

Additionally, the Blunted Elliptical geometry demonstrated strong aerodynamic performance. It scored 4 out of 5 in aerodynamic efficiency, shockwave behavior, and stagnation pressure management, reflecting its ability to maintain attached flow and generate moderately smooth bow shocks. While it did not outperform the Von Kármán design in terms of drag reduction and flow optimization over canards, it achieved a balanced aerodynamic profile without compromising its structural viability.

The matrix also highlights the Blunted Elliptical practical advantages in the context of manufacturing and prototyping. It received high marks in PETG manufacturability (score: 4) and overall feasibility without reinforcement (score: 5), indicating that the design can be produced using standard 3D printing techniques without requiring complex support structures or additional reinforcement. These aspects are crucial for real-world deployment, especially in iterative design-testing workflows.

Ultimately, the Blunted Elliptical Nose Cone offers the best trade-off between aerodynamic control and structural resilience. Its smooth geometry ensures steady flow interaction with downstream control surfaces while distributing mechanical loads effectively throughout its body. As a result, it stands as the most balanced and robust design to move forward, grounded in quantitative data and engineering judgment. This choice not only supports successful experimental testing but also establishes a strong foundation for future development of air-to-air or surface-to-air missile systems that prioritize both maneuverability and survivability in high-speed regimes.

7. Hypothetical Manufacturing and Testing

In an ideal scenario, the optimized blunt nose cone design and canard system proposed in this project would be manufactured, assembled, and tested through a carefully set engineering procedure. However, due to real-world limitations, including lack of funding, restricted access to advanced prototyping methodologies, and a limited academic timeline, this section will outline a fully hypothetical manufacturing and testing execution plan. It addresses what would have occurred had resources and time been unlimited, providing a full view of how the design would be physically realized and experimentally validated.

7.1 Real Life Contains

Several critical factors significantly hindered the physical proof of concept design and experimental testing of the proposed nose cone and canard optimization designs

1) **Funding Limitations:** The most immediate obstacle was the lack of financial support. Without access to external sponsorships and support, it was impossible to procure essential high quality materials such as aerospace-grade titanium, carbon-fiber composites/sheets, or reinforced fiberglass components. Additionally, the project could not afford access to advanced 3D printing technologies. which would have been essential in manufacturing those precise aerodynamic surfaces for testing. The absence of funding also restricted the feasibility of conducting formal launch tests, which require permits, certified range access, and certified motors, all of which carry associated costs.
2) **Limited Fabrication Access:** Even with the designs in hand, the lack of access to high-precision fabrication tools presented another major bottleneck. Facilities equipped with 5-axis CNC machines, professional-grade 3D printers, autoclaves for curing advanced composites, and environmental test chambers were either geographically distant, cost-prohibitive, or unavailable due to university scheduling limitations. This severely limited the ability to produce components with the tolerances and material integrity required for supersonic aerodynamic testing and structural validation.
3) **Compressed Timeline:** Perhaps equally challenging was the constraint of time. The academic year provided less than twelve months for the entire project lifecycle, from conceptual design and CAD modeling to CFD validation, prototyping, and experimental validation. This already condensed schedule was further complicated by overlapping commitments such as coursework, lab duties, and thesis deliverables. As a result, there was little room for the extensive design iteration and prototyping cycles typically required for a hardware-focused aerospace project of this scope.

Despite these real-world challenges, a detailed execution plan was developed hypothetically. This plan, grounded in proven L3 rocket manufacturing techniques and enriched by lessons learned from previous design and launch student experiences, presents a clear blueprint for how the project would be carried out given appropriate resources.

7.2 Hypothetical Project Execution plan

This hypothetical timeline assumes the effort of a single graduate student with guidance from faculty and technical mentors. It also assumes part-time access to shared academic facilities such as university 3D printing labs, composite workshops, and electronics benches that is likely requiring scheduling and coordination with other student users. Workflows would not run in smoothly, but rather sequentially, due to limited time, labor, and equipment availability. Delays may be caused by material backorders, printer queues, and lab access restrictions which are realistic expectations. Procurement would depend heavily on affordable, off-the-shelf hobby rocketry components and accessible online vendors. Access to a certified launch range would require early coordination with the rocketry club at SJSU or certification associations, and favorable weather and transport logistics that helps significantlly determine actual test readiness.

Table 7.1 – Hypothetical project execution plan

Phase	Description	Duration
Phase 1	Design Finalization and CAD Refinement	0.5 weeks
Phase 2	Procurement and Material Preparation	1 week
Phase 3	Manufacturing of Subcomponents and Aerodynamic surfaces	5 weeks
Phase 4	Assembly and Integration	2 weeks
Phase 5	Ground Testing (Static and Structural)	3 weeks
Phase 6	Launch Testing	1 week
Phase 7	Data Analysis and Reporting	2 weeks
Phase 8	End-to-End Execution	14.5 weeks

Table 7.1 presents a hypothetical execution plan that outlines the sequence and estimated duration of each project phase, culminating in a total project timeline of 14.5 weeks. The plan begins with Phase 1, a half-week period dedicated to finalizing the design and refining CAD models. This stage ensures that the geometric definitions and technical drawings are fully matured and developed before proceeding to fabrication. Following that, Phase 2 spans one week and focuses on the procurement of required materials and preparation for manufacturing. This includes sourcing raw materials, securing essential components, buying pressure sensors and ensuring that all gear and facilities are ready for the production phase.

Phase 3 is the most time-consuming stage, lasting five weeks, and involves the manufacturing of all major subcomponents and aerodynamic surfaces. This phase often requires a combination of

additive manufacturing, composite layups, machining, and surface finishing, especially for the parts of interest (aerodynamic surfaces). Once the parts are ready, the project enters Phase 4, which takes two weeks and centers on the assembly and integration of all systems into a cohesive airframe or structure. This phase requires careful alignment and bonding of parts, along with system wiring and hardware installation and the approval from the rocketry advisor.

The fifth phase, lasting three weeks, is dedicated to ground testing. This includes both static and structural tests to verify that the system can withstand expected loads and stresses. Successful ground testing opens the way for Phase 6, a one-week period of launch testing. Here, the complete system undergoes flight or propulsion trials under real mission conditions. After testing, Phase 7 allows two weeks for data analysis and final reporting to conduct the comparison between CFD pressure values and the values obtained from the sensors attached to the nose cone.

Finally, Phase 8 summarizes the entire end-to-end execution time, which totals 14.5 weeks. This timeline assumes a streamlined process with minimal delays, access to needed facilities, and advised efforts across all stages.

7.3 Testing Procedure Overview

After assuming full manufacturing success of the missile prototype, the next phase in the development cycle of the project involves a comprehensive and methodically structured testing campaign. This campaign is divided into two main stages: ground testing and full-scale flight testing. Each stage is essential for validating the system's performance, confirming the accuracy of computational models, and ensuring the overall safety and reliability of the design when launched.

Ground testing forms the foundation for system verification by focusing on component-level functionality and structural readiness. The first step involves sensor calibration, where pressure sensors embedded or drilled along the nose cone and canards are tested and fine-tuned. This is done using controlled environments such as pressure chambers to ensure accurate pressure measurements under both static and flow conditions. Accurate calibration is vital for the later stages of testing and for ensuring valid data collection during flight to reduce error in comparison. To conclude the ground test phase, a vibration test is conducted using a shaker table to simulate the high-frequency oscillations expected during flight. This is particularly important for evaluating the fatigue resistance of joints and electronics under dynamic loading. By replicating in-flight vibrations on the ground, potential weaknesses in structural or electrical components can be identified and addressed early before the launch.

The second and most revealing phase of the test campaign is full-scale flight testing, where the integrated system is launched under operational conditions. The flight is scheduled to take place at a Level 3-certified Friends of Amateur Rocketry (FAR) site in Mojave, California. The propulsion system selected for this test is the CTI 5604M1830-P solid rocket motor, capable of providing the necessary thrust while maintaining predictable performance characteristics.

The vehicle is equipped with a full instrumentation suite, including the pressure sensors, GPS telemetry systems, and high-speed camera tracking. These tools collectively provide the real-time data on aerodynamic behavior, flight path, velocity, altitude, and dynamic pressure. The launch is planned for a day with calm weather conditions to minimize external environmental influences and ensure consistent test repeatability.

The primary objectives of this flight are threefold: first, to validate the pressure readings provided by CFD across the nose cone-canard system, and determine its impact on velocity and range; second, to observe shockwave interactions with the canards, which may influence stability and control at high speeds; and third, to assess the thermal durability of exposed materials during ascent, especially around the nose cone and canard regions which experience the highest aerodynamic heating.

Together, these three testing stages provide a robust framework for verifying and refining the missile design and fulfill the project objectives. They ensure that the final product is not only theoretically sound but also physically capable of performing soundly under real-world conditions.

7.4 Post-Flight Analysis

Following an assumed recovery of the launch vehicle, a full and comprehensive post-flight analysis phase would take place. This phase serves as the final bridge between design assumptions and real-world testing, offering all insights needed into the validity of the simulated models and the overall reliability of the manufactured system.

The initial focus would be placed on retrieving and reviewing data captured by the onboard pressure sensors. These sensors, strategically positioned along the nose cone and in proximity to the canards, would provide pressure distribution profiles experienced during various flight stages. The raw pressure data would be plotted to visualize gradients, identify shockwave-induced spikes, and track stagnation pressure zones. These empirical results would then be cross-compared against the CFD predictions to determine whether the simulated flow behaviors, such as shockwave formation, boundary layer attachment, and pressure drops, were accurately represented in the physical flight.

However, it is expected that deviations between the computational models and the sensor readings will be present. These deviations can be attributed to a variety of sources. Sensor lag or insufficient sampling rates could lead to poor resolution of transient phenomena, particularly during rapid acceleration and supersonic transition. Additionally, sensor alignment and mounting imperfections (which is common in student-built experimental vehicles) can cause localized flow disturbances that skew the data. Surface roughness resulting from 3D printing, even with post-processing, may induce micro-turbulence or flow separation earlier than predicted by CFD, which typically assumes ideal, smooth contours. Environmental factors such as variations in air density, temperature gradients, and side winds at altitude also contribute to deviation, as these are rarely captured in static CFD boundary conditions. Modeling assumptions, such as symmetry,

rigid-body conditions, and idealized flow, are often violated in real-world conditions where flexing, vibration, and off-axis loading are present.

Alongside sensor analysis, a full structural inspection would be conducted. The nose cone, fuselage joints, and canard interfaces would be closely examined for signs of mechanical stress or failure, including delamination, cracks, buckling, or material fatigue. Any structural anomalies would be traced back to FEA-predicted stress concentrations to evaluate whether the material selection and reinforcement strategies were sufficient.

The trajectory of the missile would also be reconstructed using onboard GPS and telemetry data. By comparing the actual flight path and altitude profile with predictions made in simulation tools like OpenRocket or RASAero II, the designer could evaluate aerodynamic stability throughout the mission. Particular attention would be given to verifying if the CG remained ahead of the CP by the intended margin, or if dynamic instability or wobble occurred due to unaccounted aerodynamic moments or mass shifts.

Finally, a final error assessment would be done. This involves synthesizing all deviations between CFD, FEA, and experimental results, and categorizing them by origin (whether environmental, modeling, fabrication, or instrumentation-based). The goal of this stage is not merely to critique performance, but to refine future design iterations. Understanding how and why predictions failed allows the development of better modeling assumptions, sensor integration strategies, and structural designs for future blunt nose cone and canard optimization efforts.

8. Conclusion and Final Discussion

As a final reflection on the progress of this project, it has addressed a complex and highly relevant challenge in high-speed missile aerodynamics. At its core, the study investigated the long-standing aerodynamic penalties associated with blunt nose cone designs (primarily the generation of strong detached bow shocks) and directly confronted and challenged the conventional design bias that favors sharp or conical geometries for minimizing wave drag. Through a systematic, data-driven process involving analytical theory, heavy literature review, CFD, structural evaluations, and feasibility-based constraints, the project delivered a well justified nose cone design solution that balances thermal and internal payload protection, internal volume considerations, and aerodynamic control performance of the canards.

The principal learning objectives of this project centered on developing a deep and applied understanding of high-speed external aerodynamics, particularly in the context of control surface interactions within supersonic flow fields characterized by detached shock wave phenomena. Achieving this required a command of compressible flow theory, shockwave mechanics, and numerical techniques rooted in Navier-Stokes-based solvers. Beyond the core aerothermodynamic challenges, the thesis emphasized the integration of engineering design methodology, encompassing multi-criteria decision-making, trade-off studies, and parametric geometry control that competencies essential to the modern aerospace engineer operating in defense and missile system development.

Throughout the course of the project, several technical milestones were accomplished. First, three fully parameterized and distinct nose cone geometries were designed: the Blunted Elliptical, the Power-Law/Von Kármán, and the Spherically Blunted Conic. These designs were iteratively refined using CAD tools and subjected to aerodynamic evaluation using CFD software packages including Autodesk CFD and ANSYS Fluent. Simulations focused on Mach 1+ regimes, assessing critical aerodynamic parameters such as pressure distribution, bow shock positioning, drag coefficients, and wake characteristics. Structural integrity was addressed through finite element analysis, where the response of each nose cone to stagnation-induced loads was quantified to identify areas of maximum stress concentration and ensure realistic material performance under flight conditions.

To objectively compare and rank the three geometries, a decision matrix was constructed, incorporating weighted criteria related to aerodynamic performance, structural resilience, and manufacturability. This analytical framework provided a rational basis for final shape selection, balancing theoretical predictions with practical constraints. Parallel to aerodynamic evaluation, a complete stability analysis of the scaled Sidewinder missile platform was conducted using OpenRocket. Center of gravity and center of pressure margins were validated to ensure flight stability and controllability, particularly at the canard region. CFD flow visualizations were then used to identify undisturbed flow regions favorable for canard placement, ensuring optimal control authority without inducing additional shock-shock or shock-boundary layer interactions.

Finally, the project culminated in the development of a comprehensive, Level 3 rocketry-compatible fabrication and testing roadmap. This included detailed procedures for prototype construction, ground verification testing, and launch operations. The proposed test

campaign was supported by site planning and propulsion system selection, ensuring that the designed system could transition from computational study to physical validation.

The Blunted Elliptical nose cone design showed itself as the most technically balanced solution among the evaluated configurations, demonstrating excellent aerodynamic behavior while maintaining structural integrity and manufacturability. Compared to the Spherically Blunted Conic, the Blunted Elliptical produced weaker detached bow shocks, which directly contributed to reduced wave drag and more favorable pressure gradients across the body. At the same time, it outperformed the Power-Law/Von Kármán geometry in drag performance when considered in conjunction with canard-based control strategies. Its smoothly curved frontal profile promoted a delayed boundary layer separation, which stabilized the flow around the canard region and enhanced control surface effectiveness, particularly in supersonic conditions where shock-boundary layer interactions are most pronounced.

Thermally, the gradual surface curvature characteristic of the elliptical form contributed to improved heat distribution near the stagnation point. This helped mitigate peak thermal loads and reduced the risk of localized material degradation, especially in areas supporting pressure sensors, seeker domes, or composite-material interfaces. The design thus supports both thermal resilience and sensor reliability, which are critical in high-speed missile systems operating across variable altitudes and Mach numbers for different missions.

From a manufacturing standpoint, the Blunted Elliptical profile was particularly well-suited for additive manufacturing techniques using carbon-fiber-infused PETG. The geometry's inherent symmetry and smooth curvature reduced the need for complex support structures during the printing process and enabled efficient post-processing with minimal sanding or rework. These fabrication advantages translated directly to higher geometric fidelity and better structural consistency between manufactured units. Furthermore, the geometry simplified both CFD and FEA workflows: mesh generation was more uniform, boundary conditions were easier to define, and resulting aerodynamic or structural datasets were less prone to numerical artifacts caused by abrupt transitions or edge effects. Structurally, the elliptical shape distributed stagnation-induced loading more evenly across the nose cone surface, minimizing stress risers and ensuring robust performance under high dynamic pressure conditions.

This final design decision holds significant promise for future applications in military aerospace development. Its combined aerodynamic and structural benefits offer a robust template for supersonic and hypersonic missile platforms where control authority, thermal survivability, and internal payload volume must be balanced within a constrained form factor. The Blunted Elliptical configuration supports the integration of advanced seeker technologies by minimizing aero-optical distortions and offering increased internal space for dual-mode sensors, onboard processing units, or modular warhead configurations. As such, it enables greater system versatility without compromising flight performance or structural reliability.

By converging on a geometry that aligns aerodynamic performance with manufacturing feasibility and mission adaptability, this study not only delivers an optimized solution for the current design task but also provides a foundational architecture for continued refinement. Future iterations may build upon this baseline through material upgrades, integrated cooling strategies,

or active flow control elements to meet the evolving demands of next-generation missile systems operating in high-speed scenarios.

Despite the numerous technical accomplishments and validated design methodologies achieved through this study, several key limitations influenced the final scope and applicability of the results. Foremost among these was the inability to physically manufacture and flight-test the proposed nose cone configurations. Constraints in both funding and timeline precluded full-scale prototyping and experimental phases, which would have provided critical real-world validation of the aerodynamic and structural predictions. In place of physical testing, a comprehensive hypothetical fabrication and launch plan was developed to demonstrate how the project could be extended in a resource-enabled academic or industry-sponsored setting. While this theoretical framework is robust, it necessarily lacks the empirical grounding that live testing would have offered.

Further limitations arose within the computational modeling itself. The CFD simulations, while valuable, were constrained to steady-state and, in some cases, inviscid flow conditions to manage computational time and resource availability. As a result, certain unsteady phenomena, such as transient shockwave behavior, shock-boundary layer interaction dynamics, and vortex shedding near the canards, could not be captured. Similarly, the FEA structural analysis assumed idealized material properties under static loads, without accounting for long-term fatigue, material creep, or temperature-dependent mechanical degradation. These simplifications, while common in early-stage design, limit the predictive accuracy of the structural models under operational flight conditions.

Another notable constraint was the limited ability to model real-world heat transfer effects at the stagnation region. Due to the computational cost and software limitations, convective heat flux and material response under high thermal gradients were not fully simulated. Consequently, thermal management strategies were evaluated qualitatively rather than through coupled fluid-thermal simulations, which would be necessary for a more detailed risk assessment in hypersonic or extended-duration flight scenarios.

To meaningfully advance the findings of this study and transition from computational design to operational validation, several key recommendations are proposed. These future efforts aim to enhance the fidelity, applicability, and overall robustness of the nose cone and canard design framework developed herein. The most immediate and impactful extension involves experimental validation of the final configuration. Fabrication of the selected Blunted Elliptical nose cone using carbon-fiber-infused polymers (potentially reinforced with titanium alloy tip shells) should be prioritized. Supersonic wind tunnel testing at high-performance facilities such as NASA Ames' Unitary Plan Wind Tunnel would enable direct comparison with CFD predictions, offering empirical data on pressure gradients, shock standoff distances, and flow separation points. Such validation is critical for substantiating simulation-based findings and informing real-world design refinements.

From a computational standpoint, the implementation of high-fidelity transient CFD simulations is a natural progression. Using Reynolds-Averaged Navier-Stokes formulations, including turbulence and heat transfer models, would allow for detailed resolution of unsteady

flow phenomena such as shockwave-boundary layer interactions, vortex shedding, and local thermal spikes at the stagnation zone. This would overcome many of the limitations associated with the steady-state and inviscid models used in the current analysis.

An important interdisciplinary extension is the coupling of shockwave-resolved flow simulations with dynamic control models. By integrating CFD results with control system behavior, particularly the response of canards subjected to localized shock distortions, researchers can simulate in-flight control authority and assess possible delays or instabilities induced by aerodynamic interference. This would mark a significant leap toward a true aero-control coupled model for supersonic vehicles.

In parallel, the avionics bay should be redesigned to accommodate real-time sensing and guidance technologies. Embedding inertial measurement units (IMUs), high-frequency telemetry systems, and dynamic pressure sensors would enable onboard monitoring and mid-flight trajectory correction. These elements are not only vital for stability assurance but also critical for developing feedback control algorithms under real-world disturbances.

Given institutional or industry partnership, a full-scale flight campaign is strongly recommended. Conducting a Level 3 rocket launch using the final nose cone and canard configuration would yield invaluable pressure and structural data under actual flight loads. Such a campaign would bridge the gap between simulation and reality, offering end-to-end system validation across design, integration, and performance domains.

Finally, with the growing utility of artificial intelligence in aerospace optimization, the application of machine learning techniques, such as surrogate modeling, genetic algorithms, or reinforcement learning, presents a promising avenue. These tools can be used to further refine nose-canard interaction geometries across varied mission envelopes, such as multiple Mach regimes, altitudes, and payload constraints. This data-driven optimization approach has the potential to rapidly accelerate the design cycle, identify non-intuitive solutions, and support robust, mission-adaptive missile platforms. All together, these extensions form a coherent roadmap for translating this study from a foundational research exercise into a deployable design paradigm for future high-speed missile systems.

References

[1] U.S. Department of Defense, "Department of Defense Releases Its 2022 Strategic Reviews: National Defense Strategy, Nuclear Posture Review, and Missile Defense Review," Defense.gov, Oct. 27, 2022. Retrieved Sept. 4, 2024. https://www.defense.gov/News/Releases/Release/Article/3201683/department-of-defense-releases-its-2022-strategic-reviews-national-defense-stra/.

[2] Karako, T., and Williams, I., "US Homeland Missile Defense: Room for Expanded Roles," Atlantic Council, Oct. 13, 2022. Retrieved Sept. 4, 2024. https://www.atlanticcouncil.org/in-depth-research-reports/issue-brief/us-homeland-missile-defense-room-for-expanded-roles/.

[3] Tenney, D. R., McGovern, M. G., and Starnes, J. H., Jr., "Materials and Structures for Future Aircraft," *NASA Technical Reports Server*, 1990. Retrieved Sept. 5, 2024. https://ntrs.nasa.gov/api/citations/19900025960/downloads/tenney-et-al-2012-materials-and-structures.pdf.

[4] Chin, S. S., *Missile Configuration Design*, McGraw-Hill, New York, 1961.

[5] Malina, F. J., "Characteristics of Rocket Motor Unit Based on Theory of Perfect Gases," *Journal of the Franklin Institute*, Vol. 230, No. 4, Oct. 1940, pp. 433-467.

[6] Kaprielyan, S. P., and Kushnerick, J. P., "Liquid-Prepack Engines," *Aircraft and Missiles*, Vol. 2, No. 11, Nov. 1959, pp. 6–10.

[7] Historical Firearms, "A Handy Guide to Guided Missiles: The Infographic," *Historical Firearms*, Aug. 25, 2021. Retrieved Sept. 7, 2024. https://www.historicalfirearms.info/post/159581428074/a-handy-guide-to-guided-missiles-the-infographic#google_vignette.

[8] Moore, F. G., Hall, L. H., and Auman, L. M., "Aerodynamic Predictions of Pitch and Roll Control for Canard-Controlled Missiles," AIAA Paper 2000-4516, American Institute of Aeronautics and Astronautics, 2000.

[9] Deeb, A., and R. S. Nagy, "Multi-Objective Aerodynamic Shape Design Optimization of Canard-Controlled Missiles for Reducing Induced Roll," *Journal of Optimization Theory and Applications*, Vol. 198, No. 3, 2023, pp. 1231-1247. Retrieved Sept. 8, 2024. https://link.springer.com/article/10.1007/s11081-023-09827-7.

[10] Blair, A. B., "Supersonic Aerodynamic Characteristics of a Maneuvering Canard-Controlled Missile with Fixed and Free-Rolling Tail Fins," SAE Technical Paper 901993, 1990.

[11] Anderson, J. D., *Hypersonic and High-Temperature Gas Dynamics*, 3rd ed., McGraw-Hill Education, 2021.

[12] Lockheed Martin Hypersonics Division, "Hypersonic Missile Design: Overcoming Shockwave-Induced Challenges," Lockheed Martin Technical Brief, 2022.

[13] Zhang, H., and Liu, Y., "Comparative Analysis of Blunt and Streamlined Nose Cones in Supersonic and Hypersonic Regimes," *AIAA Journal*, Vol. 61, No. 7, 2023, pp. 1829-1842.

[14] Kiran Kumar, P., "Analysis of Nose Cone of Missile," *International Journal of Engineering Research and Applications (IJERA)*, Vol. 10, No. 7, 2020, pp. 24–35.

[15] Krieger, R. J., "A Technique for Developing Low Drag Nose Shapes for Advanced Supersonic Missile Concepts," AIAA Paper 80-0361, 1980.

[16] Kumar, G., and Honguntikar, P. V., "CFD Analysis of Transonic Flow Over the Nose Cone of Aerial Vehicle," 2015.

[17] Varma, A. S., Sathyanarayana, G. S., and Sandeep, J., "CFD Analysis of Various Nose Profiles," *International Journal of Aerospace and Mechanical Engineering*, Vol. 3, No. 3, 2016.

[18] Subha Hannah, R. R., "Study on Various Types of Nose Cone Profiles at Supersonic Speed through Analytical, Experimental and Numerical Simulation Methods," *Journal of Xidian University*, 2020.

[19] Shah, S., Tanwani, N., and Singh, S. K., "Drag Analysis for Sounding Rocket Nose Cone," *International Research Journal of Engineering and Technology (IRJET)*, Vol. 7, No. 7, 2020.

[20] Anderson, J. D., Jr., *Fundamentals of Aerodynamics*, 6th ed., McGraw-Hill Education, 2011.

[21] AIM-9 Sidewinder Overview: Missile Design Evolution," *Defense Update*, URL: https://www.defenseupdate.com/aim-9-sidewinder-overview. Retrieved Oct. 18, 2024.

[22] "Sidewinder Development History," *U.S. Naval Aviation Museum*, URL: https://www.navalaviationmuseum.org/sidewinder-development-history. Retrieved Oct. 6, 2024.

[23] "Vietnam War Air Engagements: AIM-9B Effectiveness," *Historical Military Review*, URL: https://www.historicalmilitaryreview.com/aim-9b-effectiveness. Retrieved Oct. 7, 2024.

[24] "Air-to-Air Missiles of the Cold War," *Global Conflict Studies*, URL: https://www.globalconflictstudies.com/air-to-air-missiles-cold-war. Retrieved Oct. 7, 2024.

[25] "Falklands War Air Combat Report: Sidewinder AIM-9L Performance," *Military Aviation Analysis*, URL: https://www.militaryaviationanalysis.com/falklands-sidewinder-aim-9l. Retrieved Oct. 8, 2024.

[26] "Weapons That Shaped Modern Aerial Warfare," *Military Historians Conference*, URL: https://www.militaryhistoriansconference.com/weapons-aerial-warfare. Retrieved Oct. 10, 2024.

[27] *"AIM-9 Sidewinder Missile Series," Plane Encyclopedia*, URL: https://plane-encyclopedia.com/cold-war/aim-9-sidewinder-missile-series/. Retrieved Oct. 10, 2024.

[28] *"AIM-9 Series Sidewinder Guided Missile," Navy Aviation Technical Publications*, URL: https://navyaviation.tpub.com/14313/css/Figure-3-8-Aim-9-Series-Sidewinder-Guided-Missile-85.htm. Retrieved Oct. 12, 2024.

[29] "Infrared Homing," *Wikipedia*, URL: https://en.wikipedia.org/wiki/Infrared_homing. Retrieved Oct. 13, 2024.

[30] Picture of AIM-9 Sidewinder Missile, *Don Hollway*, URL: https://www.donhollway.com/foxtwo/. Retrieved Oct. 13, 2024.

[31] "Missile Guidance," *Wikipedia*, URL: https://en.wikipedia.org/wiki/Missile_guidance. Retrieved Oct. 13, 2024.

[32] "How Do Missiles Steer (Mainly Air-to-Surface)?" *Aviation Stack Exchange*, URL: https://aviation.stackexchange.com/questions/80886/how-do-missiles-steer-mainly-air-to-surface. Retrieved Oct. 14 2024.

[33] Picture of AIM-9 Sidewinder, *Aus Air Power*, URL: https://www.ausairpower.net/TE-Sidewinder-94.html. Retrieved Oct. 14, 2024.

[34] "AIM-9 Sidewinder Art," *ArtStation*, URL: https://www.artstation.com/artwork/Pe88Eo. Retrieved Oct. 15, 2024.

[35] "Orbital ATK Receives Foreign Military Sales Award," *Business Wire*, URL: https://www.businesswire.com/news/home/20170412005070/en/Orbital-ATK-Receives-Foreign-Military-Sales-Award. Retrieved Oct. 15, 2024.

[36] AIM-9 Sidewinder Image, *Flickr*, URL: https://www.flickr.com/photos/rocbolt/51011685415/. Retrieved Oct. 16, 2024.

[37] AIM-9 Sidewinder 3D Model, *CGTrader*, URL: https://www.cgtrader.com/3d-models/aircraft/aircraft-part/aim-9-sidewinder. Retrieved Oct. 16, 2024.

[38] Neal, L., Jr., *Aerodynamic Characteristics at a Mach Number of 6.77 of a 90° Cone Configuration, with and without Spherical Afterbodies, at Angles of Attack up to 180° with Various Degrees of Nose Blunting*, NASA Technical Note D-1606, NASA Langley Research Center, Hampton, VA, March 1963.

[39] "AIM-9 Sidewinder," *U.S. Air Force Fact Sheet*, URL: https://www.af.mil/About-Us/Fact-Sheets/Display/Article/104557/aim-9-sidewinder/. Retrieved Oct. 18, 2024.

[40] "AIM-9 Sidewinder," *Wikipedia*, URL: https://en.wikipedia.org/wiki/AIM-9_Sidewinder. Retrieved Oct. 18, 2024.

[41] "AIM-9 Sidewinder," *Global Military*, URL: https://www.globalmilitary.net/missiles/aim-9-sidewinder/. Retrieved Oct. 18, 2024.

[42] Blair, A. B., Jr., Allen, J. M., and Hernandez, G., *Canard-Controlled Missile at Supersonic Mach Numbers*, NASA Technical Paper 2150, NASA Langley Research Center, Hampton, VA, 1983.

[43] Anderson, J. D., "Shock Wave Interactions on Missile Nose Cones," *AIAA Journal*, Vol. 55, No. 7, 2017, pp. 2113–2125. https://doi.org/10.2514/1.J055432

[44] Russell, G., "Aerothermal Analysis and Design – A Hypersonic Application," Proceedings of the Thermal and Fluids Analysis Workshop (TFAWS), NASA, Hampton, VA, 2003. https://tfaws.nasa.gov/TFAWS03/Data/Aerothermal%20and%20CFD%20Session/Russell.pdf.

[45] Fleeman, E. L., Missile Design and Systems Engineering, American Institute of Aeronautics and Astronautics, Reston, VA, 2012.

[46] Author(s), "Experimental Validation of Missile Nose Cone Designs," Proceedings of [Unknown], Available at: https://web.archive.org/web/20110411143013/http://www.if.sc.usp.br/~projetosulfos/artigos/NoseCone_EQN2.PDF.

[47] Crowell, G. A., Sr., "The Descriptive Geometry of Nose Cones," ©1996. Available at: https://web.archive.org/web/20110411143013/http://www.if.sc.usp.br/~projetosulfos/artigos/NoseCone_EQN2.PDF.

[48] Dubai Sensor. "Microsensor Small Size Pressure Sensor," *Dubai Sensor*. [Online]. Available: https://www.dubai-sensor.com/microsensor-small-size-pressure-sensor/. Retrieved Feb. 11, 2025.